# Designing Wave Attenuation Solutions using Hydro-Structural Modelling in ComFLOW to reduce Free Surface Motions within a Flooded Well-Dock of an existing Landing Platform Dock

D.M. Mehlbaum

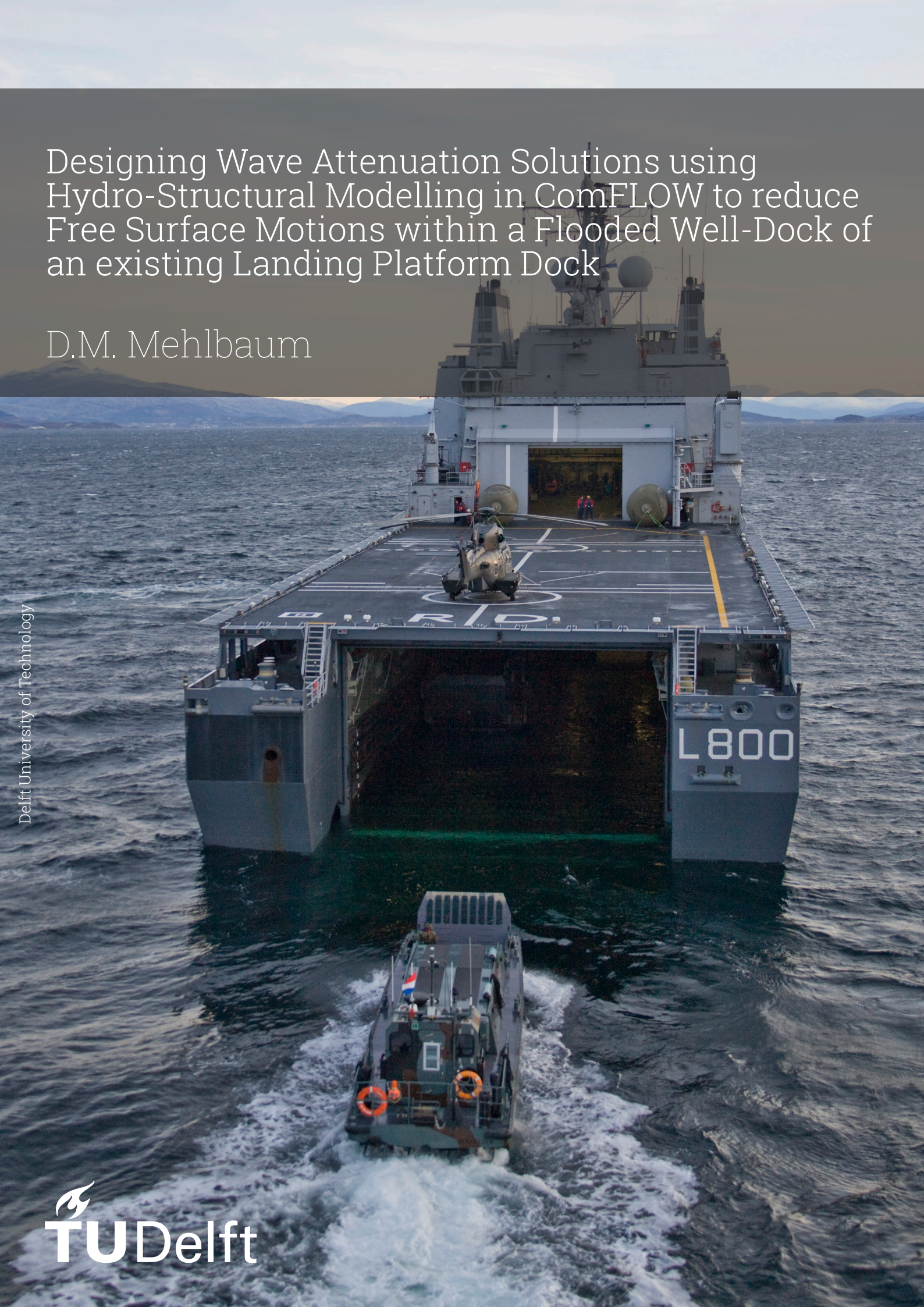


Delft University of Technology

TU Delft

# Designing Wave Attenuation Solutions using Hydro-Structural Modelling in ComFLOW to reduce Free Surface Motions within a Flooded Well-Dock of an existing Landing Platform Dock

by


D.M. Mehlbaum

| Student Name | Student Number |
|---|---|
| D.M. Mehlbaum (Dean) | 5315654 |


**Thesis comittee:**

| | |
|---|---|
| Chair & Supervisor TU Delft: | Dr. ir. P. R. Wellens |
| Second Supervisor TU Delft: | Dr. ir. G. H. Keetels |
| Third Supervisor TU Delft: | ir. A. D. Boon |
| Supervisor Ministery of Defence : | Dr. ir. R. W. Bos |
| Project Duration: | September, 2023 - July, 2024 |
| Institution: | Delft University of Technology |
| Faculty: | Mechanical Engineering (ME) |


**Report number:** MT.23/24.043.M


Cover: A Landing Craft Vehicle Personnel (LCVP) is entering a Landing Platform Dock (LPD) flooded well-dock (Source: Defensie.nl)

TU Delft

# Preface

This thesis is the final part of my Master's program in Offshore & Dredging Engineering at Delft University of Technology. Over the past ten months, working on this project has reminded me how dynamic and promising the field of hydrodynamics is, with the potential to solve many of tomorrow's big challenges.

Balancing this master's degree with a full-time job over the past 3.5 years has been tough but incredibly rewarding. I could not have done it without the support of my family and girlfriend. Looking back, I'm so glad I made the decision to start this challenging master's program.

This research was carried out in close collaboration with Delft University of Technology and Commando Materieel & IT (COMMIT). Both provided all the resources I needed for this thesis. For this reason, I especially want to thank Reinier Bos and Peter Wellens. They are not only experts in hydrodynamics but also fantastic mentors. Their knowledge and guidance have been invaluable and truly appreciated.

I hope you enjoy your reading.

*D.M. Mehlbaum*
*Delft, July 2024*

# Summary

A Landing Platform Dock (LPD) facilitates amphibious operations by allowing landing vessels such as the Landing Craft Vehicle Personnel (LCVP) and Landing Craft Utility (LCU) to embark and disembark from its internal flooded well-dock. The smooth transition of these landing vessels is critical, but can be hindered by wave motions (i.e. sloshing) within the well-dock, making safe embarking and disembarking more difficult.

Existing literature mainly describes wave motions within a well-dock, but does not address how to minimise these motions. This thesis aims to develop a preliminary design to reduce wave energy entering the dock by implementing an optimised wave attenuation solution.

ComFLOW is used to observe that wave motions inside the well-dock are highly non-linear and correspond to the LPD's oscillation period. The wave motions within the dock are caused by a drop in water level near the well-dock entrance. This causes waves to roll into the dock. In shallow water conditions like in the well-dock, the propagating waves hereby show amplitude dispersion and wave breaking.

Using a system engineering approach, a bottom-hinged pitching flap was found to be ideal for wave attenuation in shallow water conditions. The flap's attenuation performance was examined using ComFLOW by adjusting design parameters such as: mass, center of gravity, length and mechanical damping.

It was found that high-period waves with high wave heights fully couple dynamically with the flap, resulting in several outcomes. First, the flap follows the wave frequency, resulting in sub-optimal energy dissipation with use of radiation damping. Second, tuning the flap's natural period to match the incoming wave period, increases pitching angles but reduces angular velocity, leading to decreased wave attenuation. Third, lowering the centre of gravity increases the restoring moment and angular velocity. This results in enhanced energy dissipation of higher-order wave components. Fourth, increasing the flap's length improves wave attenuation due to enhanced reflection and radiation damping. Fifth, adding mechanical damping decreases attenuation performance, likely because the reduction in angular velocity worsens the energy dissipation effect for higher-order wave components. This research revealed that the best performing solution, with low a centre of gravity, attenuates 28.7% of wave energy entering the well-dock. Furthermore, optimising the flaps natural period to the incoming wave period was less effective, attenuating only 19.7% of the wave energy.

# Contents

# List of Figures

# List of Tables

# 1

# Introduction

In the heart of a ferocious North Sea storm, a team of determined Dutch marines embarked on a high-stakes mission. Buffeted by towering waves and relentless rain, they set out in small landing vessels toward a distant coastline. Hours of struggle later, they secured vital intelligence and turned back towards their sanctuary. The sight of the Landing Platform Dock (LPD) on the stormy horizon filled them with relief. Battling the waves, they finally reached the well-dock at the stern of the LPD vessel safely.

During missions and operations, LPDs can function as mother ships with internal harbors (well-dock). For this reason, the conditions during the embarking and disembarking of marines from the well-dock must be safe. Collisions and hard-to-control landings crafts due to extreme wave conditions within the well-dock must be avoided at all times. Figure 1.1 shows an LPD with an open well-dock and an approaching landing vessel at the stern.


**Figure 1.1:** LPD with open well-dock and a landing vessel approaching at the stern [11]

The Royal Netherlands Navy (RNN) has two LPDs, HNLMS Rotterdam and HNLMS Johan de Witt. Their main task is to support amphibious operations on the border of land and water (Figure 1.1) as described in the first paragraph. These vessels function as floating harbours, where Landing Craft Vehicle Personnel (LCVP) and Landing Craft Utility (LCU) can bring personnel and heavy equipment ashore. Additionally, these ships can serve as a mobile command centre for directing large-scale amphibious and maritime operations. To bring personnel and goods ashore without a harbour, the rear of the ship can lower up to four meters [22]. This allows water to flow into the internal well-dock, and the carried landing craft by the LPD can (dis-)embark. The Rotterdam can carry two LCU and three LCVP landing craft in its internal well-dock. The Johan de Witt can carry two LCUs and four LCVPs. As an example, the storage of these landing crafts inside a well-dock can be seen in Figure 1.2.

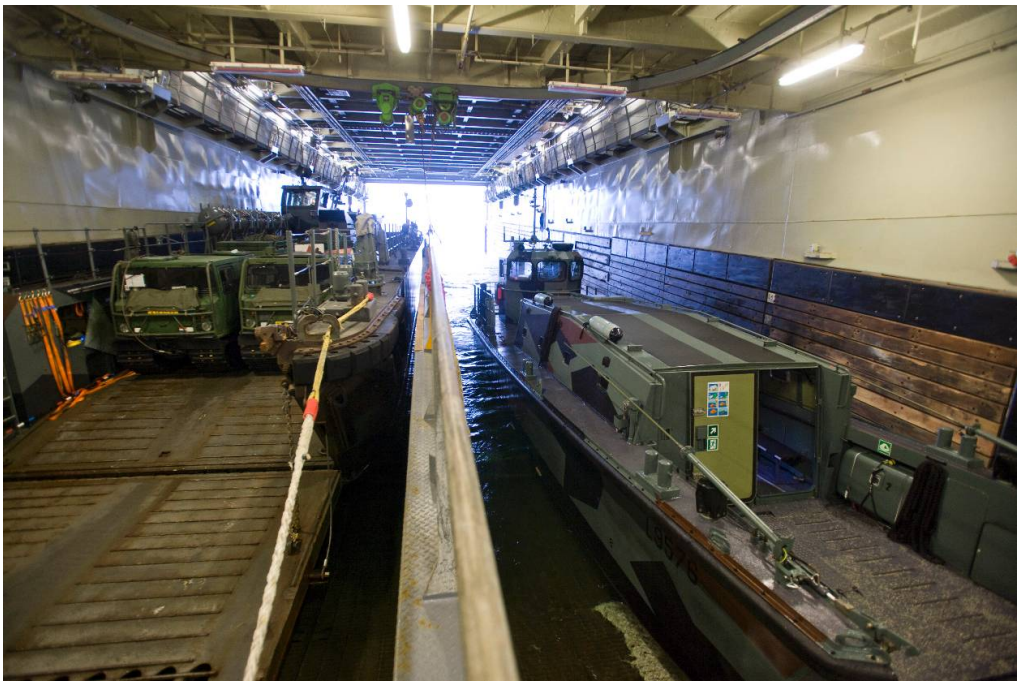

**Figure 1.2:** Landing craft vessels stored inside a well-dock of an LPD, left: LCU and right: LCVP [10]

The operability of LPDs depends on the landing craft's capability to transition smoothly from the well-dock to the open sea and vice versa [18]. To determine the operating parameters for safe sea transfers, it is important to understand the behaviour of the wave motions and the motions of the landing craft inside a well-dock. These internal wave motions are influenced by the motions of the LPD and incoming waves at the stern [54]. In some conditions, these motions can cause sloshing [52], as illustrated in Figure 1.3. Extreme sloshing events can decrease the operational window of the LPD due to two reasons: First, the landing craft vessels inside the dock will get slammed by surface waves, which makes them difficult to control. Secondly, extreme wave motions trigger wave-induced motions of the landing craft, which causes impacts with well-dock inner walls or bottom [7][59].

As a result, the RNN only performs amphibious operations in sea states with specific characteristics. Ultimately, the RNN wants to have a maximum operation time in a wide range of sea states. This can be accomplished by reducing extreme wave motions within the dock, so lowering the risk of a collisions.

**Figure 1.3:** Free surface oscillations within a well-dock of an LPD [41]

## 1.1. Problem Statement

The problem statement will be described in the following section, starting with the high-level demand in LPD operations and progressing to the low-level hydrodynamic effects within the well-dock.

### 1.1.1. Geopolitical

The world still faces a great deal of hazards, especially in light of the ongoing conflict in Ukraine. The Dutch Ministry of Defence therefore needs increased adaptability [48]. When looking at the transition to the planned amphibious vessels, these must be in accordance with the emerging risks and developments in operations. A recent example of such adaptability can be seen in the so-called Amphibious Task Group 2024 of NATO.

### 1.1.2. Operational

The rising need for amphibious operations places a significant strain on current LPDs, especially in areas with higher sea states such as the Baltic Sea, the North Sea and the North Atlantic. Eventually, increasing sea states result in a higher probability of significant wave heights and wave periods. The main goal is to extend LPD operations with longer time brackets and higher sea states, which correspond to harsher sea conditions. The impact of these conditions on the operability of the LPD will be further explained in the following sub-paragraph.

### 1.1.3. Physical

This subparagraph will discuss the physical issues that can arise in an LPD's well-dock when operating in rough seas. In these higher sea states, wave characteristics tend to align more closely with the natural frequency of the LPD [22]. Within this thesis, it is assumed that the longitudinal sloshing inside a well-dock is triggered by the natural frequency of heave and pitch motions. This hypothesis will be further supported with evidence from existing literature presented in Section 2.2.

Regarding these pitch and heave motions, Wang G. et al. [52] indicated that the LPD exhibits a natural period of approximately 11.4 s. Hopman et al. [22] stated that a major requirement is that the embarking and disembarking operations must be possible for sea conditions up to sea state 4. Analysing a sample wave spectrum from the North Atlantic (Figure 1.4), it becomes evident that there is a considerable likelihood (25%) of encountering 1.5 m to 2.5 m waves with this wave period (highlighted in blue) when operating in these sea states.

**North Atlantic, Anual**

| Significant wave height [m] | | | | | | | | | | | | | | | | |
|---|---|---|---|---|---|---|---|---|---|---|---|---|---|---|---|---|
| 18.5 | | | | | | | | | | | | | | | | |
| 17.5 | | | | | | | | | | | | | | | | |
| 16.5 | | | | | | | | | | | | | | | | |
| 15.5 | | | | | | | | | | | | 0.01 | 0.01 | | | |
| 14.5 | | | | | | | | | | | | 0.01 | 0.01 | | | |
| 13.5 | | | | | | | | | | | 0.01 | 0.04 | 0.01 | | | SS8+ |
| 12.5 | | | | | | | | | | | 0.01 | 0.04 | 0.01 | | | SS8+ |
| 11.5 | | | | | | | | | | 0.01 | 0.05 | 0.07 | 0.01 | | | SS8 |
| 10.5 | | | | | | | | | | 0.03 | 0.15 | 0.08 | 0.02 | | | SS8 |
| 9.5 | | | | | | | | | 0.02 | 0.14 | 0.24 | 0.12 | 0.02 | | | SS8 |
| 8.5 | | | | | | | | 0.01 | 0.17 | 0.46 | 0.24 | 0.15 | 0.02 | | | SS7 |
| 7.5 | | | | | | | | 0.17 | 0.55 | 0.59 | 0.27 | 0.18 | 0.02 | | | SS7 |
| 6.5 | | | | | | | 0.02 | 1.02 | 0.84 | 0.71 | 0.33 | 0.22 | 0.03 | | | SS7 |
| 5.5 | | | | | | 0.02 | 0.48 | 2.30 | 0.96 | 0.76 | 0.36 | 0.24 | 0.04 | | | SS6 |
| 4.5 | | | | | 0.01 | 0.62 | 2.38 | 2.58 | 0.99 | 0.77 | 0.42 | 0.24 | 0.06 | | | SS6 |
| 3.5 | | | | | 0.63 | 3.50 | 2.96 | 2.59 | 1.11 | 0.84 | 0.48 | 0.27 | 0.07 | | | SS5 |
| 2.5 | | | 0.02 | 1.64 | 4.20 | 4.35 | 2.92 | 2.27 | 1.22 | 0.97 | 0.60 | 0.32 | 0.09 | | | SS4 |
| 1.5 | | 0.22 | 3.00 | 5.06 | 4.18 | 4.09 | 2.77 | 2.92 | 1.23 | 1.30 | 0.72 | 0.43 | 0.13 | | | SS4 |
| 0.5 | 0.41 | 0.26 | 4.19 | 4.29 | 2.97 | 3.71 | 2.04 | 1.99 | 0.90 | 1.01 | 0.45 | 0.16 | 0.04 | | | SS2 |
| T0 | 3.2 | 4.8 | 6.3 | 7.5 | 8.8 | 9.7 | 10.9 | 12.4 | 13.8 | 15.0 | 16.4 | 18.0 | 20.0 | 22.5 | 25.7 | |
| T1 | 2.5 | 3.7 | 4.9 | 5.8 | 6.8 | 7.5 | 8.4 | 9.5 | 10.6 | 11.6 | 12.6 | 13.9 | 15.4 | 17.3 | 19.8 | |
| T2 | 2.3 | 3.4 | 4.5 | 5.3 | 6.2 | 6.9 | 7.7 | 8.8 | 9.8 | 10.7 | 11.6 | 12.8 | 14.2 | 16.0 | 18.2 | |

**Figure 1.4:** Wave spectrum North Atlantic [1]

In this last part, the actual concrete physical problem that needs to be solved is presented in steps. Before doing so, the operational procedure to start a amphibious operation will be explained first:

1. The LPD sails to the designated area and positions itself stationary in head waves. Like depicted in Figure 1.5.

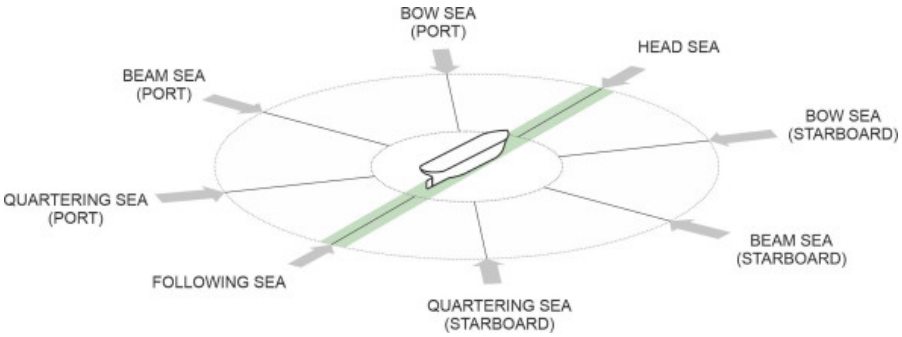


**Figure 1.5:** Wave-/sea directions [37]

2. The LPD opens the 11.0 m well-dock door and begins to fill the ballast tanks at the rear of the vessel.


**Figure 1.6:** LPD opening the well-dock door and filling its ballast tanks [44]

3. Due to the increased weight at the stern from ballast water, the LPD becomes submerged at this location, eventually causing the well-dock to flood. This process continues until a specific water depth within the dock is attained, as illustrated in Figure 1.7.

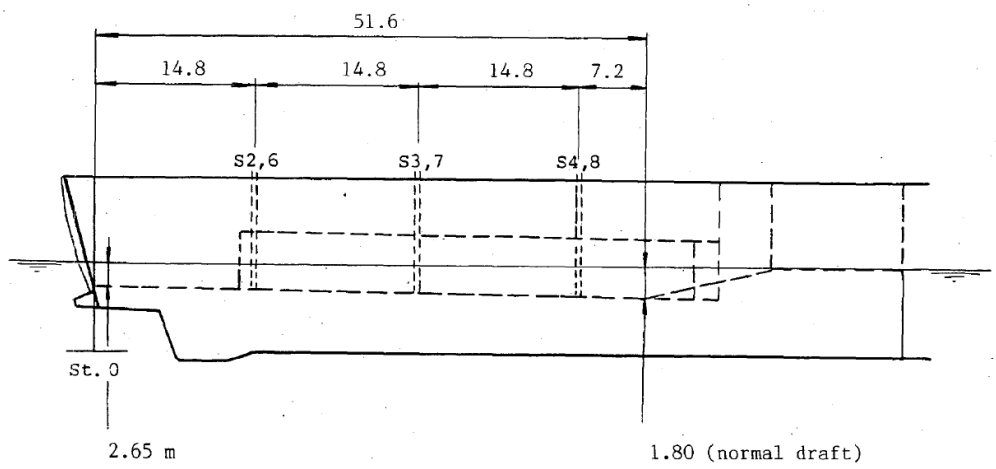


**Figure 1.7:** Flooded condition of an LPD well-dock

4. The LPD is now prepared for amphibious operations, facilitating the embarkation and disembarkation of landing vessels. An impression of such a condition can be viewed in Figure 1.8.

**Figure 1.8:** Landing vessel entering a well-dock [35]

When combining all facts, a brief summary of the problem statement can be described in the following events:

1. An increasing demand in LPD-operations in higher sea-states results in a higher probability of significant wave heights and wave periods.
2. Increased wave periods are in the range of the natural period of the LPD in heave and pitch motion.
3. Maximal motion amplitude of the LPD (well-dock included) in combined pitch and heave direction are reached.
4. Oscillating motions of the free surface are generated with these specific wave properties.
5. Landing vessels inside the well-dock come into motion due to the free surface motions.

6. Under specific wave conditions, the waves generated within the well-dock can escalate to a point where the motions of the landing vessels result in collisions between the bottom of the landing vessel and the floor of the well-dock.

In the end, event 6 results in an increase of aborting amphibious operations. So the percentage of time operational will decrease when no solution is provided. To make the LPD fulfill the required operability in a broader range of sea states, the wave energy entering the well-dock must be minimised. For this reason, research question(s) are stated which will require in-depth analysis to answer.

## 1.2. Research Question

As mentioned in Section 1.1, the overall operability of LPDs in higher sea states is influenced by the wave motions within the well-dock. These phenomena are unique within maritime engineering and not well examined [52] or reduced. This will be investigated by addressing the primary research question below:

***"How can wave attenuation solutions be designed with the use of hydro-structural computational modelling, ultimately reducing free surface motions within a flooded well-dock of an existing Landing Platform Dock?"***

To answer this main question, the following four sub-questions must be answered:

1. What is the modelling approach for simulating free surface motions in a flooded well-dock of an LPD under in a specific sea state?
2. What are the properties of free surface motions in a flooded well-dock of an LPD in a specific sea state?
3. What wave attenuation solution design(s) effectively decrease(s) free surface motions within the well-dock?
4. How can the wave attenuation solution be optimised by looking at design- and environmental input parameters?

### 1.2.1. Objectives

The main objective of this research is to design optimised wave-attenuation solutions to reduce unwanted wave motions within the well-dock of an LPD. To obtain these solutions, a model of the free surface motions must be computed first. This will be done with the use of Computational Fluid Dynamics (CFD). Using a numerical model, the entire well-dock or a specific section of it can be simulated. This allows for adjustments, such as implementing wave attenuation solutions or modifying input wave properties.

Answering the main question will lead to two impacts. First , the improvement of existing well-dock designs for LPDs in the RNN. This results to enhanced operability in amphibious operations in higher sea states over longer periods of time. Second, the outcomes provide valuable insights into how free surface elevations interact with wave attenuation solutions. This understanding can be utilized during the initial design phase of potential new LPD vessels or mid-life updates of existing vessels with well-docks.

In the end, this thesis has the following sub-objectives:

1. To determine a modeling approach that simulates free surface motions in a flooded well-dock of an LPD in a specific sea state.
2. To determine the wave motion characteristics within a flooded well-dock of an LPD in a specific sea state.
3. To determine the most effective wave attenuation concept solutions.
4. To optimise a concept solution by looking at design- and environmental input parameters.

## 1.3. Report Structure

This report is structured as follows:

- In the literature review, the basics and underlying theory is presented concerning: waves in general, the attenuation of wave energy and free surface elevations within a well-dock of an LPD.
- In Part I, the modeling choices identified in the literature review are used to set up a computational domain in CFD. Using known LPD Response Amplitude Operators (RAO's), the free surface elevations is created and examined.
- In Part II, a system engineering approach is applied to design different concepts. Several interviews and desk studies are conducted to determine the requirements and restrictions of these concepts.
- Part III contains all results related to the wave attenuation performance of the developed concept design. These results are obtained using both the linear boundary element method and non-linear CFD-software (i.e. ComFLOW).

A summary of the report structure with different parts is presented in Figure 1.9:

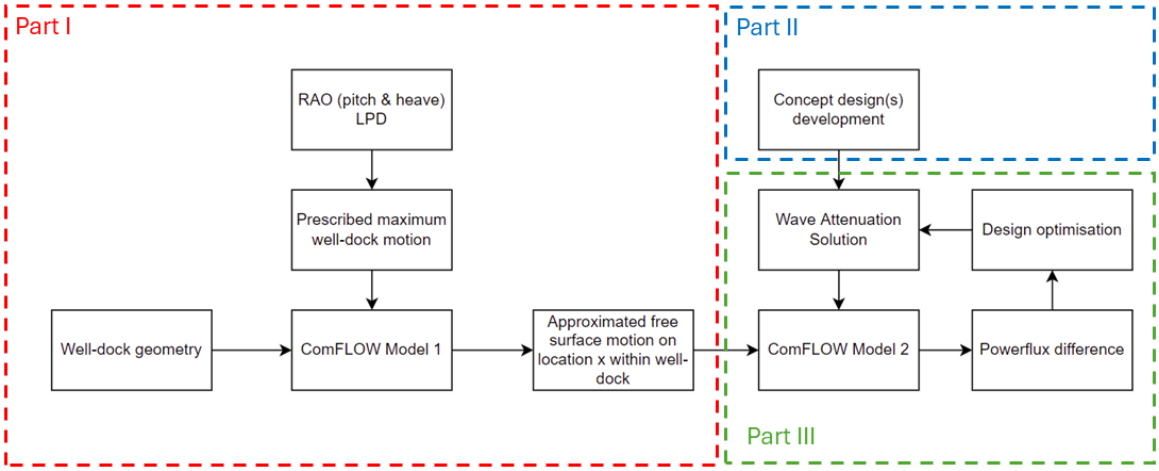


**Figure 1.9:** Overview report structure

# 2

# Literature Review

This chapter focuses on the existing literature on wave attenuation, discussing topics such as linear and non-linear waves, regular and irregular waves, and wave energy transport. In a separate literature review existing papers on free surface elevations within an LPD are examined.

## 2.1. Wave Attenuation

In this section various methods of wave attenuation will be explored. This phenomenon, known as the decrease in wave's energy over distance, arises from three primary causes. The first cause is transmission loss at interfaces, which occurs due to reflection, diffraction, mode conversion, and scattering [4]. The second cause is geometric divergence, where the energy of waves disperses as they move away from the source. The third cause is absorption or energy dissipation, where the energy of the wave is gradually lost.

Within this research, only two specific mechanisms are examined and utilised in designing and optimising a passive wave attenuation solution: wave reflection and wave energy dissipation (e.g. damping and/or wave breaking). These two topics will be further explained, with a detailed explanation of the main mechanisms. But first, the mechanisms and theories behind free surface waves and wave energy (transport) are examined.

### 2.1.1. Free surface waves

Simulating free surface motions within a well-dock is one aspect of achieving the thesis's main objective. For this reason it is essential to provide background information on wave theories that describes these surface waves (regular, irregular, linear & non-linear). When looking at a free surface wave, the oscillatory motion of wave propagation (as depicted in Figure 2.2) persists due to the interplay between gravity and inertia [49]. As waves transition from deep to shallow water, the orbital wave motion transforms from elliptical to more complex patterns, influenced by non-linearity's.

#### Linear waves

Linear wave theory represents the simplest and most widely used approach for describing the propagation of (gravity-) waves on the surface of a fluid. Nevertheless, no single reduced order theory adequately captures the behavior of waves across all heights, periods, and water depths, spanning from deep to intermediate and shallow waters. Only by solving the Navier-Stokes equations with use of CFD-software (e.g. ComFLOW) all hydrodynamics can be captured. Further on, the parameters like wave height, period and water depth are utilized to assess the applicability of wave theories. To conclude, the appropriate wave theory can be determined by considering environmental and wave properties, as depicted in Figure 2.1. It is critical to understand which wave regime is applicable. In this way the right equations and theories can be applied.

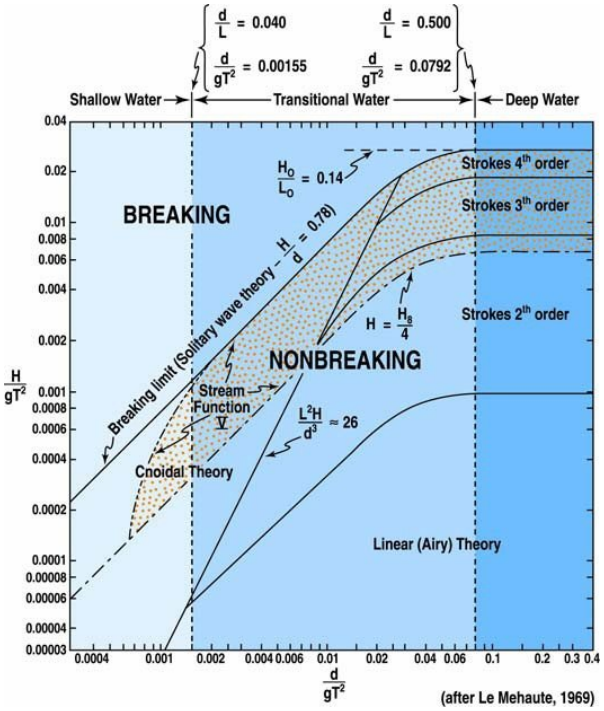


**Figure 2.1:** Graph indicating the validity of wave theories [28]

Upon applying the discussed theory to the problem statement outlined in Section 1.1 and referencing to Figure 1.3, it becomes evident that wave breaking takes place within the shallow or intermediate water depth of a well-dock. As waves roll into the dock, they propagate longitudinally, encountering decreasing water depth (d) due to the sloped bottom. This interaction with the bottom leads to changes in $\frac{H}{gT^2}$ and $\frac{d}{gT^2}$. Within these equations H is the wave height, g the gravitational constant and T the wave period. Furthermore, this interaction has the potential to cause waves to exceed their breaking limits. When this occurs the dispersion relationship for an arbitrary water depth remains valid. The dispersion is presented in Equation 2.1, it must be noted that this relation is derived under the assumptions of irrotational flow, constant water depth, no current and linear, small waves [60].

$$\omega^2 = g \cdot k \cdot tanh(k \cdot d) \tag{2.1}$$

Hence, as the water depth decreases and reaches shallow water conditions, the wavelength will decrease. Under these conditions, the phase speed c decreases and approaches the group velocity $c_g$.

$$c = \sqrt{\frac{g}{k} tanh(k \cdot d)} \tag{2.2}$$

$$c_g = n \cdot c \tag{2.3}$$

with $n = \frac{1}{2}\left(1 + \frac{2kd}{sinh(2kd)}\right)$ and $k$ being the wave number.

In shallow water conditions the (linear) phase velocity of the wave becomes:

$$c = \sqrt{g \cdot d} \tag{2.4}$$

Differences in group velocity cause differences in local wave energy and amplitude [21]. The wave steepness increases as wave amplitude increases, causing instability and wave breaking.

Non-linear waves
It is crucial to recall that when analyzing the described issues within the well-dock, the free surface elevations within the well-dock can become irregular or even non-linear in sea state 4. By looking at Figure 2.1 and assuming a wave period of 10.0 s in water depth of 2.65 m, non-linearity occurs when the wave heights exceeds 1.0 m. As a result, directly applying linear wave theory-based equations may lead to underestimate or overestimate the outcome.

The wave dispersion relation is derived from linear wave theory under the assumptions of irrotational flow, linear waves, constant water depth and no current [60]. However, within the well-dock many of these assumptions become invalid. For example, the slope within the dock causes the mean water depth to vary from one location to another. For this reason, within this report the Newton-Raphson method is used to determine the wave number $k$ and consequently the phase velocity and wavelength $\lambda$ (Equation: 2.5). These parameters will later be used in the determination of the powerflux. This will be done by using the following equation also containing the wave period $T$ and wave frequency $\omega$:

$$c = \frac{\lambda}{T} = \frac{\omega}{k} \tag{2.5}$$

### 2.1.2. Wave energy

The existence of a wave on the water surface indicates that water particles have been displaced from their original location to new positions. This displacement requires work to be done against gravity, thereby storing potential energy within the system. Additionally, as the wave particles move, they possess kinetic energy. For a harmonic wave with amplitude (a) with a certain density ($\rho$) this potential and kinetic energy over one period is determined with the following equations [21]:

$$E_{potential} = \frac{1}{4}\rho g a^2 \tag{2.6}$$

$$E_{kinectic} = \frac{1}{4}\rho g a^2 \tag{2.7}$$

Note that the formulation of $E_{kinetic}$ employs expressions for $u_x$ and $u_z$ from the linear theory, which is accurate to second order wave amplitudes. Within the approximations of linear wave theory, $E_{potential} = E_{kinetic}$ holds. The total time-averaged wave induced energy density for regular waves $E = E_{potential} + E_{kinetic}$ is calculated Equation 2.8.

$$E = \frac{1}{2}\rho g a^2 \tag{2.8}$$

It can be seen that the total wave energy is proportional to the amplitude squared; therefore, it is a second-order property of the wave, estimated using the results of linear wave theory.

In the event of irregular waves, where the surface elevation is viewed as the summation of numerous harmonic (regular) waves, the variance, which is proportional to the wave energy, can be utilized. By employing Fast Fourier Transform (FFT) on the measured signal, the amplitude spectrum can be determined. The wave energy can be calculated using Equation 2.9 [21]:

$$E(f) = \rho \cdot g \cdot E_{variance}(f) = \rho \cdot g \cdot \sum_{i=1}^{N} E\{\frac{1}{2}a_i^2\} \tag{2.9}$$

### 2.1.3. Wave energy transport

As waves travel across the ocean surface, they transport both potential and kinetic energy. To compute this energy transport, commonly referred to as energy flux, the following formulas are used to quantify this amount of energy transport per unit time per unit crest length [21][17].

$$P_{energy} = \left(\frac{1}{2}\rho g a^2\right)\frac{1}{2}\left(1 + \frac{2kh}{sinh(2kh)}\right)\frac{\omega}{k} \tag{2.10}$$

or, since $E = \frac{1}{2}\rho g a^2$ $(J/m^2)$ and $c = \frac{\omega}{k}$

$$P_{energy} = E \cdot n \cdot c \tag{2.11}$$

with $n = \frac{1}{2}\left(1 + \frac{2kh}{sinh(2kh)}\right)$

Note that the propagation speed $n \cdot c$ in this expression precisely equals the group velocity $c_g$. The term ”group velocity” is frequently used interchangeably for either the group velocity itself or the energy transport velocity. Hence, it is conventionally accepted to write [21]:

$$P_{energy} = E \cdot c_g \tag{2.12}$$

Where, the group velocity $c_g$ is now written as:

$$c_g = \left(\frac{1}{2} + \frac{kh}{sinh\,(2kh)}\right)\frac{\omega}{k} \tag{2.13}$$

The meanings of the parameters are listed below:

$h =$ water depth $(m)$

$k =$ wave number $(m^{-1})$

$\omega =$ wave frequency $(rad/s)$

With this formula the group velocity can be calculated for both deep and shallow water [21]:

$$c_g = \frac{c}{2} \quad \text{(deep water)} \tag{2.14}$$

$$c_g = c \quad \text{(shallow water)} \tag{2.15}$$

To calculate the energy attenuation due to an implementation of a Wave Attenuation Solution (WAS), the difference in power flux ($J/s/m$ or $W/m$) has to be calculated between the measured inflow and outflow [21]. During the simulation, it is assumed that the measured free surface elevation within the dock will be irregular, non-linear and in shallow water conditions. Therefore, the measured signal is analyzed by examining each regular component obtained from a FFT analysis. For each component, the wavenumber and the corresponding phase velocity can be calculated using the Newton-Raphson method. In the end, this approach will be used to determine the total power flux for each component by taking the summation.

$$P_{attenuation} = E_{inflow} \cdot c_{g_{(inflow)}} - E_{(outflow)} \cdot c_{g_{(outflow)}} \tag{2.16}$$

$$P_{attenuation} = \frac{1}{2} \cdot c_{g(inflow)} \cdot \rho \cdot g \cdot a^2_{inflow} - \frac{1}{2} \cdot c_{g(outflow)} \cdot \rho \cdot g \cdot a^2_{outflow} \tag{2.17}$$

Throughout this report, this formulation will be employed to assess the wave attenuation performance of various wave attenuation designs and ultimately optimise these designs to achieve maximum wave attenuation by means of reflection or damping.

### 2.1.4. Wave reflection

Now that we understand how free surface waves form, break and energy transport, we can explore ways to reduce these motions and energy before they reach the well-dock. This reduction in energy can be achieved through reflection or dissipation, such as damping. In this paragraph, we specifically delve into the method of wave reflection.

The difficulty in predicting wave reflection is resolving the energy balance equation [9][45], which includes wave reflection, dissipation and transmission (both through and over the structure or object). Thus, achieving an accurate solution for the reflection coefficient requires considering parameters related to each of these important processes.

$$E_{wave} = E_{reflection} + E_{dissipation} + E_{transmission} \tag{2.18}$$

$$E_{attenuation} = E_{reflection} + E_{dissipation} \tag{2.19}$$

$$E_{attenuation} = E_{wave} - E_{transmission} \tag{2.20}$$

By looking at Equation 2.18 and applying the linear wave theory, Shi et al. [46] convert this energy balance into a equation with wave heights ($H$). This only applies when it is assumed that the reflection and transmission have the same period as the incident wave then the following equation can be used:

$$H_0^2 = H_r^2 + H_d^2 + H_t^2 \tag{2.21}$$

Where $H_0$ is the incident wave height, $H_r$ is the reflected wave height, $H_t$ the transmitted and $H_d$ the wave height which is relevant to the (mechanical) damping. By utilizing these parameters, several coefficients can be determined. Firstly, the reflection coefficient can be calculated with $K_r = H_r/H_i$. This equation represents the ratio between the reflected wave height ($H_r$) and incoming wave height ($H_0$). The calculation of the reflected wave height is conducted by using the wave splitting theory [34]. It must be noted that the wave reflection is not determined within the scope of this thesis.

Secondly, the transmission coefficient: $K_t = H_t/H_i$, which is the ratio between the transmitted wave height ($H_t$) and the incident wave height, can be calculated. This equation originates from Macagno's work [32] utilizing the linear wave theory. Lastly, the dissipation coefficient ($K_d$) is dependant upon the type of energy dissipation device or method employed.

Controlling the wave height of the transmitted wave can be achieved by modifying the reflection coefficient ($K_r$) of the implemented structure. This coefficient is typically influenced by surface slope, roughness, porosity, geometrical slope of the structure, still water depth and incident wave conditions.

Another way of controlling the wave height is to influence the phase angle of the wave. When two waves are in phase, their combined profile is the sum of both components (constructive interference). Conversely, when their phases are shifted by 180°, the resulting profile is lower or even cancelled (destructive interference). In the end, phase interaction can be utilized to reduce wave height for two progressive waves with a phase lag of $\pi$.

### 2.1.5. Wave energy dissipation

Wave motion involves the disruption of a system from its stable equilibrium. When the system is in a distorted state, it possesses more potential energy compared to when it is in equilibrium. Within waves, there is a constant exchange of energy occurring through the conversion of potential energy into kinetic energy and vice versa.

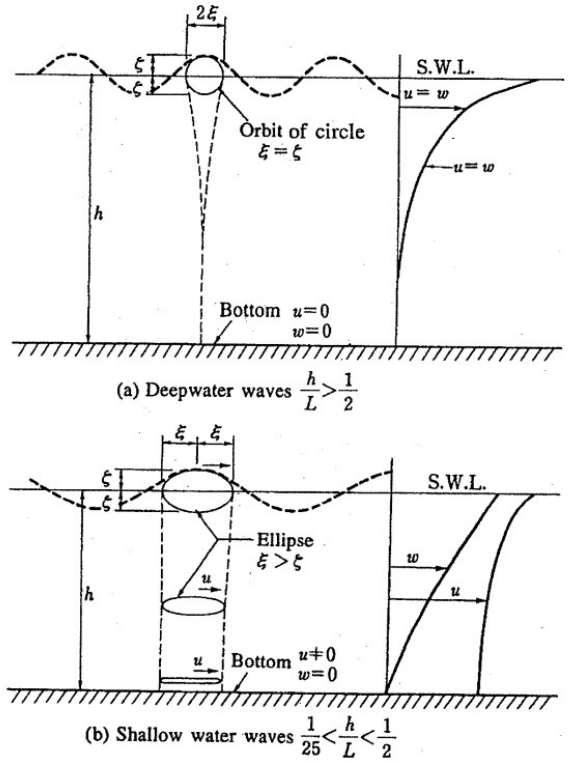


**Figure 2.2:** Velocity distribution for deep and shallow water waves [43]

Figure 2.2 illustrates velocity distributions within waves. In deep water waves, particle motion forms a circular orbit, with horizontal ($u$) and vertical ($w$) velocities being equal in both directions ($u, w$) and zero at the bottom. In contrast, shallow water waves exhibit an elliptical particle motion, with zero vertical velocity ($w$) at the bottom and nearly constant horizontal velocity ($u$).

The distribution of kinetic energy within waves across the water depth depends on the ratio between water depth ($h$) and wavelength ($\lambda$). Increasing the water depth in relation to the wavelength enhances the concentration of kinetic energy near the free surface, as depicted in Figure 2.2 (a). On the other hand, increasing the wavelength will enhance the constant horizontal velocity along the total water depth. When examining the problem statement, this aspect may favor a submerged wave attenuation solution, as the velocity of shallow water waves within the dock is likely to remain constant. This means there would be no decay in wave energy when submerged.

By looking at the distribution of kinetic energy within waves, the absorption of this energy can be achieved through various methods. One method is when water has to flow through or around objects. As the fluid moves through these objects, turbulence dissipates wave energy into heat. A second method involves internal work within structures or systems, such as floating or submerged mattresses and motion of submerged objects like pitching flaps. Lastly, wave energy can be dissipated through wave breaking, a phenomenon effectively utilized by wave breakers near coasts and harbors.

## 2.2. Free Surface Oscillations in an LPD Well-dock

This part of the literature review aims to examine the methodologies employed for modelling hydro-structural interactions within a well-dock of an LPD. The results show that the existing papers are characterised by conflicting and different outcomes. Moreover, the focus of the selected literature tends to be on the analysis and modelling of wave motions only. So, limited attention is given to engineering solutions addressing the undesired sloshing effects. The findings from these papers provide helpful information about how waves travel inside well-docks, but they also show that there are disagreements, conflicts, and different approaches. Subsequently, further research is needed that considers essential factors and aims to compute a simplified model with low computational time. Eventually, this model can be used to develop wave attenuation solutions which will enhance the operability of amphibious operations in higher sea states.

As mentioned in the introduction, the wave motions inside a well-dock are influenced by the motions of the LPD itself and incoming waves at the stern [54]. Eventually, these motions cause sloshing and free surface oscillations [52]. This might have two possible effects: firstly, the LCVPs inside the dock will get slammed by waves making them more difficult to control. Secondly, extreme wave motions could cause impacts between LCVPs and the LPD inner walls and bottom [7].

The primary goal of the second part of the literature review is to look into the various methods used to model complex wave motions inside a well-dock of an LPD. In this way, these findings can be used further on within this thesis, to set-up the CFD-model and to design and optimise the wave attenuation solutions. Therefore, the main question within this literature review is:

***"How can hydrodynamic modelling be used to compute the free surface oscillations within a well-dock of an LPD in varying sea-states?"***

To answer this question, the following sub-questions will be answered:

1. Which environmental input factors are required for modelling the wave motions within a well-dock?
2. What is the modelling approach for simulating wave motions in a flooded well-dock of an LPD?
3. What is the effect of well-dock design on the wave motions inside a well-dock?

### 2.2.1. Modelling set-up

In Figure 2.3, the results from the found existing literature are shown. The main purpose of this table is to show the hydro structural modelling choices of each paper in relation to well-docks. A detailed description of each modelling choice is presented in the following subsections.

| | **Environmental modelling (waves)** | | **Structure modelling (LPD)** | | **Fluid modelling (beach ramp)** | **Hydrodynamic/structural modelling** |
|---|---|---|---|---|---|---|
| **Author** | *Wave direction* | *Wave type* | *DOF* | *Forward speed* | X | X |
| Yoon, S.H. et al. | Multi-directional | Irregular waves | Pitch & heave | Yes | Yes | One-way coupling |
| Wang, Z. et al. | Head seas | Regular waves | Fixed | No | No | None |
| Wang, G. et al. | Head seas | Regular waves | Fixed | No | No | None |
| Cartwright, B. et al. | Head seas | Regular waves | Pitch & heave | No | Yes | One-way coupling |
| Hopman, H. et al. | Multi-directional | Irregular waves | Free | Yes | Yes | Full-coupling |
| Bass, D. et al. | Head seas | Irregular waves | Fixed | Yes | Yes | None |
| Cartwright, B. et al. | Head seas | Regular waves | Pitch & heave | No | Yes | One-way coupling |
| Groenenboom P.H.L. et al. | Head seas | Regular waves | Pitch, heave & surge | No | Yes | Unknown |
| Gang, X. et al. | Multi-directional | Regular waves | Pitch, heave & surge | No | Yes | One-way coupling |

**Figure 2.3:** Summary of different modelling choices in existing literature

#### Environmental input modelling

According to the literature, the RNN is currently conducting amphibious operations in conditions up to sea state 4 [59][7] [22]. These sea states are composed of two main elements: short-period wind sea and long-period swell waves. The size of wind waves is affected by factors like the strength of the wind and how long it persists [21]. Swells however are waves that have gained sufficient energy to extend beyond their location of origin and they no longer require additional wind to push them forward [21]. These long and short-period waves could have different effects on the shaping of the overall motions of both the LPD and the fluid within the well-dock.

For an accurate consideration of how these waves affect ship-water interaction, it's crucial to incorporate them both into the model. Therefore, most of the research papers use a very similar approach to include this environmental input factor. This method involves the utilization of irregular waves with varying periods [59][22][3][6]. The other method entails the use of regular waves [54][52][6][3][18][56].

In addition to considering wave types, such as regular and irregular waves, it is essential to include wave direction, often referred to as sea direction. From the papers examined, three different approaches were applied: head seas, multi-directional, and following seas (Figure 1.5). During standard well-dock operations the LPD positions itself in head waves [54]. Several papers use an incoming wave direction of 180° [54][6][21]. However, other research papers also take into account the existence of multi-directional waves, including head seas, bow quartering seas, beam seas, and quartering seas [22][56]. As a result, these various wave directions result in multi-degree motions of the LPD.

To create an accurate model, it is crucial to incorporate all the relevant environmental input factors. As mentioned by Hopman et al. [22], amphibious operations occur along the coast in conditions up to sea state 4, which involve the presence of wind sea, swell, or a combination of both. To model these irregular waves, the usage of the super-position principle of regular waves can be introduced.

The LPD's position with respect to the incoming waves is crucial. Irregular uni-directional head waves in the model lead to the most precise representation of the real amphibious operation. Early research conducted by COMMIT in 2001 showed that long wave periods (T = 11.4 s) result in the highest wave heights within the dock. For this reason, the research focuses on wave periods close to the natural period of the LPD, which is comparable to regular swell waves.

### Hydrodynamic modelling

To model the wave motions within an LPD's well-dock accurately, it is vital to develop a model for the LPD structure in sea water. The characteristics of this model and its behaviour in seawater can be represented through various methods. In this literature review three methods have been identified: in the first method the LPD was totally fixed, so no ship motions were possible [54][52][6]. In the second method, it was free to move in pitch, heave and surge, but restrained in roll, yaw and sway [18][56]. In the last method, the LPD has held a fixed location in the fore and aft (front and back of the LPD) and was free to move in pitch and heave direction [59][7][6]. For understanding means, these ship motions can be seen in Figure 2.4.

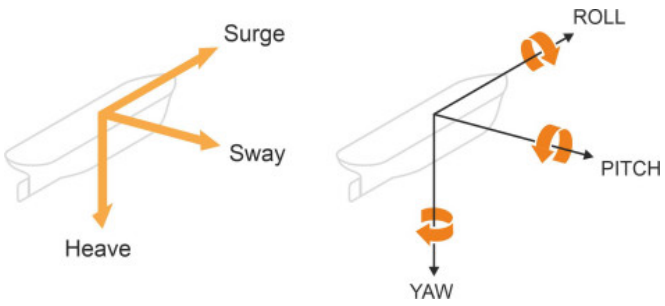


**Figure 2.4:** Ship's degrees of freedom [37]

Besides the Degree Of Freedom (DOF) of the LPD, also the forward velocity plays a role. When a ship moves forward in water, particularly one with a broad, submerged transom stern, such as an LPD, it can cause forward-oriented wave breaking, commonly referred to as stern waves. This phenomenon takes place right behind the transom stern, located at the rear of the ship [57]. Moreover, this movement generates a turbulent wake behind the LPD [22]. These two wave phenomena are illustrated in Figure 2.5.

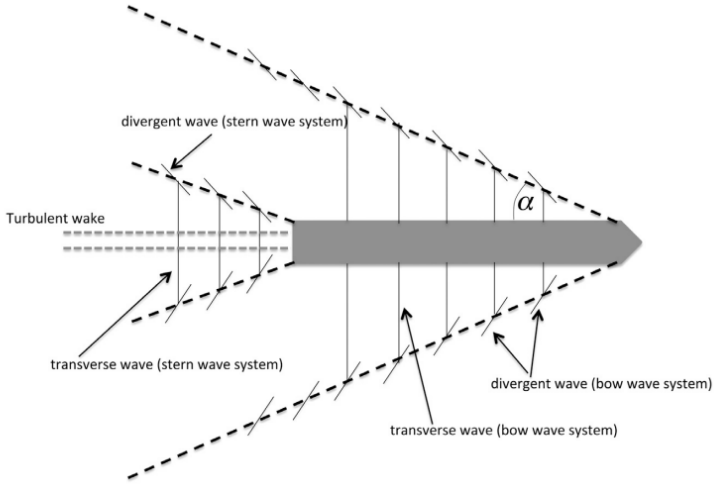


**Figure 2.5:** Location of stern waves and turbulent wake [57]

The generation of wakes and stern waves results in additional waves appearing within the well-dock [22]. The forward speed increases in the relative motion between the well-dock and the water's surface. This is primarily due to the vertical motion of the stern, where the extended well-dock gate is located. Some research papers have incorporated this forward speed into their numerical models or model experiments, as shown in Yoon et al. [59] and Hopman et al. [22]. In contrast, the majority of papers chose not to account for the forward speed, mainly due to the characteristics of specific amphibious operations in which the LPD remains stationary without any forward movement [54][52][7][6][18][56].

The impact of adding forward speed is further evaluated through experimental validation. From the outcomes of these experiments, we can draw the following conclusions: Firstly, the experimental data from Bass, et al. [3] and Yoon, et al. [59] indicate a noticeable trend of reduced relative motion at the stern when forward speed is added. This relative motion is defined as the distance between the well-dock entrance and the water surface with increased speed. Secondly, there appears to be a significant sheltering effect on the waves when moving with speed. As a result, fewer waves travel into the dock. Lastly, the results of the model experiments of Hopman, et al. [22] show that the waves generated in the well-dock were highest at zero speed. As a result, it can be concluded that incorporating forward speed into the model will not increase the wave motions within the well-dock. Ultimately, to model the scenario where wave motions are at their most severe, it is recommended that the LPD remains in a stationary position without any forward speed.

### Computational domain set-up

Modelling the fluid within the well-dock is done with different boundary conditions (BC). The primary difference in BC lies in the inclusion or exclusion of a beach ramp, which causes either reflection or damping effects from incoming waves into the dock. Both effects influence the location with the greatest wave response. An illustration of such beach ramp can be seen in Figure 2.6.

**Figure 2.6:** Example of a beach ramp at the end of a well-dock [59]

Different papers included the ramp and the damping effect of these ramps on incoming waves [59][6][22] [3][7]. These papers describe that the wave motions near the entrance of the well-dock are considered one of the most critical points and give the most chance of collision during amphibious operations. In papers in which beach ramps were excluded such as Wang, Z. et al. [54] the largest wave responses were found near the rear wall of the well-dock, primarily due to reflections from the back and side walls.

When looking at the design of (numerical) beach ramps, it is found that the damping effect of these ramps varies depending on their shape, porosity and angle with the well-dock floor [59]. This variation can also be seen in the findings of different research papers. For example, Bass et al.[3] stated that the most effective wave absorber was the vertical wall (slope is 90°) with 20% porosity, followed by a sloping ramp with 20% porosity. Furthermore, the absence of a ramp (thus vertical wall) will result in the largest wave responses due to reflective waves [3].

### Hydrodynamic/structural modelling

Hydro-structural modelling is the interaction of some movable structure with an internal or surrounding fluid flow [5]. This type of interaction also applies to the seawater inside the well-dock, the well-dock's sidewalls, the sloped beach ramp and the (sloped) bottom itself. In case of the LPD, there can be either one-way or two-way coupling between the vessel and the fluid within the dock.

Upon reviewing papers concerning wave motions within a dock, conflicting results were identified. On the one hand, several papers state that the ship motions of the LPD do not influence the wave motions within the well-dock. This is shown by a coupling analysis in studies by Bass et al. [3], Wang, Z. et al. [54], and Wang, G., et al. [52]. On the other hand, papers by Cartwright et al. [6] and Yoon et al. [59] state that the wave motions inside the well-dock are indeed influenced by the motions of the LPD. Therefore, coupling between the LPD ship and wave motions within the dock is present.

#### Effect of well-dock design

Well-dock design has a significant impact on wave motions inside a well-dock. Some design features that have a notable impact are the slope of the bottom and the water depth [59][3][6]. In the literature, contradicting results are obtained when the effects of a sloped and flat bottom are compared. On one hand, results indicate that an inclined slope in the well-dock floor may result in larger waves compared to a flat floor [6]. This observation aligns with the results obtained by Bass et al.[3], which led them to the conclusion that a sloped well-dock bottom would lead to higher wave motions inside the well-dock. In contrast to these findings are the results from Yoon et al. [59]. These findings indicate that a sloped bottom leads to a reduction in the wave's entry speed. As a result, the outflow rate from the well-dock is lower in comparison to a flat floor. Consequently, the wave height at the well-dock entrance remains relatively low due to the sloping [59].

### 2.2.2. Conclusions

This literature review investigated the different modelling methods and choices used in different papers. The focus hereby is on: domain set-up and hydrodynamic modelling of wave motions in well-docks of an LPD during amphibious operations. In Figure 2.3, the results from the systematic method described in this part of the literature review are shown. The main purpose of this table is to present the computational modelling choices of each paper in relation to well-docks and free surface oscillations. Different modelling choices, sometimes contradictory, were made in the existing research. This information will be used to set up the computational models and domains for this thesis.

Based on this review, it is concluded that hydrodynamic modeling withing a well-dock can be approached in various ways. Hereby, different elements come into play, such as environmental input factors, structural/fluid modelling, and the choice of one-way, two-way, or no hydro-structural coupling at all. These modelling options led to different and sometimes conflicting results. Firstly, when considering incoming waves, there is a choice between regular and irregular waves. Also, their direction can vary between unidirectional and multi-directional. In the context of the user profile of an LPD, unidirectional irregular head waves appear to be the most realistic choice for implementation in the model.

Secondly, by looking at structural and fluid modelling, the structure can be modelled with different degrees of freedom. Given the LPD's user profile, it is realistic to assume free movement in the heave and pitch directions, and the absence of forward speed. Regarding domain set-up, there are differing viewpoints when it comes to boundary conditions. The presence of a sloped beach ramp at the well-dock's end is decisive in determining the specific location of large wave responses. This due to constructive interference.

Lastly, the coupling between the LPD (structure) and seawater (fluid) within the well-dock has a major influence on wave motions. Based on the review of several papers, it can be concluded that one-way coupling, specifically the impact of LPD motions on the seawater within the dock, yields the most realistic outcomes. This is due to the heave and pitch motions of the LPD, which generate additional waves in the longitudinal direction within the dock.

# Part I

# Model 1: Free Surface Motions within an LPD Well-dock

# 3

# Methodology

The methodology to accomplish the main objective involves three parts: Part I consists of developing a numerical model (referred to as Model 1) that uses ComFLOW to simulate non-linear free surface oscillations within an LPD's well-dock. In Part II, a concept design is created with the use of system engineering techniques. Lastly, part III simulates the fluid-rigid body interaction between waves and the designed solution itself. The utilization of ComFLOW within this report is motivated below.

- Comprehensive analysis options available in both time and frequency domain, which results in better understanding of design optimisation.
- The inclusion of (possible) non-linear terms in the equations of motion for oscillating submerged objects and free surface elevations.
- The simulation of non-linear free surface motions, such as steep and breaking waves, in both intermediate and shallow water conditions.
- The caption of non-linear processes that lead to changes in wave shapes and energy distribution of free surface motions.
- The capability to simulate complex two-way coupling of non-linear free surface motions and the interaction with submerged (moving) objects.
- ComFLOW is a relatively easy programming language when compared to open source software like OpenFOAM, allowing even beginners to use it.
- ComFLOW's results can primarily be improved by adjusting two main parameters: the time step $\Delta$t and the grid size $\Delta$x,y,z.

## 3.1. ComFLOW Set-up Strategy

Before using CFD to compute free surface motions in a well-dock, several modelling choices must be determined. The results supported with the outcome of Section 2.2 are listed below in several steps:

### 3.1.1. System to model

In Figure 3.1, the complete boundary of the system is highlighted in red. This includes an LPD and its inner well-dock. The primary objective of the model is to simulate the free surface motions occurring within the well-dock.


**Figure 3.1:** Total system with boundaries [10]

### 3.1.2. Input and output of the system

With the system and boundaries established, the inputs and outputs can be identified. The results are depicted in Figure 3.2, where inputs are represented in green and outputs (reactions) are indicated in red.

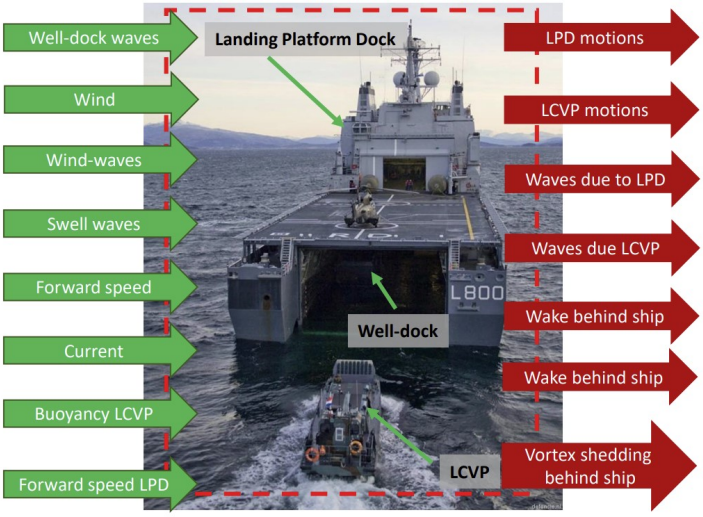


**Figure 3.2:** Input and outputs of the system [10]

### 3.1.3. Components and connections of the system

In the total system, the relevant components and connections are:

- Inner walls of the well-dock;
- Sloped bottom of the well-dock;
- Sloped beach ramp inside the well-dock;
- The well-dock gate door;
- The landing vessel;
- The wing-tanks;
- The bulkhead inside the well-dock (longitudinal direction).

Additionally, the relevant connections that can be identified are:

- The bottom of the well-dock and the fluid within this dock;
- The sloped beach ramp at the end of the well-dock and the fluid within this dock;
- Sloshing interactions in the well-dock;
- The stern of the LPD and the well-dock gate door;
- The well-dock door and the open sea.

### 3.1.4. Items to model

Based on several research papers (Section 2.2) describing wave motions inside a well-dock, the following items will be modelled:

*Components:*

- (Sloped) bottom of the well-dock;
- Sloped beach ramp inside the well-dock;
- The well-dock gate door.

*Connections:*

- The bottom of the well-dock and the fluid within this well-dock;
- The sloped beach ramp at the end of the well-dock and the fluid within this well-dock;
- The well-dock door and the open sea.

### 3.1.5. Model simplifications

The numerical model can be further simplified by disregarding certain inputs and outputs.

*Environment:*

- Unidirectional regular head swell waves on the LPD;
- The sea-state remains stationary throughout the amphibious operation (launch & recovery), spanning a 3-hour interval. Hence, only a single wave component, defined by a constant wave period (T) and wave height (H), is employed in the calculation of the LPD motions using known RAOs.
- An average significant wave height ($H_s$) of 2.0 m, with a wave period of 11.4 s is chosen as dominant wave. This resembles long-period swell wave, which is tuned to the natural period of the LPD.

*Structure:*

- LPD (incl. well-dock): rigid body assumption;
- LPD is free to move in heave and pitch direction (2-DOF), so two-dimensional (2D) modelling;
- LPD is perpendicular to incoming regular head swell waves;
- Known well-dock dimensions (HNLMS Rotterdam);
- LPD has no forward velocity (stationary);
- Known Response Amplitude Operators (RAOs) of an LPD (HNLMS Rotterdam);
- Prescribed well-dock motions on the basis of known RAO-values.

*Fluid:*

- Assume one-way coupling (LPD-motions on the fluid within well-dock);
- Ignore turbulence in the well-dock (no viscous fluid);
- Ignore wake at the stern of LPD;
- Ignore the stern waves;
- Ignore diffraction and radiation effects at the stern of the LPD, near the entrance of the well-dock;
- Model hydrodynamics in 2D.

## 3.2. ComFLOW Domain Set-Up

In this section, all assumptions, restrictions, and modelling choices will be used to set up a numerical model in ComFLOW. This will include: boundary conditions, grid setup, geometry, and numerical settings.

### 3.2.1. Computational Domain & Boundary Conditions

The 2D model used in this setup is 350.0 m long with a water depth of 90.0 m, as depicted in Figure 3.5. For all simulations in Model 1, no wave input settings were used because the free surface elevations were generated purely by the well-dock motions. To mitigate wave reflection from the domain boundaries, a Generating and Absorbing Boundary Condition (GABC) has been integrated at both ends of the domain. This replaces the need for large dissipation zones, which usually requires more space than the primary wave-structure interaction region [50].

The water density is set at 1025.0 kg/m³ with a kinematic viscosity of $0.1^{-2}\ m^2/s$. Air is assigned a density of 1.0 kg/m³ and a kinematic viscosity of $0.1710^{-4}\ m^2/s$. Furthermore, Adams-Bashforth, a two-step explicit method is employed for the time scheme. Also an automatic time step adjustment function is utilized to satisfy the Courant-Friedrichs-Lewy (CFL) condition. To ensure stability, accuracy and reasonable computational time, the following values are used:

- Flow: 0.7 < CFL < 0.9
- Wave: 0.25 < CFL < 0.5

In Figure 3.3 and 3.4, the geometry of the well-dock from a technical drawing and the simulated geometry in ComFLOW are illustrated. The dimensions and properties are based on those described in Table 5 from Hopman et al. [22] and Liu et al. [30]. To enhance computational efficiency, the model is simplified using the assumptions outlined in the beginning of this section. It should be emphasized that the simulations in this report only consider the normal draft case, which is also mentioned by Hopman et al. [22].

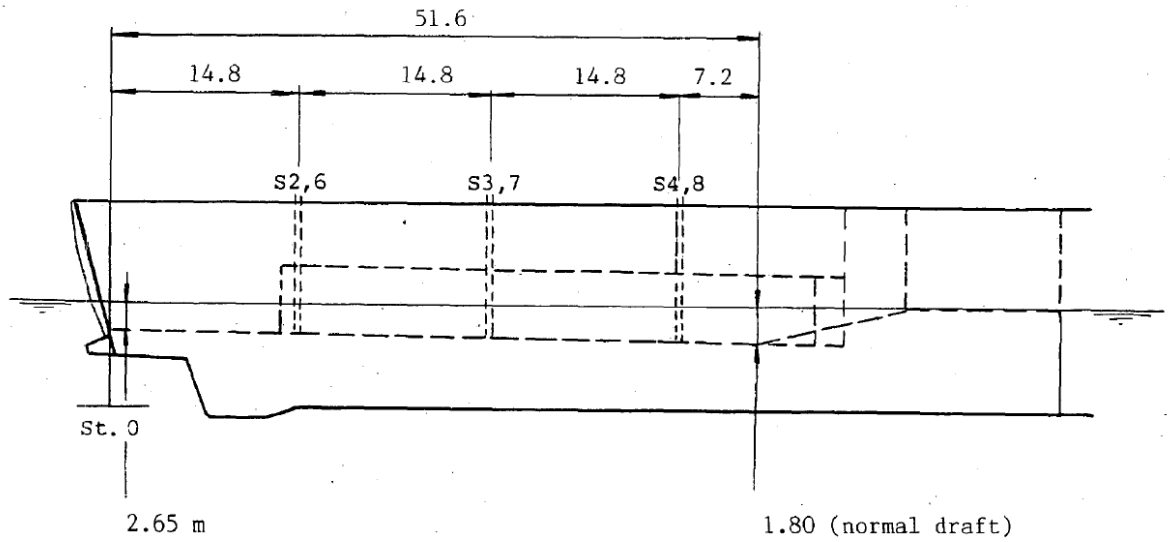


**Figure 3.3:** Well-dock dimensions LPD-1 and water depth (draft), hereby distances are in meters.

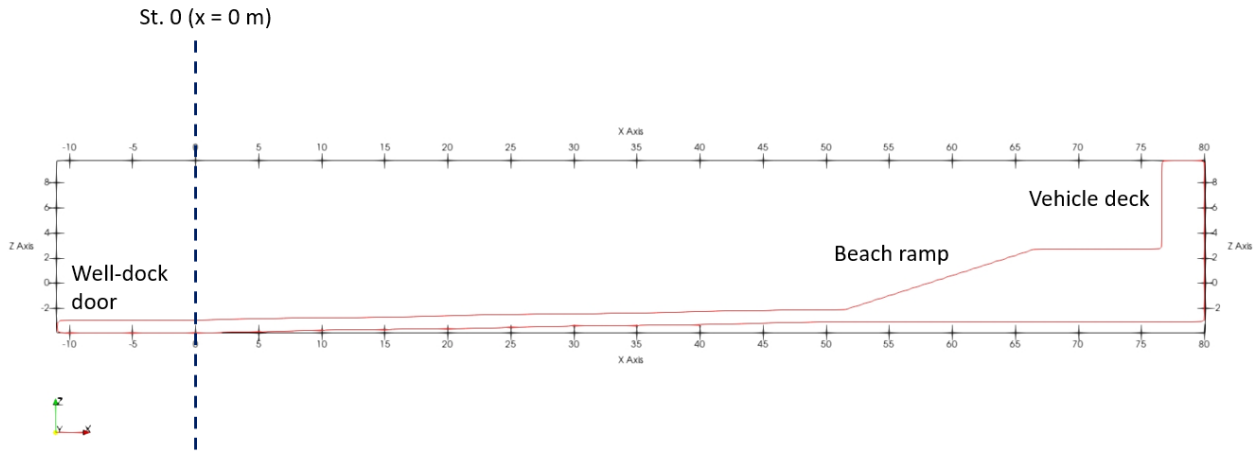


**Figure 3.4:** Well-dock geometry in ComFLOW, hereby distances are in meters.

### 3.2.2. Computational Grid

ComFLOW solves the Navier-Stokes equations with use of a computational grid. This grid system allows for multiple refinement levels, enabling local adjustments to enhance accuracy or optimise computational efficiency.

During the set-up of the general outline, several choices where made to improve stability and accuracy:

1. Level 1 grid refinement is used near the upper and lower parts of the domain, where minimal fluid motion and velocities are expected, typically in deep water conditions.
2. Level 2 refinement is used near the inflow and outflow boundaries to absorb waves generated by well-dock movements, both linear and non-linear.
3. Additionally, level 2 refinement is employed across the entire width of the domain near the free water surface.
4. To ensure a smooth transition to the highest refinement level 3, a level 2 refinement area surrounds the entire area of interest, including the well-dock with the free surface.
5. The most refined grid level, level 3, is placed within the well-dock, where the highest fluid- and object motions are expected.

The complete grid with refinement levels can be seen in Figure 3.5:

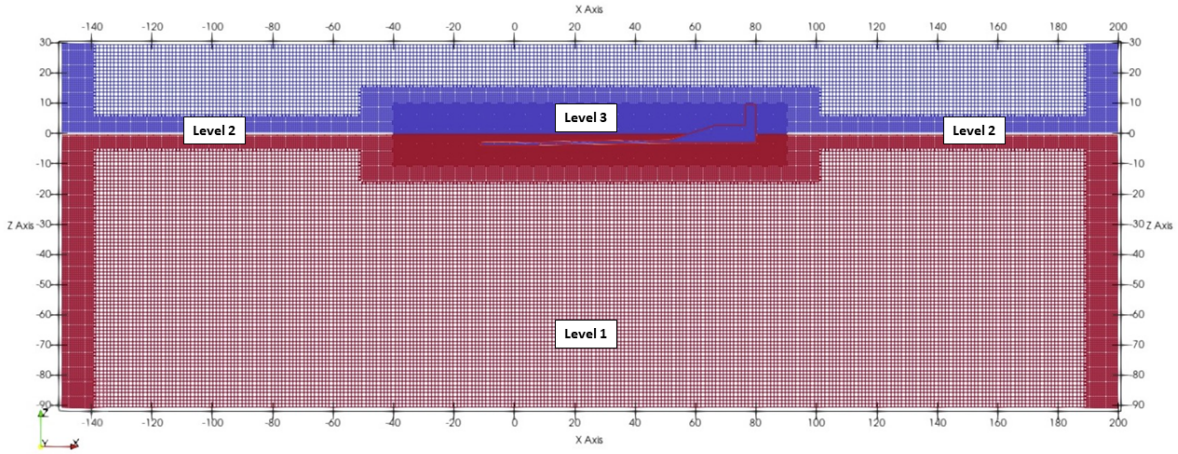


**Figure 3.5:** Grid outline with refinement levels

In the grid sensitivity study shown in Table 3.1, three grid sizes are tested to find the optimal refinement. The simulation uses LPD-1's known RAO curves and Center of Gravity (CoG) position, with 11.4 s waves and a significant height of 2.0 meters. These RAO values (amplitudes and phase angles) are input values for ComFLOW's forced oscillation motion function, resulting in longitudinal sloshing effects.

| Grid type | Finest $\triangle$x (m) | Finest $\triangle$z (m) | Total number of mesh cells (-) |
|---|---|---|---|
| A | 0.60 | 0.65 | 81,794.00 |
| B | 0.30 | 0.33 | 297,528.00 |
| C | 0.15 | 0.16 | 1,082,268.00 |

**Table 3.1:** Grid refinement levels

Figure 3.6 presents the free surface elevation at St. 0, the beginning of the well-dock. The results converge with a grid size of 580x in the x-direction, 1x in the y-direction, and 200x in the z-direction.

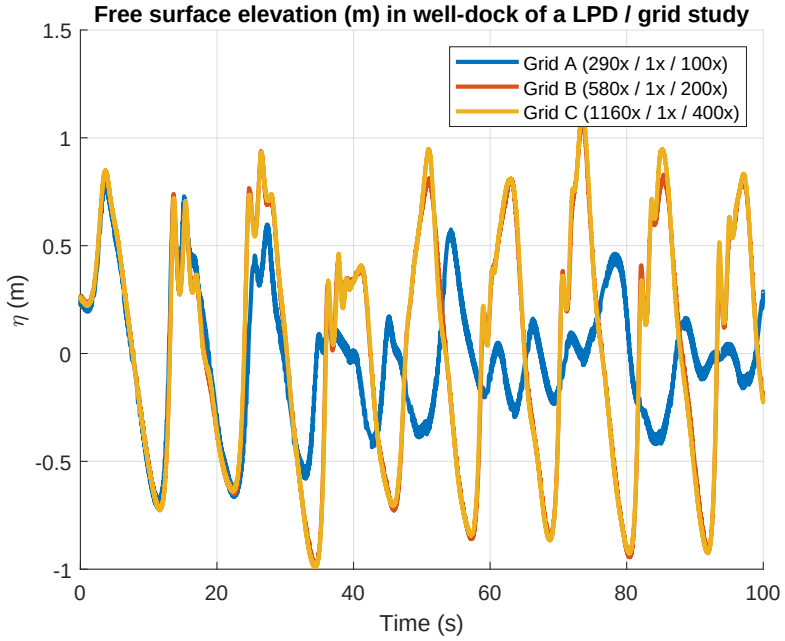


**Figure 3.6:** Grid sensitivity study

When examining grid types A and B, several observation can be made. Firstly, three distinct events are noticeable. From 0.0 to 13.0 s, the well-dock starts moving according to the prescribed motions derived from the LPD's RAO. This motion causes the initial wave to enter the dock due to its lowered bottom. Between 13.0 s and 24.0 s, another wave enters the dock, repeating the cycle. The third event occurring from 50.0 s to 100.0 s, shows a steady state situation.

Besides these three events, it is observed that the second measured wave elevation represents the incoming waves at St. 0 without the effect of wave reflection from the beach ramp. This also explains the variation in free surface elevation shape between event two (13.0 s < t < 24.0 s) and event three (50.0 s < t < 100.0 s).

### 3.2.3. Numerical Settings

ComFLOW employs two types of discretization schemes for convection. Firstly, the first-order upwind scheme (B2), and secondly, the second-order central scheme (B3). To examine the differences, the refined grid type C with scheme B2 was compared against the converged grid type B using both schemes B2 and B3. The results, shown in Figure 3.7, indicate that the differences are small. According to Van der Plas [50], the first-order upwind scheme provides more stable simulation results, so the B2 convection scheme is used.

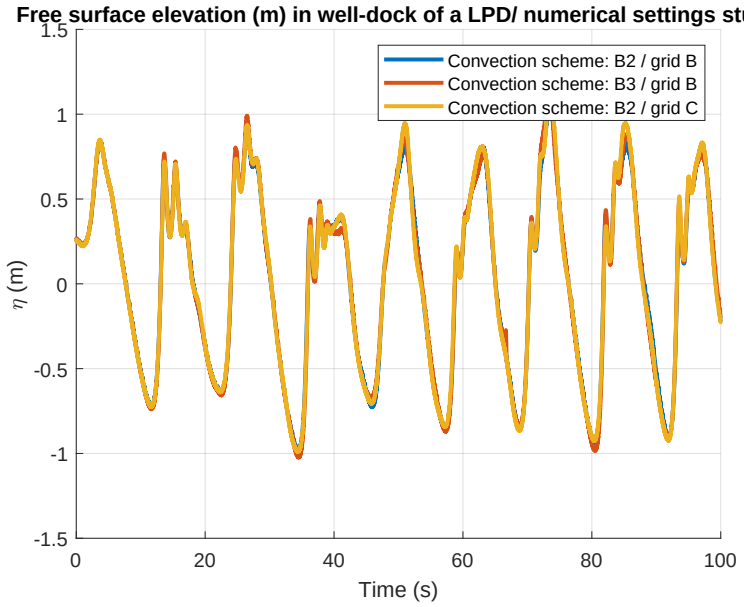


**Figure 3.7:** Convection scheme sensitivity study

Two more settings were investigated to assess their impact on the results. Firstly, the GABC-settings were examined, with adjustments made between the auto-tune option and manual adjustment by setting the coefficients. These coefficients are derived from the linear dispersion relation approximation and depend on factors such as water depth (h) and expected wave number (k) [50]. The outcome indicates there is no significant difference between both settings.

Secondly, two types of discretization schemes for diffusion are examined:

- A legacy scheme based on a staircase approximation of the geometry; and
- LS-STAG.

In the inner flow region, away from solid objects, both discretization schemes produce identical outcomes. However, the LS-STAG scheme offers a more precise estimation of viscous stresses in cells intersected by the geometry and is thus recommended for general applications [50]. Upon reviewing the results obtained with the LS-STAG scheme and grid type B, it is clear that this combination yields the most accurate results.

## 3.3. Verification Computational Model 1

To ensure accuracy of the final ComFLOW settings, a regular wave input is simulated. This wave is described with the Airy wave theory, which is also a wave model option in ComFLOW:

$$\eta(x,t) = A \cdot cos(\omega t - \kappa x + \phi) \tag{3.1}$$

Where: the amplitude (A) is 0.25 m, the frequency ($\omega$) 0.1 Hz, the wave number (k) 0.04 (deep water) and $\phi$ the phase equal to 0.01 rad. The phase is added to align with the numerical result, which is due to simulation start-up time.

The simulation uses the same settings as if the well-dock geometry were present. In Figure 3.8, the differences between the numerical and theoretical wave elevations after reaching a steady state (T > 50.0 s) is compared on location St.0. In addition, wave reflections are not considered in any of the test cases, as it is assumed that the GABC fully absorbs the transmitted waves. This assumption is verified as no wave reflection behavior is observed at any of the wave gauge locations during this numerical simulations.

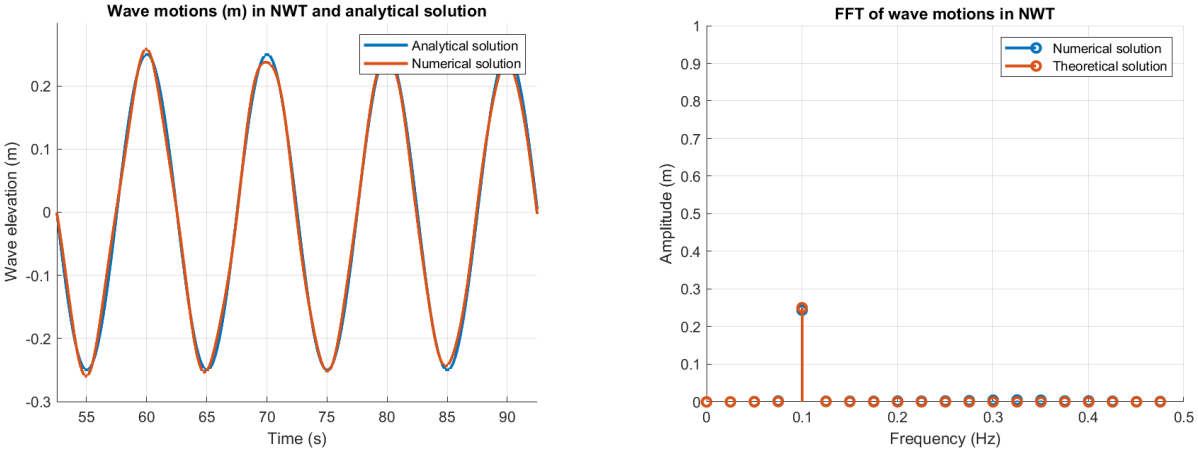


**Figure 3.8:** Verification Airy model with chosen settings, left time domain and right frequency domain

Figure 3.8 shows that the percentage error when looking at the maximum and minimum wave height is approximately 2.5%. For this reason, wave reflections are not considered in any of the test cases with the same wave properties.

This error percentage could be further reduced because the input wave starts from the left side where grid level 2 is present. In the actual simulations, the wave is generated in the more refined level 3 grid area. Because of grid level differences minor numerical damping and a slight decrease in wave amplitude could occur.

# 4

# Results & Discussion

In this chapter, the free surface elevations will be examined using the verified ComFLOW model. The primary objectives of analysing the surface motions are outlined below:

1. Understanding the fundamental mechanisms governing surface motions within a moving well-dock.
2. Graphing the outcomes in both time and frequency domains to determine their characteristics and properties.
3. Approximate the measured elevations using a mathematical function for subsequent utilization in Model 2.

## 4.1. Free Surface Elevations Within Well-Dock

In the upcoming paragraphs, 2D images of the free surface elevations within a well-dock will be examined in both space and time domain. These simulations were performed with the modelling settings as described in Chapter 3.2. The images show a 2D intersection of the well-dock, whereby red indicates seawater and blue indicates air. The blue object with the thin red-outline depicts the entire dock. St. 0 is indicated with a vertical white line at the location x = 0.0 m.

The final results of the measured surface elevation are plotted in time domain. These graphs are used to calculate the Root Mean Square (RMS), which indicates the overall wave elevation throughout the length of the well-dock.

### 4.1.1. Time-space domain analysis

**t = 0.0 s**

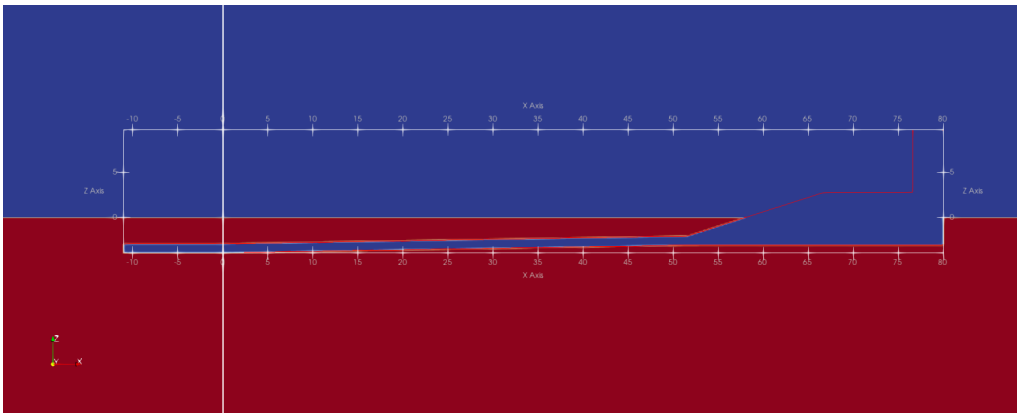

**Figure 4.1:** Free surface elevation at t = 0.0 s

At this point in time the LPD is not moving. The draft in the well-dock is set as detailed in Figure 3.3, with a maximum depth of 2.65 m at St. 0 and 1.80 m near the beach ramp (”normal draft”). ComFLOW settings dictate that the geometry is situated at the maximum amplitude of the prescribed motions. In our scenario, this equates to the highest combined motion amplitude in both pitch and heave directions. Consequently, the motion oscillates around a mean water depth of 2.65 m at St. 0.

**t = 2.0 s**

The geometry starts motion in accordance with the prescribed heave and pitch input data. Consequently, the bottom of the well-dock descends (negative z-direction), causing a drop in free surface. This leads to a relative disparity in the free surface levels between the outer and inner part of the well-dock.

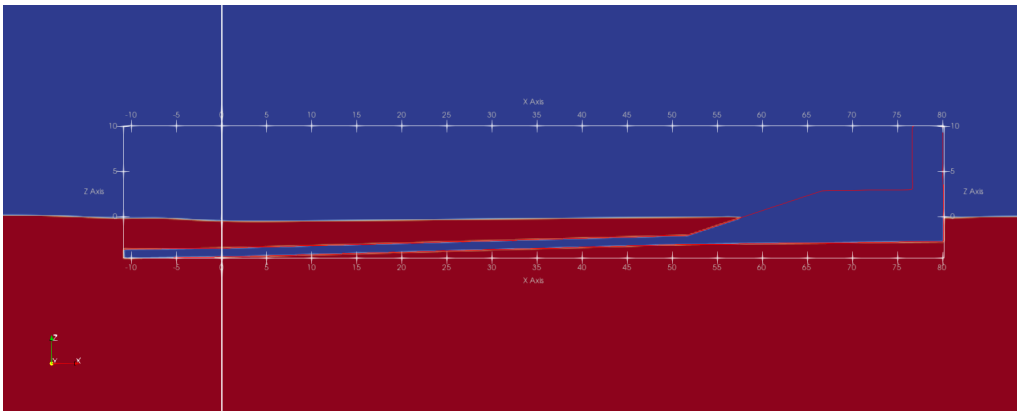

**Figure 4.2:** Free surface elevation at t = 2.0 s

### t = 3.6 s

Due to different surface levels, waves enter the dock from higher elevations and propagate towards the beach ramp at x = 51.6 m. Meanwhile, the bottom of the well-dock rises (positive z-direction) due to its oscillating motion. Consequently, this tilts the bottom, pushing the wave further into the dock. After 8.0 s, the dock reaches its maximum amplitude in the opposite direction before reversing its movement.

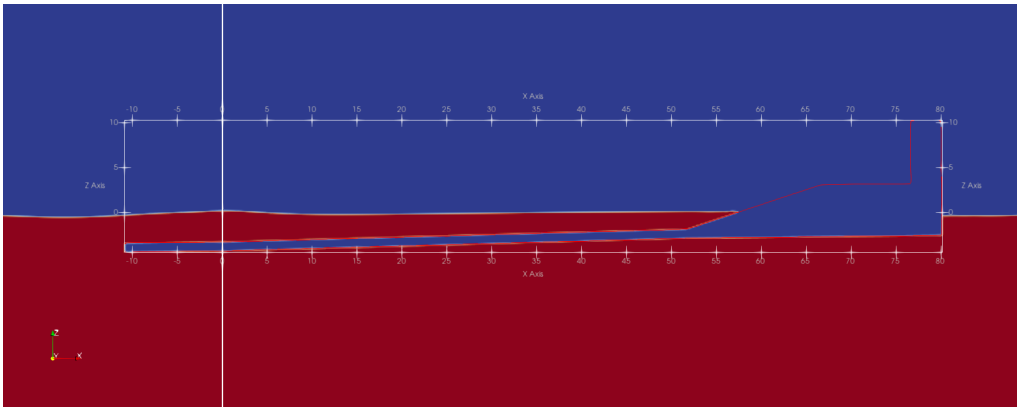

**Figure 4.3:** Free surface elevation at t = 3.6 s

### t = 11.6 s

At this time step, the cyclic process repeats itself. Once more, the disparity in surface levels generates a wave that rolls into the dock due to the relative difference in surface elevation.

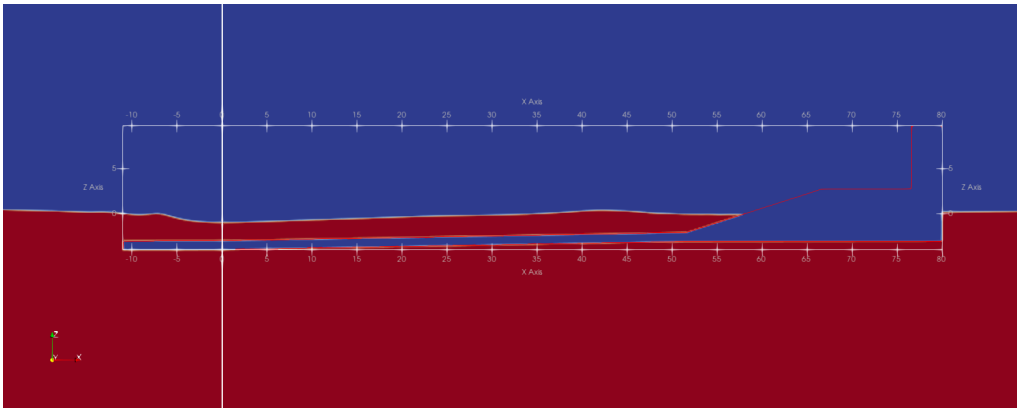

**Figure 4.4:** Free surface elevation at t = 11.6 s

**13.0 s < t < 24.0 s**

The second cycle unveils a more pronounced free surface motion. When the bottom reaches its maximum downward amplitude, waves begin to roll into the dock again. A wave train with three crests, decreasing in height, becomes noticeable as it travels deeper into the dock.

It is important to note that as the first wave passes St.0, the bottom begins to move in the opposite direction (positive z-direction). Consequently, the water depth becomes even shallower and the waves are being pushed further into the dock toward the beach ramp.

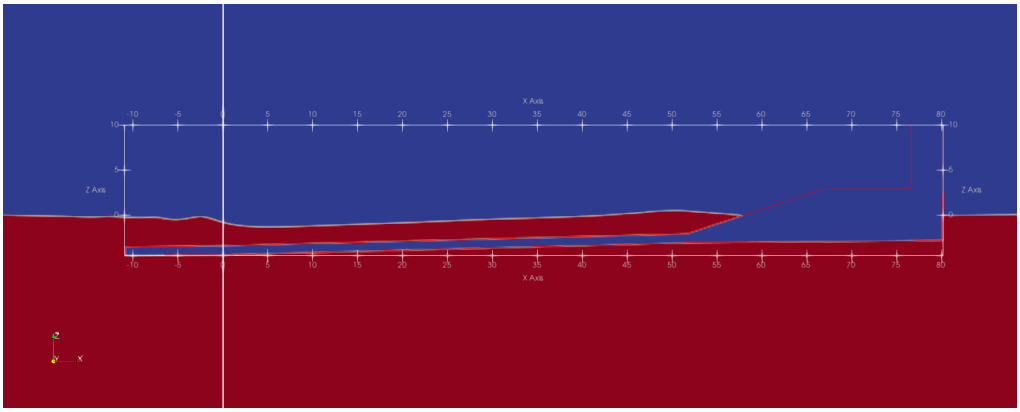

**Figure 4.5:** Free surface elevation at t = 13.0 s

As the well-dock rises, the water depth decreases, adding to the existing slope. Figure 4.6 illustrates this phenomenon by the presented breaking limit $\left(\frac{H}{d} = 0.78\right)$, eventually the shoaling effect leads to wave breaking. This event is observed in the image below at t = 18.5 s.

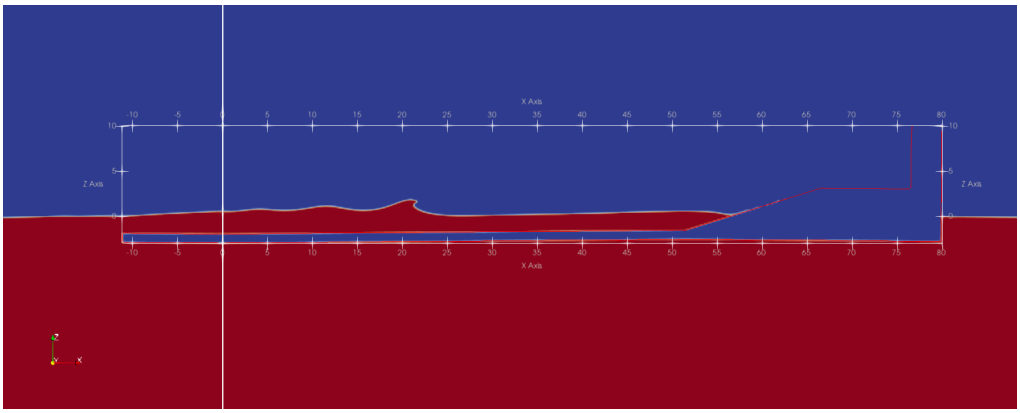

**Figure 4.6:** Free surface elevation at t = 18.5 s

**t > 24.0 s**

From this point on, the cycle described at t=13.0 s repeats itself. Following this cycle, the graph's shape changes due to the superposition of reflected waves from the beach ramp. Eventually, these waves interact with the incoming waves at location St.0, leading to an increase in wave height. This stabilizes into a steady-state after a period of 90.0 s.

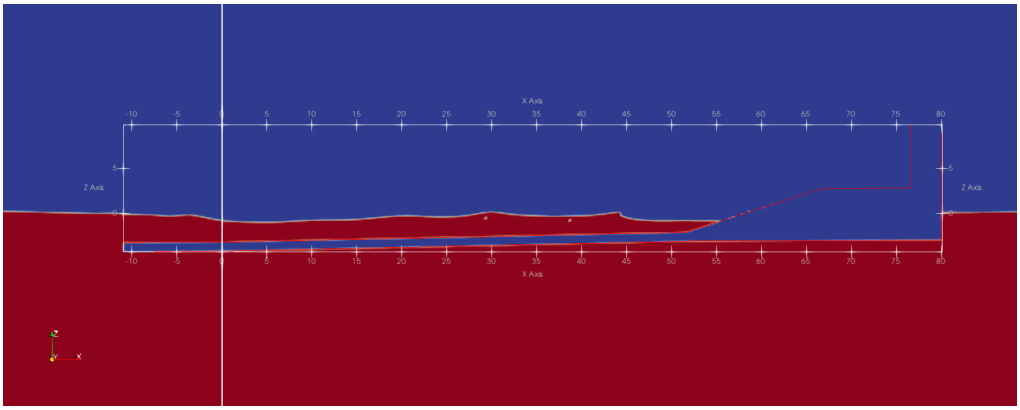


**Figure 4.7:** Free surface elevation at t = 24.0 s

### 4.1.2. Time domain analysis

For further analysis, one wave cycle (sample) from the wave record is selected to approximate the wave for use in Model 2. The wave profile must remain uncontaminated by interference from the beach ramp located at x = 51.6 m. Therefore, it is assumed that after one complete cycle within the well-dock, the first measured wave represents the fully developed surface elevation (13.0 s < t < 24.0 s). Moreover, considering the distance of the dock and the phase velocity of these longer period waves, it is assumed that the reflected wave does not interfere with the measured signal at St.0.

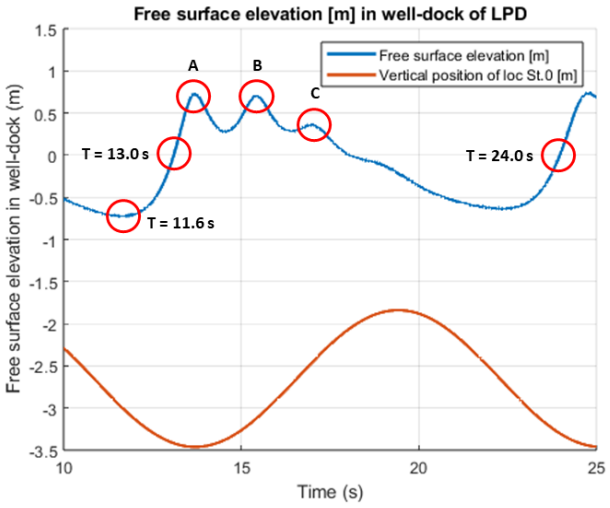


**Figure 4.8:** Free surface elevation and vertical position of location St.0 (time domain)

The events described in Figures 4.1 to 4.7 are also notable when measuring the surface elevation at location St. 0 over time, as shown in Figure 4.8. Additionally, the vertical motion of the bottom of the well-dock is plotted, indicating an average depth of 2.65 m. Upon examining the results, the following observations are noticeable:

- After the second downward motion of the well-dock bottom (10.0 s < t < 13.0 s) waves start to roll into the dock by passing the wave gauge at St.0. This observation indicates that waves are only entering when location St.0 is at its maximum depth (maximal downwards motion amplitude). This is because at that point, the largest relative difference in free surface level is achieved.
- The period of the wave cycle is approximately 11.0 s, so there is a small decrease (4.4%) in period when compared to the coupled heave and pitch motion period of the LPD. This can be explained by the fact that in shallower water the wavelength will decrease, so decreasing the wave period.
- Three crests, labeled A, B, and C, are observed to break away from the long-period wave with an increased velocity. This phenomenon is caused by the interaction between the free surface motions and the shallower depth within the dock, caused by its limited water depth. This non-linear wave interaction can create secondary crests by transferring energy from the primary wave crest to secondary modes.
- When the main wave disintegrates into multiple crests (or modes), each mode can have a different speed due to the combined effects of non-linearity and dispersion. In traditional non-linear shallow water theories, the phase speed of the primary wave is given by [21][12]:

$$c = \sqrt{g(h+\eta)} \tag{4.1}$$

  As seen, the phase speed (c) depends on the local water depth h and the surface elevation ($\eta$). Under the crest, the total water depth is greater than under the troughs, causing the crest to propagate faster than the trough. As a result, the crest catches up with the trough, which can ultimately lead to wave breaking. In our case, this increased velocity in combination with the long wave length will result in the break away of the separate crests.

- The difference can also be explained by the fact that the waves are non-linear, so the first order wave does not propagate according to the linear dispersion relation anymore. Consequently, as the wave steepens the non-linear phase speed increases compared to the linear phase speed. Therefore, non-linear waves travel faster than linear waves [21].
- After approximately 10.0 m the wave group travels as a hole with the same velocity. This can be explained by the fact that in shallow water, the phase speed of non-linear waves is influenced by wave curvature. The curvature of the wave front leads to acceleration [27]. However, it is possible for the curvature $\frac{d^2\eta}{dx^2}$ to counteract the non-linear effect $\frac{h^2}{3\eta}$. Under certain conditions, these opposing effects can cancel each other out, resulting in a stable wave form [21].

$$c = \sqrt{g \cdot h \left(1 + \frac{3\eta}{2h} + \frac{h^2}{3\eta} \cdot \frac{d^2\eta}{dx^2}\right)} \tag{4.2}$$

### 4.1.3. Root mean square analysis

The wave height is calculated for each numerical WG positioned inside the well-dock. This is done by calculating the RMS, also known as the standard deviation [26] of the steady state signal in time domain. In total, five wave period were used. The results are shown in Figure 4.9.

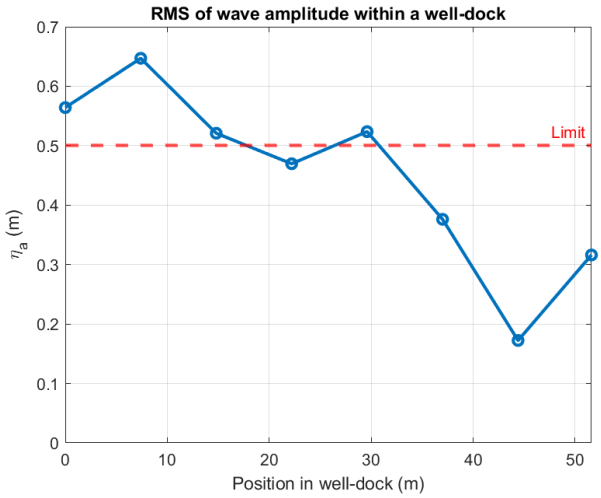


**Figure 4.9:** RMS of free surface elevation ($\eta$) for different locations within well-dock (St.0 = 0.0 m on the x-axis)

From the graph in Figure 4.9, the following conclusions can be made:

- The highest wave heights can be observed near the entrance of the well-dock, within the area St.0 < x < 10.0 m. This is in line with the findings presented in the papers from Yoon et al. [59], Cartwrith et al. [7], Hopman et al. [22], and Bass et al. [3]. This is likely due to the constructive interference of reflected waves from the beach ramp. Additionally, waves are generated in this area due to the largest relative difference in free surface levels.
- After 30.0 m within the well-dock, there is a significant drop in wave elevation, which can also be observed in the time-space domain simulations. As shown in Figures 4.6 and 4.9, incoming waves within this area are breaking due to a combination of shoaling and constructive interference.
- Near the beach ramp, a drop in wave height is observed as a result of breaking waves. This research assumes that there is a high probability of splashes of water against the aft of the LCU, due to slamming or white-capping from these broken waves.
- An increased wave height can be observed near the beach ramp due to the run-up effect near the slope of the ramp.
- Considering the maximum draft of the LCU of 1.4 m and a safety region of 0.25 m, the wave elevation must not exceed 0.5 m. From Figure 4.9, it is observed that this condition is not met within the area 0.0 m < x < 20.0 m.

## 4.2. Approximating the Free Surface Elevations Within Well-Dock

In this section the primary objective is to translate the measured surface elevation at St.0 into a superposition of regular wave components. To achieve this goal, the following steps are taken.

1. Measuring the free surface elevation in time domain at location St.0.
2. Choosing a specific time range where the entire cycle of wave elevation is observed, without interference with reflected waves originating from the beach ramp.
3. Transforming the measured surface elevation into frequency domain using Fast Fourier Transformation (FFT).
4. Analyzing the selected wave sample to determine its properties, including period, wave height, crests, troughs and other characteristics.

### 4.2.1. Time and Frequency Domain Analysis

Steps 1 and 2 presented above have been detailed in Figure 4.8, where all significant properties are presented. Given the scope of this thesis, it is critical to exclude the interference of reflected waves from the beach ramp. So, the first wave occurring after the completion of one motion cycle of the LPD is selected as the input wave within the dock. This wave is then used in the FFT analysis (see Figure 4.10).

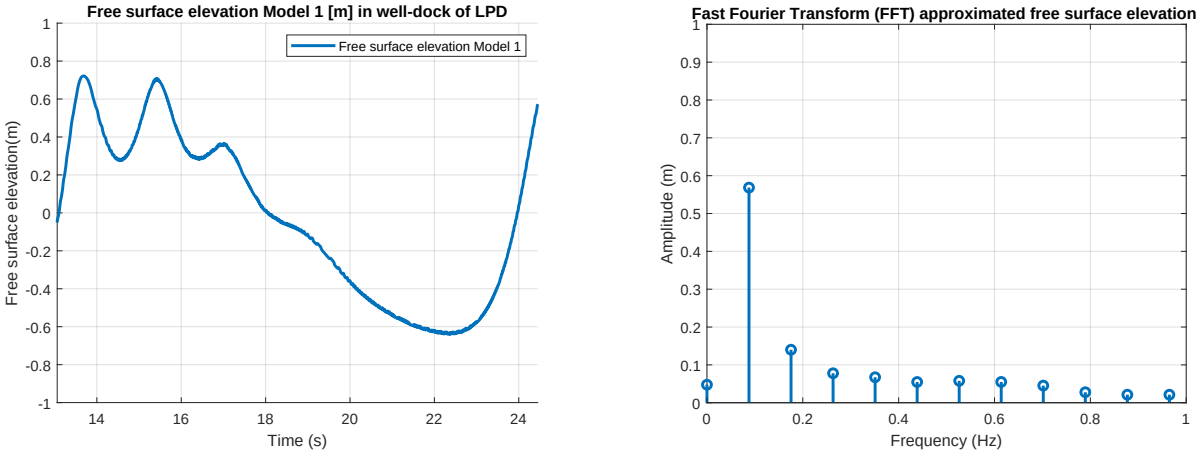


**Figure 4.10:** Free surface elevations in well-dock at St.0 within specific time window (left: time domain and right: frequency domain)

From these graphs in Figure 4.10 two conclusions can be drawn. Firstly, the primary wave component measures a maximum amplitude of 0.57 m. Secondly, the period is slightly lower (t = 10.9 s) in comparison with the period of the motion of the well-dock (t = 11.4 s). This reduction is due to the shallow water condition within the dock. The decrease in depth leads to a decrease in wavelength, resulting in an increase in wave frequency and, therefore, a decrease in wave period.

### 4.2.2. Non-linearity Analysis

It is crucial to determine the wave regime before using the appropriate wave theory to analyse free surface elevations. Figure 2.1 will assists in identifying the wave regime and the Ursell number will assesses the degree of non-linearity [13]. When calculating the Ursell number with use of Equation 4.3, it's important to note that the water depth (d) depends on the location within the well-dock. In the upcoming calculation, an average water depth of 2.65 m and a maximum wave height H of 1.14 m is chosen. The corresponding wave period T is 10.9 s.

$$N_{Ursell} = \frac{\frac{H}{g \cdot T^2}}{\left(\frac{d}{g \cdot T^2}\right)^2} \tag{4.3}$$

By assuming a fixed water depth, the calculated Ursell number is an approximation. The actual number would even be higher for two reasons. Firstly, as shown in Figure 4.9, the wave height $H$ increases along the length (0.0 < x < 10.0 m) of the well-dock. Secondly, the water depth $d$ decreases due to the sloped bottom.

Based on Figure 2.1 and the calculation of the Ursell-number, several conclusions can be made. To start, the wave regime is described by cnoidal wave theory and lies on the boundary of solitary wave theory. Second, the high Ursell number of 200.0 (-) indicates non-linearity. This causes the troughs to lengthen and flatten, while the crests become sharper. This behavior is consistent with the observed results presented in space and time domain.

To calculate the phase speed, surface elevations were measured between two wave gauges, positioned 5.0 meters apart ($\Delta x$) over a time difference $\Delta t$. The equation used is presented below:

$$c = \frac{\Delta x}{\Delta t} \tag{4.4}$$

The phase speed can also be calculated under the assumption of linear conditions, by using Equation 4.5. Where $c$ is the phase speed, $g$ the gravitational constant and $d$ the water depth. In the end, the differences in $c$ indicate the effects of non-linearity.

$$c = \sqrt{g \cdot d} \tag{4.5}$$

The difference can be determined by calculating $c$ using Equations 4.4 and 4.5. An increase of 7.4% in phase velocity is present due to the effect of non-linear amplitude dispersion. Hence, this value is even larger due to the constant water depth. Throughout the simulation, changes in the sloped bottom and the dock's movement continuously affect $d$ as the wave progresses.

Non-linear amplitude dispersion is evident in the individual phase speeds of the crests (A, B, C), which respectively are 5.3 m/s, 4.7 m/s, and 3.9 m/s. This difference is explained by the direct relationship between wave amplitude and speed in many solitary wave types: where higher amplitude waves travel faster than lower amplitude ones [21]. Moreover, this difference diminishes over distance due to the balance between dispersive and non-linear effects, as described in Equation 4.2.

### 4.2.3. Computing the Approximated Free Surface Elevation

In this paragraph, the free surface elevation measured in a moving well-dock is converted into an approximated input wave for a stationary non-moving well-dock. To approximate the wave components shown in Figure 4.10, FFT results from the free surface elevations in a moving dock will be used to extract amplitudes, frequencies, and phase-angles. These data are then implemented in ComFLOW using the linear irregular waves plug-in function.

The super-position of regular linear waves, which approaches the measured elevation in a moving dock, is then introduced to a non-moving well-dock with a fixed water depth of 2.65 m. Additionally, a zone of 20.0 meters is introduced in front of position St. 0. This allows the wave to fully develop and interact with the bottom. Furthermore, from left to right numerical wave gauges are placed with a distance of 1.0 m between them. In the end, each position is plotted to find the most aligning free surface elevation. The result of the best alignment can be seen in Figure 4.11. Note that the FFT analysis is conducted over five measured wave periods.

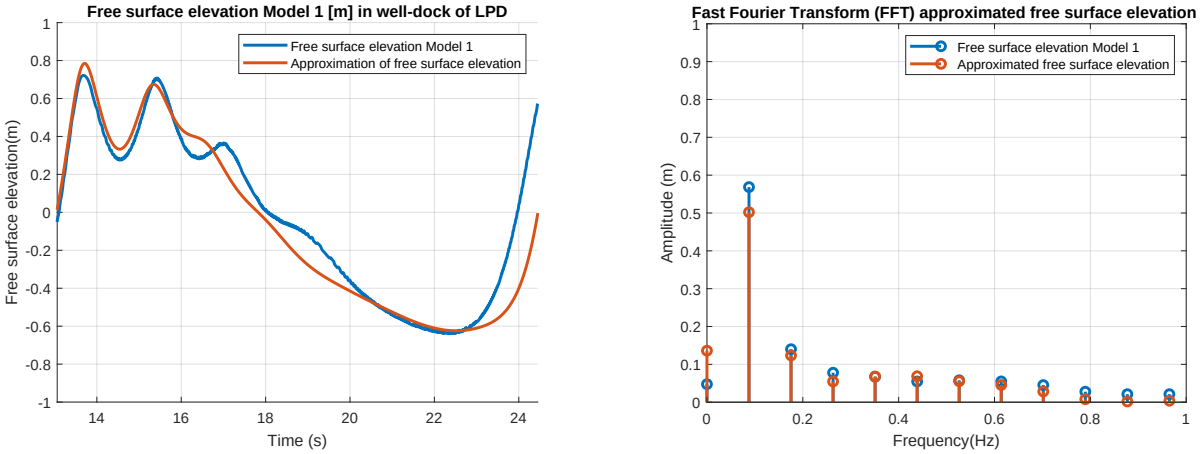


**Figure 4.11:** Approximation of free surface elevation in the well-dock at St.0 within a specific time window (left: time domain and right: frequency domain)

The period of the approximated surface elevation is 0.48 s higher in comparison with the measured elevation in Model 1. Thus being the same as the period of the oscillating motion of the LPD. Furthermore, it is evident that the wave is breaking apart into three separate waves, each decreasing in height. In the approximated wave, this phenomenon is partly present when looking at the third crest. The absence of well-dock motions, resulting in a fixed water depth, might lead to less pronounced declines in the three separate waves entering the dock.

In frequency domain, the dominant amplitude differs from the results obtained in Model 1, showing that the approximated wave input is underestimated. However, when calculating the wave energy, a negligible difference in wave energy content is revealed. Specifically, the energy from Model 1 is equal to $1.947 \times 10^3\ J/m^2$ and the approximated wave contains $1.915 \times 10^3\ J/m^2$. This indicates that the static Model 2, with approximated wave input, can accurately represent the wave energy and properties with an error of 1.6%.

# 5

# Conclusions and Recommendations

## 5.1. Conclusions

To answer the main research question, several sub-objectives must be addressed first. This led to four sub-research questions that guide the direction of this thesis. The first two sub-research questions answered in Part I were:

1. ***"What is the modelling approach for simulating wave (free surface) motions in a flooded well-dock of an LPD in a specific sea state?"***
2. ***"What are the properties of free surface motions in a flooded well-dock of an LPD in a specific sea state?"***

When examining existing literature, unidirectional irregular head waves appear to be the most realistic option for the LPD user profile. The LPD can be modelled with different degrees of freedom, but it is realistic to assume free movement in the heave and pitch directions, without forward speed. Additionally, the presence of a sloped beach ramp at the well-dock's end is crucial to determine specific locations of large wave responses due to constructive interference.

Insights from existing papers guided the development of a numerical model (Model 1). Free surface motions within the dock are generated by a mechanism where a drop in the free surface leads to a difference between the outer and inner parts of the well-dock. This water level difference causes a wave to roll into the dock from the higher elevation towards the lower level, propagating towards the beach ramp.

The wave period is approximately the same as the period of the LPD oscillating in a specific sea state. After the wave is generated, multiple smaller crests break away from the long-period wave crest due to interaction with the well-dock bottom. By examining the results, the wave regime is close to that described by cnoidal wave theory and on the boundary of solitary wave theory. The high Ursell number indicates significant non-linearity, causing the troughs to lengthen and flatten while the crests become sharper.

The root mean square of the surface elevations shows that the highest values can be observed near the entrance of the well-dock, within the area St.0 < x < 10.0 m. This is in line with existing papers from Yoon et al. [59], Cartwrith et al. [7], Hopman et al. [22] and Bass et al. [3].

## 5.2. Recommendations

During the simulation and setup of the computational domain, several simplifications and assumptions were made. The most important elements are discussed below.

The CFD model focuses solely on the LPD's motion, neglecting oscillations of the free surface of the ocean. During low-frequency waves, where the LPD moves in sync with the waves, the height difference between the dock's interior and exterior is negligible. However, in short period waves, this could effect the relative difference between the outer and inner water level. Assuming no oscillations of the free surface affect the relative height difference, which may influence the height of the generated wave. Furthermore, ignoring sea waves neglects the effects of wave diffraction and radiation near the stern. These additional waves may interfere with the already generated sloshing. To conclude, future research should use an LPD geometry oscillating in steady-state sea conditions. This approach will provide more accuracy in presenting the phase / frequency difference between surface waves and LPD motions, and will account for the presence of diffraction and radiation waves generated by the LPD's hull.

Large numerical domains prevent detailed simulations of free surface elevation from capturing all wave breaking events. Additionally, a turbulence model is not used in the numerical simulations. These two modeling choices could result in less wave energy dissipation due to fewer non-linear effects, thereby decreasing the probability of wave energy distribution or earlier wave breaking. Future research should incorporate a turbulence model for shallow water conditions and use a smaller grid around the free surface to capture all breaking waves. This will yield more wave energy dissipation mechanisms.

This research only looked at the effects of 2D head waves, which resulted in longitudinal sloshing and ignored waves from other directions (e.g. bow quartering). Thus, assuming no reflections from the dock's inner walls or multi-directional waves within the dock exist. However, such events may result in additional interference and wave-breaking at specific locations within the well-dock. Further research should focus on 3D modelling to incorporate waves from multiple directions, which can help in determining locations of interference and additional wave breaking, thereby dissipating energy.

# Part II

# Concept Design(s) with System Engineering

# 6

# Methodology

System engineering and typical product design techniques guide designers through initial design phases [36]. These include defining a mission, identifying stakeholders and their requirements, outlining functional requirements and establishing goals. SE emphasises taking the entire life cycle of a system and breaking it down into manageable sub-functions. During this research the SE-process presented by Pahl [36] is applied.

## 6.1. Task clarification

It is necessary to clearly define the given task that the Wave Attenuation Solution (WAS) must fulfill. The primary aim of a clarification process is to gather all relevant information regarding the system requirements and relevant limitations. As a result, this process yields a comprehensive list of requirements. To accomplish the requirement list, prepared questions are addressed in an interview with engineers from Commando Materieel & IT (COMMIT). These employees are responsible for the current LPD vessels and their replacement programs. Besides the interviews, existing naval reports, doctrines and procedures related to the LPD vessels were consulted for additional insights. In the end, the results are summarized and processed into a requirements list.

### 6.1.1. Objective(s)

As outlined in the problem statement (see Section 1.1), extreme oscillations of the free surface pose a significant challenge for the safe embarkation and disembarkation of landing vessels in a well-dock. It is crucial to reduce the free surface elevation to prevent the aft of the LCU from hitting the bottom of the well-dock with excessive force Therefore, the primary objective outlined by COMMIT is to reduce the amount of wave energy entering the well-dock to ensure that the amplitude of the free surface motions does not exceed 0.5 m within the region of St. $0 < x < 15.0$ m. By meeting this objective, the operability in higher sea states will be improved due to avoiding:

1. Landing crafts from hitting the well-dock floor;
2. High splashes of water against the aft oft the LCU due to slamming or white-capping from waves within the dock;
3. Run-up of water on the vehicle deck.

After completing Model 1 and performing RMS calculations, Figure 4.9 shows that 0 < x < 15.0 m has the highest free surface elevations, resulting in decreased operability. A sketch with this location presented in Figure 6.1, where the area of interest is delineated by a red square box. To aid visualization, a wave with a wavelength of approximately 50.0 m is depicted, matching the length of the well-dock.

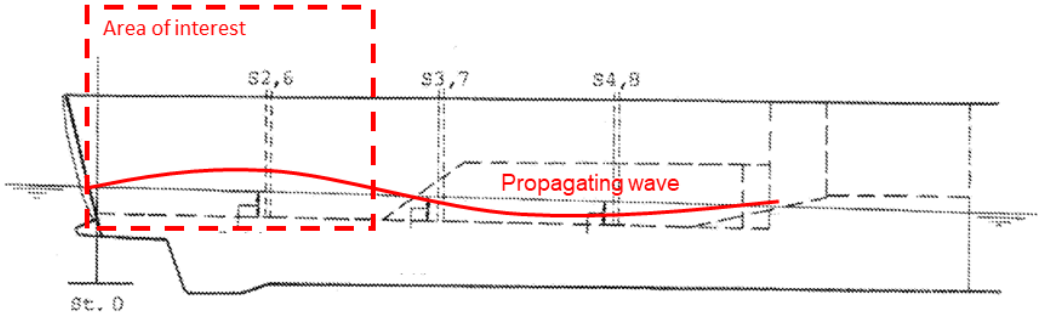


**Figure 6.1:** Objective area within a well-dock [22]

### 6.1.2. Properties and requirements

In addition to the primary objective outlined in Section 1.2.1, COMMIT has specified certain sub-requirements and properties for the proposed solutions. These are as follows:

1. The solution should be easily retrofitted without requiring adjustments to the internal structure of the well-dock.
2. The solution must operate as a passive system, without the need for additional energy input.
3. Minimal maintenance should be required.
4. Design aspects of the solution should not pose risks of entanglement or damage due to impacts on propellers or pump jets.
5. The solution should be resilient to minor impacts from the LCU, both when submerged and when the water depth is reduced during transit.
6. The solution must not obstruct the landing vessels pathway in any way.
7. The solution should be capable of supporting the weight of the LCU when the well-dock floor is drained and the LCU is resting on the well-dock floor.

## 6.2. Concept Design(s)

To create the initial concept designs, it's crucial to understand the core problem first. Therefor it is necessary to analyse the interview results and the relevant documents such as LPD doctrines. These findings are used to develop a working structure to guide the selection of the best concept designs.

### 6.2.1. Functional Breakdown Structure

In this paragraph, the primary objective is to translate the requirements into a functional structure that represents the solution. This process is carried out for each phase in the life cycle of the solution. The main phases are depicted in Figure 6.2.

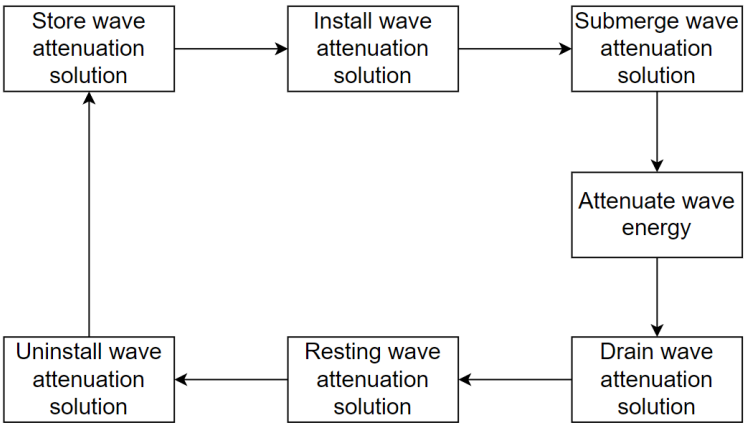


**Figure 6.2:** Life cycle of the solution

The process begins with storing the solution on the LPD. Once the operation begins, the next step is to install the solution at a specific location within the well-dock using the LPD's available manpower and machinery. After installation, the solution must not obstruct the areas where landing vessels are positioned. Once these vessels are loaded, the LPD sails to its designated operation area. The same steps as described in Paragraph 1.1.3 are then undertaken, resulting in the flooding of the entire dock to the water depth specified in Figure 3.3.

When the LPD is in operation, the solution must attenuate the maximum amount of wave energy, either by reflection or dissipation. This means it must withstand the (drift) forces and moments acting on it. In the end of the operation, the well-dock is drained and the landing vessels (i.e. LCU) come to rest on the well-dock bottom. This means that the vessels can impact and rest on the solution. Upon returning to the harbor, the solution can be detached and stored.

### 6.2.2. Developing Working Structure

After completion of the sub-function structure by looking at the life-cycle, working principles need to be found for the various (sub-) functions. Eventually, these principles must be combined into a working structure. It is crucial to ensure that a working principle aligns with the required physical effect for achieving a specific function, along with its geometric and material characteristics [36]. In Table 6.1, the functional structure is presented, wherein each row presents the potential working principles (options 1 to 3) corresponding to each sub-function (A to F).

| | **Working principle** | **Option 1** | **Option 2** | **Option 3** |
|---|---|---|---|---|
| A | Reflect waves | Large surface area | Geometrical slope | Surface roughness |
| B | Radiate waves | Tuning to incident $T_{wave}$ | Optimized geometry | Optimized geometry |
| C | Damp wave energy | Mechanical damping | Drag forces and turbulence | Elastic deformation |
| D | Free to move | Bottom hinged (pitch) | Floating (heave and pitch) | Top hinged (pitch) |
| E | Modular (sea state) | Modular segments | Internal champers | Multiple systems |
| F | Impact proof (e.g. LCU) | Soft polymer | Rigid (high Young's modulus) | Decreased length |

**Table 6.1:** Working structure for WAS

When selecting the optimal option, it is important to consider both the requirements from COMMIT and the limitations of the CFD software. The following paragraphs will discuss the advantages and disadvantages of the different options.

Sub-function A
One sub-function is to reflect waves, which can be accomplished by using a perpendicular surface area. One example is a surface piercing vertical wall in waves, which can reflect 100% of the energy. However, considering the requirements of COMMIT, the solution must not obstruct the pathway of incoming vessels. Meaning it must be submerged with a minimal depth of 1.4 m. This should not be an issue because the velocity profile in shallow water, such as within the well-dock, is almost linear, as depicted in Figure 2.2. So, the shallow water conditions be exploited by using the advantage of the amplification of horizontal water particle motion [19]. Another reflection method involves optimising shapes and slopes at the well-docks bottom. Due to the restricted water depth of the dock as seen in Figure 3.3, it is assumed that this approach would not yield significant results in terms of reflection.

Sub-function B
Radiation damping occurs when an object oscillates in a fluid, redistributing wave energy and potentially causing destructive interference. This process requires no additional mechanisms and therefore improves maintainability. The amount of wave radiation depends on the geometry of the object and the wave frequency at which this geometry oscillates. This means that the solution can be designed to maximize radiation damping at specific wave frequencies.

Sub-function C
Wave energy dissipation can be achieved through wave breaking, radiation damping and mechanical damping. With mechanical damping the amount of damping can be adjusted to dissipate the maximum amount of wave energy. Besides this mechanical damping, energy dissipation can also be caused by drag, turbulence, or internal elastic deformation. For drag and turbulence, energy is lost due to the separation of flow which causes vortices. This loss mechanism is generally considered to be proportional to the frontal area of the body and is in phase with the flap's velocity [19]. However, these latter mechanisms have limitations when using ComFLOW, as the current models do not simulate these events accurately [51].

Sub-function D
During amphibious operations, the well-dock is flooded and the solution must come into action. This means the solution must have some DOF. This DOF is also needed when the dock is flooded and vessels are entering or leaving the dock. Ultimately, a minimum of 1-DOF ensures that vessels can move the solution without damaging their hulls.

Several methods can be applied to ensure DOF. Firstly, a bottom hinge can be used to allow oscillation in the pitch direction. Conversely, top hinged could be used, but it might obstruct the storage area when the dock is drained. Lastly, the solution can be moored to the bottom, allowing it to float at a certain depth and oscillate in both pitch and heave directions. However, the presence of mooring lines could entangle with the propulsion system of the landing vessels.

In conclusion, a submerged bottom-hinged flap is ideal to meet COMMIT's requirements, ensuring maximum surface area and preventing entanglement or collisions. According to Henry et al. [20], selecting this solution requires to position the hinge point as close to the bottom as feasible to maximize wave torque for effective energy dissipation.

### Sub-function E

LPDs encounter both long and short period waves from wind- and swell waves. As a result of this variation in wave periods, the solution needs to attenuate wave energy across a broad range of wave periods. This condition also impacts the sub-function of wave radiation, which varies depending on the wave period.

A modular design that allows for shape adjustment to modify hydrodynamic properties and enhance wave attenuation, can effectively accommodate different wave periods. Another method to accommodate different wave periods is the introduction of internal chambers that can be flooded with seawater. This approach allows for the adjustment of inertia and restoring moment (spring) properties, to influence the dynamics. Lastly, a system of systems (e.g., arrays) can be used to optimise wave attenuation.

When selecting a bottom-hinged solution with maximum surface area, it is logical to choose the option of internal chambers. By flooding these cavities with water, the CoG or mass can be adjusted accordingly.

### Sub-function F

When the solution is operational, the LCU is likely to hit the bottom hinged solution, both in a flooded and non-flooded well-dock. Several measures can be implemented to reduce this risk. First, the solution could be built of a flexible (polymer) material that absorbs impacts. An alternative is to create a stiff body that can be easily pushed away without any damage. Lastly, a shorter flap can be applied, which in turn diminishes radiation damping and reflection.

### Conclusions

The solution should feature a bottom-hinged flap with a large surface area, which is limited to a depth of 1.4 m. An increased surface area ensures maximum wave reflection, which, along with (radiation) damping, optimises wave attenuation performance. The damping effect can be further enhanced by introducing mechanical damping. Because of ComFLOW's limitations, additional energy dissipation due to turbulence and drag is not taken into account.

### 6.2.3. Developing Concepts

The next step in the SE-process is developing concepts using the selected function- and working principles structure. As depicted in Figures 6.3 to 6.6, various concept designs can be considered to fulfill a specific function stemming from a requirement or restriction. In the end, design number 15 is chosen as the best concept design for further research in Part III.

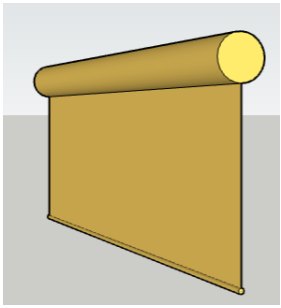

| Feature | Design 1 |
|---|---|
| Material | Steel |
| Positioning | Floater with bottom hinge |
| Modular (adaptivity) | No |
| Wave attenuation | ▪ Radiation<br>▪ Reflection |

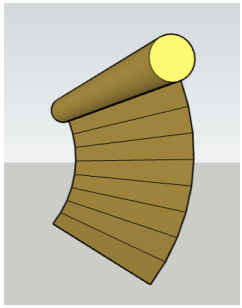

| Feature | Design 2 |
|---|---|
| Material | Steel |
| Positioning | Floater with bottom hinge |
| Modular (adaptivity) | No |
| Wave attenuation | ▪ Radiation<br>▪ Reflection<br>▪ Drag |

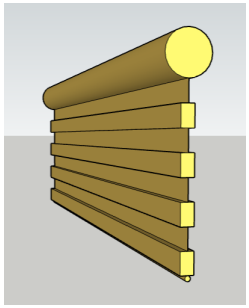

| Feature | Design 3 |
|---|---|
| Material | Steel |
| Positioning | Floater with bottom hinge |
| Modular (adaptivity) | No |
| Wave attenuation | ▪ Radiation<br>▪ Reflection<br>▪ Drag |

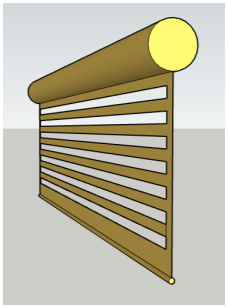

| Feature | Design 4 |
|---|---|
| Material | Steel |
| Positioning | Floater with bottom hinge |
| Modular (adaptivity) | No |
| Wave attenuation | ▪ Radiation<br>▪ Reflection<br>▪ Drag & turbulence |

**Figure 6.3:** Concept designs WAS 1 to 4

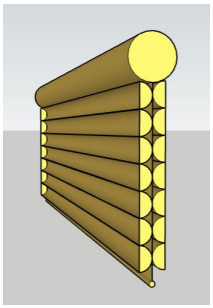

| Feature | Design 5 |
|---|---|
| Material | Steel |
| Positioning | Floater with bottom hinge |
| Modular (adaptivity) | No |
| Wave attenuation | ▪ Radiation<br>▪ Reflection<br>▪ Drag |

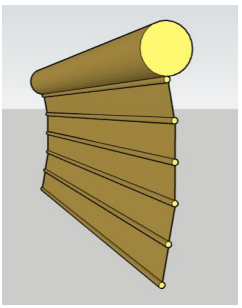

| Feature | Design 6 |
|---|---|
| Material | Steel |
| Positioning | Floater with bottom hinge |
| Modular (adaptivity) | No |
| Wave attenuation | ▪ Radiation<br>▪ Reflection<br>▪ Internal bending<br>▪ Drag |

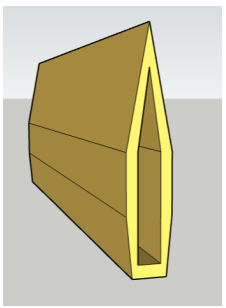

| Feature | Design 7 |
|---|---|
| Material | Polymer |
| Positioning | Internal chamber with bottom hinge |
| Modular (adaptivity) | No |
| Wave attenuation | ▪ Radiation<br>▪ Reflection<br>▪ Turbulence<br>▪ Internal bending |

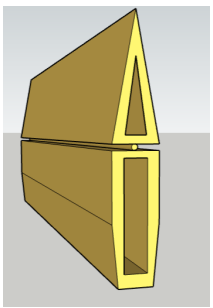

| Feature | Design 8 |
|---|---|
| Material | Polymer |
| Positioning | Internal chamber with bottom hinge |
| Modular (adaptivity) | Filling chambers with water |
| Wave attenuation | ▪ Radiation<br>▪ Reflection<br>▪ Turbulence<br>▪ Internal bending |

**Figure 6.4:** Concept designs WAS 5 to 8

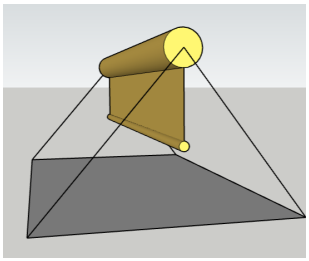

| Feature | Design 9 |
|---|---|
| **Material** | Visco-elastic |
| **Positioning** | Floater and mooring system (2x) |
| **Modular (adaptivity)** | ▪ Adjust inertia properties<br>▪ Length flap |
| **Wave attenuation** | ▪ Reflection<br>▪ Radiation damping. |

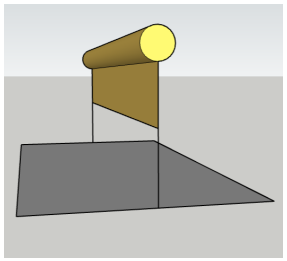

| Feature | Design 10 |
|---|---|
| **Material** | Polymer |
| **Positioning** | Floater and mooring system (1x) |
| **Modular (adaptivity)** | Change length flap and mooring system |
| **Wave attenuation** | ▪ Reflection<br>▪ Radiation damping |

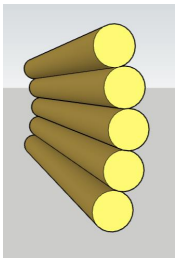

| Feature | Design 11 |
|---|---|
| **Material** | Polymer |
| **Positioning** | Floater with hinge or mooring lines |
| **Modular (adaptivity)** | Adapt tubes for properties |
| **Wave attenuation** | ▪ Internal bending<br>▪ Reflection<br>▪ Mechanical damping<br>▪ Radiation damping |

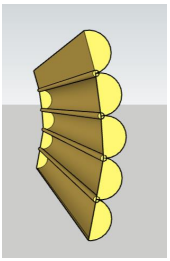

| Feature | Design 12 |
|---|---|
| **Material** | Steel |
| **Positioning** | Floater with hinge |
| **Modular (adaptivity)** | None |
| **Wave attenuation** | ▪ Internal bending<br>▪ Reflection<br>▪ Drag<br>▪ Radiation damping |

**Figure 6.5:** Concept designs WAS 9 to 12

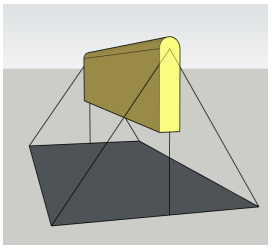

| Feature | Design 13 |
|---|---|
| **Material** | Visco-elastic |
| **Positioning** | Floater with mooring |
| **Modular (adaptivity)** | Adjust mooring system |
| **Wave attenuation** | ▪ Reflection<br>▪ Radiation |

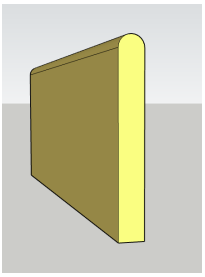

| Feature | Design 14 |
|---|---|
| **Material** | Hollow elastic flap |
| **Positioning** | Floater with top/bottom hinge |
| **Modular (adaptivity)** | None |
| **Wave attenuation** | ▪ Internal bending (energy conversion)<br>▪ Reflection<br>▪ Radiation |

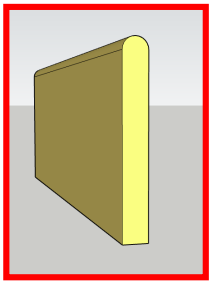

| Feature | Design 15 |
|---|---|
| **Material** | Rigid body |
| **Positioning** | Floater with top/bottom hinge |
| **Modular (adaptivity)** | None |
| **Wave attenuation** | ▪ Reflection<br>▪ Radiation |

**Figure 6.6:** Concept designs WAS 13 to 15

## 6.3. Design Optimisation with Physics

Based on the concept design phase conducted in Section 6.2, a submerged bottom hinged pitching flap has been selected as the preferred solution for further optimisation. The hypothesis is that implementing this wave attenuation solution will reduce free surface elevations behind the flap, minimizing the wave energy entering the dock. To maximize this attenuation effect, the concept solution undergoes optimisation by analysing hydrodynamic response.

### 6.3.1. Determining wave energy attenuation

Measuring the performance of the WAS involves measuring the free surface elevation ($\eta$) both in front of and behind the WAS. By utilizing the group velocity $c_g$ of the wave, the difference in power flux $P$ can be obtained. It is important to note that the group velocity depends on the water depth and wave number, which can vary in shallow water, intermediate, and deep water conditions. Ultimately, the primary goal during design optimisation is to maximize this power flux difference by means of reflection or dissipation (e.g. wave breaking or damping).

#### General information

The high-level SE-analysis conducted in part II underscores that a bottom-hinged flap aligns most effectively with the requirements and constraints outlined by COMMIT and ComFLOW. An illustrative example of such a submerged flap is depicted in the Figure 6.7:

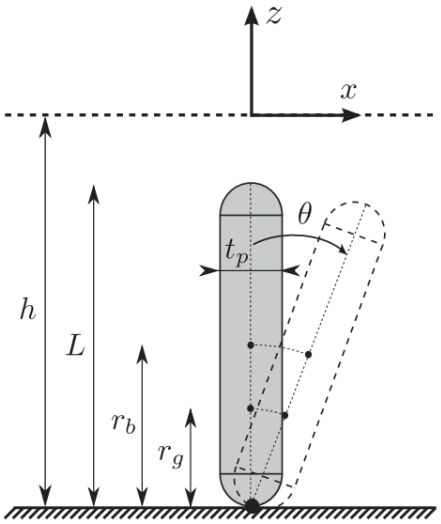


**Figure 6.7:** Side view of a bottom-hinged flap and it's dimensions [17]

The meaning of the parameters are listed below:

$h =$ water depth (m)

$L =$ height of the flap (m)

$r_b = L/2 =$ distance from the hinge to the centre of buoyancy (m)

$r_g =$ distance from the hinge to the centre of gravity (m)

$t_p =$ flap thickness (m)

$\theta =$ rotation angle of the flap (°)

When an object is submerged in water and excited by waves, it experiences forces and moments (Froude - Krylov) based on the submerged volume ($\nabla$) as well as the incoming wave's height ($H$) and period ($T$). Consequently, these wave-induced forces and moments cause the submerged object to oscillate. In addition, these oscillations generate radiation waves at the oscillation frequency of the moving object. The amplitude of these emitted waves depends on the object's dimensions and the magnitude of its pitching motion [19]. These radiated waves extract energy from the system. The next paragraph will provide further information about this phenomenon.

#### Wave energy attenuation

Wave energy attenuation is best understood as a process of wave interference. To effectively absorb a wave, the WAS must produce "counter radiation-waves" to interact with the incident waves. When this interaction results in destructive interference (out-of-phase) — meaning it diminishes the incoming wave — the WAS attenuates wave energy [19][38].

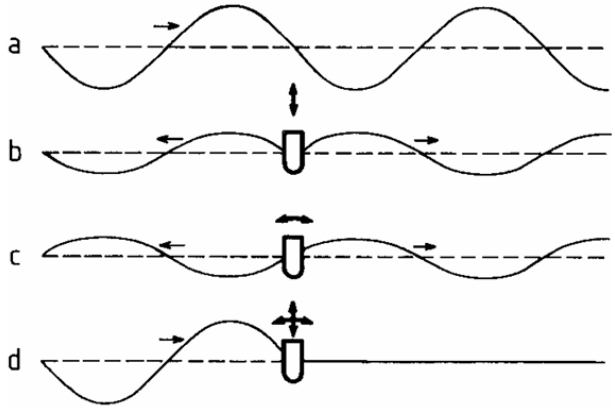


**Figure 6.8:** 2D wave attenuation theory [14]

Falnes [14] stated with use of Figure 6.8 that absorbing waves requires the generation of waves. When looking at the Image (a), this represents an undisturbed incident wave. Image (b) shows symmetric wave generation (on otherwise calm water). Image (c) depicts anti-symmetric wave generation. Lastly, image (d) represents the superposition of all waves mentioned above, and absorbing all of the incident wave energy. In conclusion, the radiated wave interferes destructively with the incident wave, resulting in a combined wave that propagates beyond the wave absorber with less power than the incident wave [14].

### 6.3.2. Hydrodynamic response

To optimise the design of the WAS, such that the wave attenuation is maximized, the Equation of Motion (EoM) of a pitching flap presented by Senol et al. [45] must be further examination and understood.

$$M_r(t) + M_h(t) + M_m(t) = M_e(t) \tag{6.1}$$

Note that the radiation moment $M_r$ is equal to:

$$M_r(t) = [I_a + A(\infty)] \cdot \ddot{\theta}(t) + B(\omega) \cdot \dot{\theta}(t) \tag{6.2}$$

and the hydrostatic restoring moment $M_h$ is:

$$M_h(t) = C \cdot \theta(t) \tag{6.3}$$

In a later section of this report, an in-depth analysis investigates the implications of integrating additional mechanical damping ($B_m$) within the hinge. For this reason, the mechanical damping term is also integrated into the EoM.

$$M_m = B_m \cdot \dot{\theta}(t) + C_m \cdot \theta(t) \tag{6.4}$$

Finally, the wave excitation moment $M_e$ due to a single regular wave component is presented by:

$$M_e = A_w \cdot \Gamma \cdot sin(\omega t + \epsilon_{M_e}) \tag{6.5}$$

Where $A_w$ is the incoming wave amplitude and $\Gamma$ the frequency dependent excitation moment coefficient.

After substituting all described elements, the total equation of motion can be stated:

$$[I_m + A(\infty)] \cdot \ddot{\theta}(t) + [B(\omega) + B_m] \cdot \dot{\theta}(t) + [C + C_m] \cdot \theta(t) = A_W \cdot \Gamma \cdot sin\left(\omega t + \epsilon_{M_e}\right) \tag{6.6}$$

In Equation 6.6 $I_m$ represents the mass moment of inertia in the pitch direction, measured in $kg \cdot m^2$. The wave frequency, denoted as $\omega$ and is measured in $rad/s$. The added mass moment of inertia at infinite frequency, $A(\infty)$ , is measured in $kg \cdot m^2$. This parameter, described by Cummins [8], accounts for the added mass moment of inertia effect. The damping coefficient B($\omega$), represents the radiation damping due to generated waves and is measured in Nm / (rad/s). This coefficient is essential for quantifying the energy dissipation caused by wave radiation. From the EoM it is assumed that this term is a linear effect and in phase with the velocity. Finally, C is the hydrostatic stiffness or restoring moment, proportional to the water displacement of the submerged body, measured in N/m. This parameter determines the restoring moment that acts on the Centre of Buoyancy (CoB) to return the system to its equilibrium position.

It must be noted that the excitation moment ($A_w\Gamma$) on the right-side of the equation is in-phase with the pitching motions ($\theta$) and is related to the inertia term ($I_m$) and stiffness coefficient ($C$), while the out-of phase components are related to the damping terms [26]. Furthermore, the presented EoM does not account for non-linear (quadratic) damping caused by viscous effects (e.g. drag and vortex shedding) as described by Asmuth et al. [2].

### 6.3.3. Natural period

Now the equation of motion for the pitching flap is known, the undamped natural period and angular frequency can be calculated. The hypothesis is that tuning a flap to the dominant incoming wave frequency maximizes pitching motion amplitudes and enhances radiation damping, leading to optimal wave attenuation performance [30]. To calculate the undamped natural period of the flap, terms are used from the equation of motion and the following Equation 6.8 given by Pecher & Kofoed [38]:

$$T_n = 2 \cdot \pi \cdot \sqrt{\frac{I_m + A(\infty)}{C + C_m}} \tag{6.7}$$

Because no mechanical springs are added, $C_m$ will be zero, so:

$$T_n = 2 \cdot \pi \cdot \sqrt{\frac{I_m + A(\infty)}{C}} \tag{6.8}$$

Radiation damping and additional mechanical damping have no effect on the flap's natural period (Equation 6.8). The only contributions come from the added mass moment of inertia, moment of inertia and the restoring moment. All three parameters depend on the flap's dimensions or mass distribution. This relationship is evident in the following equations:

The mass moment of inertia $I_m$ can be calculated with use of the parallel axis theorem, also stated by Gomes et al. [17]:

$$I_m = \left(\frac{\rho_{flap}}{\rho_{fluid}}\right) \cdot \rho_{fluid} \cdot t_f \cdot W \cdot L \left(\frac{1}{12} \cdot \left(L^2 + t_f^2\right) + r_g^2\right) \tag{6.9}$$

$$I_m = \alpha \cdot \rho_{fluid} \cdot t_f \cdot W \cdot L \left(\frac{1}{12} \cdot \left(L^2 + t_f^2\right) + r_g^2\right) \tag{6.10}$$

$$I_m = \frac{1}{12} \cdot m \cdot \left(L^2 + t_f^2\right) + m \cdot r_g^2 \tag{6.11}$$

Where, $\frac{\rho_{flap}}{\rho_{fluid}} = \alpha$ and W is the width of the flap into the y-direction. Hence, due to 2D-simulations W = 1.0 m in both calculations and ComFLOW-settings.

The hydrostatic restoring coefficient or restoring moment presented in Equation 6.8 is calculated using the equation below described by Gomes et al. [16]:

$$C = g \cdot t_f \cdot W \cdot L \left(\rho_w \cdot r_b - \rho_f \cdot r_g\right) \tag{6.12}$$

### 6.3.4. Damping

In this paragraph the damping principle of the flap will be looked into, which is used to optimise the WAS design. This by analyzing the EoM to identify key design parameters for maximizing free surface elevation reduction behind the WAS through damping.

To effectively attenuate wave energy, it requires the generation of out-of-phase radiated waves [19]. Examining Equation 6.6 it is found that the out-of-phase damping coefficient $B(\omega)$, which correlates with the pitching velocity $\dot{\theta}(t)$, plays a significant role in achieving this objective. Another option is to implement a mechanical damping mechanism within the hinge of the flap. Instead of relying on destructive interference, the surface elevation is reduced by extracting energy from the waves using torsional dampers inside the hinge.

By solving the general solution of the EoM, three possible outcomes exists: under-, critically- and over-damped [23][25]. These outcomes, also referred to as determinants, can be used to quantify the effectiveness of different damping regimes in attenuating wave energy.

1. $[B(\omega) + B_m]^2 - 4 \cdot [I_m + A(\infty)] \cdot [C + C_m] < 0$ (under-damped);
2. $[B(\omega) + B_m]^2 - 4 \cdot [I_m + A(\infty)] \cdot [C + C_m] = 0$ (critically damped);
3. $[B(\omega) + B_m]^2 - 4 \cdot [I_m + A(\infty)] \cdot [C + C_m] > 0$ (over-damped).

When plotting the three possibilities regarding damping, the following observation can be made. An under-damped system **(a)** will oscillate, with each successive oscillation decreasing in magnitude (sinusoidal decay) until it comes to rest. Conversely, a super critically damped system **(c)** is where the object is pushed (e.g. wave torque) out of the equilibrium and the object goes to the new equilibrium without vibrations. However, the bigger the damping ratio $\left(\zeta = \frac{B}{B_{crit}}\right)$, the slower the system moves to it's new equilibrium. At the boundary between these two scenarios lies the critically damped system **(b)**, which possesses just enough damping to completely suppress oscillations.

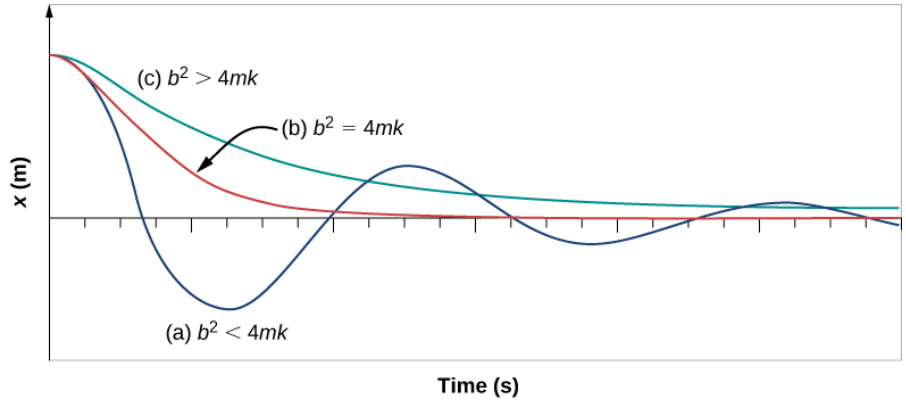


**Figure 6.9:** An example displacement of a harmonic oscillator for different amounts of damping, the restoring moment C is in the graph equal to k [42]

During the optimisation process, the damping coefficients in the EoM must be tuned to optimal conditions. To determine these optimal conditions, the damping coefficient must be investigated further. The initial hypothesis is twofold. First, it is assumed that the ideal condition is when the sum of coefficients (radiation and mechanical) equals the critical damping (see Equation 6.13).

$$B_{optimal} = B(\omega) + B_m = B_{crit} = 2\sqrt{C \cdot (I_m + A(\infty))} \tag{6.13}$$

Second, when the incident wave period matches the flap's natural period, the mechanical damping equals the radiation damping coefficient at this resonance period ($B(\omega_0)$ = $B_m$) [40]. In this way, the body is tuned to resonate with the highest motion amplitudes while dissipating the most wave energy. The equation for optimal damping becomes:

$$B_{optimal} = B(\omega_0) + B_m \tag{6.14}$$

where, $B_m$ = $B(\omega_0)$.

### 6.3.5. Hydrodynamic design optimisation

To achieve an optimal damped system various design parameters can be adjusted. Referring to Equation 6.13 and 6.14, $B_{optimal}$ can be achieved by adjusting the restoring coefficient (C), the moment of inertia ($I_m$) and mechanical damping ($B_m$). Firstly, altering the inertial term is achieved by changing flap dimensions such as thickness ($t_f$), width (W), mass (m) or position of the Centre of Gravity ($r_g$). Secondly, modifying the restoring term (C) involves adjusting the submerged volume ($\nabla$) or the vertical distance between the Center of Gravity and the hinge ($r_g$).

Considering the operational constraints of the LPD and the requirements outlined by COMMIT, it is impractical to adjust the flap's thickness. This because the flap must rest on the bottom of the drained well-dock without hindering the LCU's. For this reason, only adjustments in mass, and therefore, the mass ratio ($\alpha$), flap's length to water depth ratio ($\frac{L}{h}$) and CoG will be considered as design parameters. In practice, the mass ratio and CoG-position can be achieved by actively controlling the amount of water entering certain chambers within the flap when submerged. Another option would be to increase the total length (L). However, increasing the length of the flap also increases the probability of an impact between the flap and landing crafts entering the dock.

This report focuses on four key design parameters based on the flap's equation of motion and the principle damped systems. Firstly, it will investigate the moment of inertia by adjusting the mass ratio $\alpha$ and the center of gravity position ($r_g$), which affects the radius of gyration (r). Secondly, it will explore variations in the restoring coefficient C by adjusting the center of gravity position. Thirdly, by altering the ratio of water depth (h) to flap length (L). Finally, it will analyze the impact of mechanical damping ($B_m$).

# 7

# Conclusions and Recommendations

## 7.1. Conclusions

In Part II the system engineering approach presented by Pahl [36] is adopted to choose the best concept solution. This approach is further supported by: interviews with employees of COMMIT, existing naval reports, doctrines and procedures related to LPD vessels. In the end, real understanding of the problem statement and constraints is achieved. This understanding is used to come up with a initial preliminary (concept) design. This makes it possible to answer the third sub-question.

3. ***"What wave attenuation solution design(s) effectively decrease(s) free surface motions within the well-dock?"***

The concept solution must fulfill six sub-functions to achieve the main objective: reflect waves, radiate waves, dissipate wave energy, be free to move to prevent obstruction and damage, be adjustable to different sea states and be impact-proof against landing vessels in both flooded and non-flooded conditions. By developing a working structure and considering various options to fulfill its (sub-)functions, one concept design is selected.

In shallow water conditions, such as those in a well-dock, the amplification of horizontal water particle motion is a great advantage. The concept solution features a bottom-hinged pitching flap, which exploits this advantage. The centre of rotation is placed close to the well-dock bottom, maximizing wave torque. By adjusting its CoG-position and hydrostatic coefficients this WAS can be tuned. When examining the EoM, four key design parameters are analysed for optimal attenuation performance: mass, position of the CoG, length, and mechanical damping in the hinge.

## 7.2. Recommendations

Several design choices and working principles were not selected due to the limitations of ComFLOW, restrictions stated by COMMIT or the limited time for this thesis. The most important recommendations for further improvements or research are listed below:

- In selecting the best option to fulfill a working principle, options based on turbulence were ignored due to limitations of ComFLOW's solvers. The same applies to very thin plated or flexible concepts. Further research could focus on these concept designs, which could potentially increase energy dissipation. In the end, all presented concept designs should be tested (e.g., model tests) to identify the best-performing solution.
- Currently, COMMIT has not stated any restrictions regarding when sloshing leads to halting amphibious operations. For this reason, there was no target value for free surface elevations. Further research could examine this limit by determining the "no-go" properties of waves within a well-dock.

- During the setup of the functional breakdown structure, a desk study was performed using LPD manuals for well-dock operations. Due to limited time and resources, these steps were not examined at the actual locations of a real LPD vessel. Applying field research could improve this functional breakdown structure, potentially leading to more restrictions or opportunities.
- This research did not examine the application of additional spring terms in the hinge of the flap or changes in thickness. Considering the equation of motion, these design parameters could further improve the dynamics of the pitching flap and possibly the wave attenuation performance.

# Part III

# Model 2: Wave Attenuation Solutions (WAS)

# 8

# Methodology

## 8.1. ComFLOW Set-up Strategy

In this section, the same steps and argumentation method as used in Model 1 will be used to explain the modelling choices as used in Model 1. One crucial point to highlight is that Model 1 provides the input wave profile for Model 2. Another point to mention is that the wave profiling can be carried out for different locations (St.0, S2.6, and S3.7) within the well-dock of the LPD, each containing its own individual wave profile. Within the scope of this research only position St.0 is examined.

### 8.1.1. System to model

In Figure 8.1, the entire well-dock of an LPD is depicted in a flooded condition. The red-boxed area outlines the boundary of the local model system within the total dock. This specific local domain is used to reduce computational time. Once the optimisation is completed, the solution will be tested in the full domain representing the entire well-dock.

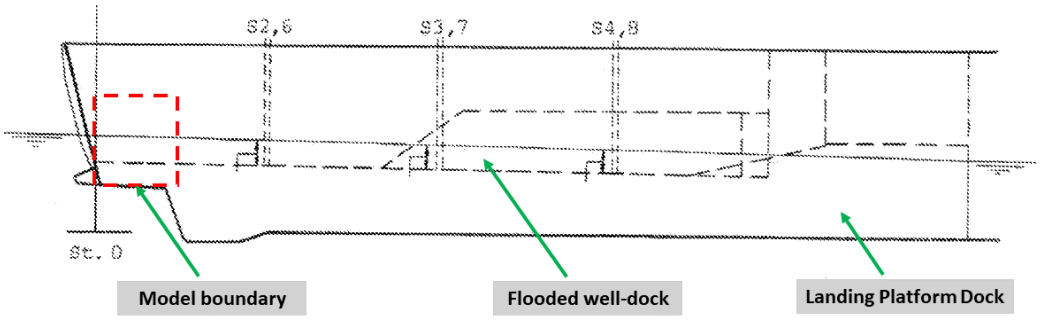


**Figure 8.1:** System model with boundary, depth at St.0 is 2.65 m [22]

### 8.1.2. Input and output of the system

A simplified image of the 2D system model is presented in Figure 8.2. The input waves are depicted in green, approximated with use of Model 1 in Part I. The outputs (reactions) are highlighted in red. Additionally, the GABC-boundaries and impenetrable well-dock floor are illustrated.

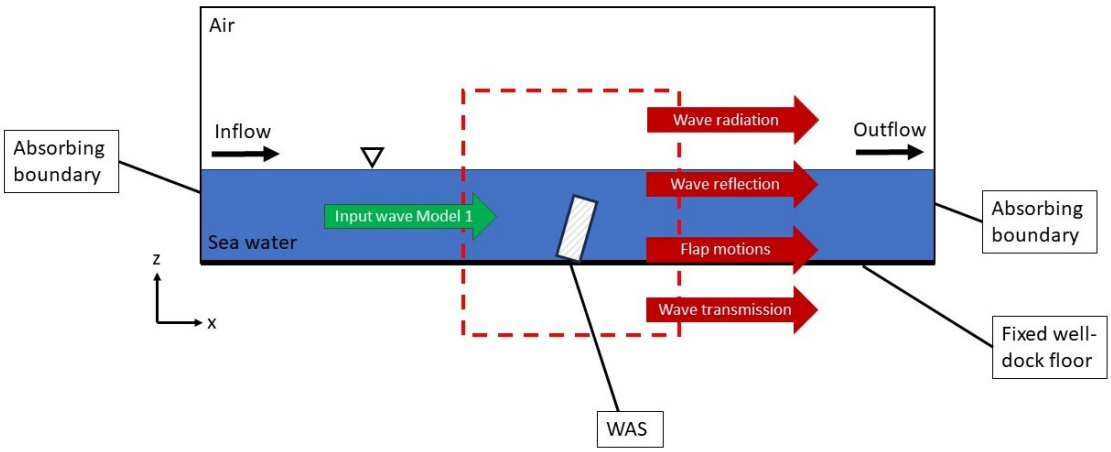


**Figure 8.2:** Input and outputs of the 2D local model system

### 8.1.3. Components and connections of the system

In the local system, several relevant components and connections can be identified. The components are presented in the enumeration below:

- Impenetrable non-moving well-dock bottom;
- Single Wave Attenuation System;
- Free surface.

Additionally, the connections are given below:

- Fluid-rigid body interaction between the rigid WAS and the seawater within the dock;
- Fluid-fluid interaction between incoming and reflected waves and radiated waves due to the presence of the WAS;

### 8.1.4. Model simplifications

Based on the findings and conclusions from Model 1 and the additional literature discussed in Subsection 2.2, the 2D local model can be simplified with the following assumptions:

*Environment:*

- Reflected waves due the beach ramp at the end of the well-dock are ignored (absorbing boundary conditions at outflow);
- Diffraction and radiation effects near the entrance of the well-dock are neglected;
- Turbulence caused by flap-motions is ignored.

*Structure:*

- The domain boundaries are fixed, so no forced heave and pitch motions are present;
- The well-dock floor will be parallel to the water surface (fixed water depth);
- Bottom friction from the well-dock floor is ignored;
- No landing craft vessel (e.g. LCU) is present within the well-dock, which influences the free surface motions;
- The WAS is a rigid submerged 1-DOF (pitch) moving body, no elastic deformation will take place;
- WAS's are modelled with the use of closed basic geometries, so no vents or slots that create turbulence or vortices are present;
- The WAS is prescribed with properties like mass (m), Centre of Gravity (CoG) and radius of gyration (r) using settings in ComFLOW.

*Fluid:*

- The input wave is approximated as a tuned super-position of linear wave components, as described in Section 4.2;
- Fluid is assumed to be an incompressible viscous fluid;
- The air is assumed to be a compressible viscous fluid;
- Fluid is modelled with unsteady Reynolds-Averaged Navier-Stokes equations;
- No turbulence model is applied during the simulations.

## 8.2. Validation Computational Model 2

A validation step must be conducted to determine the appropriate ComFLOW set-up strategy and settings. In this way, the motions and fluid-structure interactions of the implemented flap-type WAS are realistic and ensure accurate results.

### 8.2.1. Computational Set-up

Before validation-process can begin the right experimental data must be found. As mentioned in Section 6.2, the submerged flap type system seems most suitable for wave attenuation in the case of a well-dock with restricted water depth (shallow water to intermediate conditions). For this reason, the concept solution and hydrodynamic response can be compared to a submerged Oscillating Wave Surge Energy Converter (OWSEC).

The validation process will be carried out in two steps. Firstly, the 2D Numerical Wave Tank (NWT) will be modelled without any structure interfering with the incoming waves. A known simple wave input will be modelled and compared to analytical formulations. Secondly, the wave energy converter is placed into the NWT and the obtained results are compared with data gathered from experimental tests. The final goal is to achieve a maximum percentage error of 10% for both maximal rotation angles and angular velocities.

In the experiment, the wave flume measures 16.7 m in length and 0.65 m in width, with a flap-type wave maker situated at one end. The OWSC model is positioned on a flat bottom, approximately 12.2 m from the paddle wave maker. An absorbing beach, constructed with porous plates having a porosity of 8%, extends from 12.8 m to 16.3 m away from the wave maker and effectively absorbs incident waves. Seven wave probes track the wave propagation along the flume [20][55]. A 2D image illustrating the layout of the wave flume is provided in Figure 8.3.

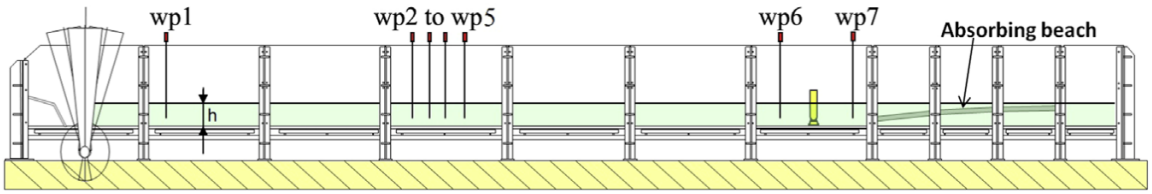


**Figure 8.3:** Experimental set-up in research paper [20]

### Computational domain

The next step involves building a computational domain in ComFLOW. To achieve this, a fixed domain with absorbing boundary (GABC) at the outflow of the NWT is defined. The dimensions and properties of the pitching flap mirror those detailed in Figure 8.3. The final setup shown in Figure 8.4 matches the experimental conditions (detailed zoomed images are available in Appendix A).

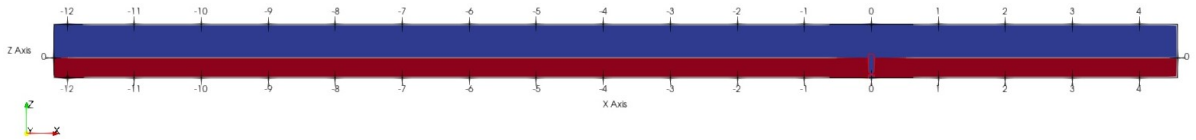


**Figure 8.4:** Computational set-up in ComFLOW

### Grid refinement

Following a mesh convergence analysis with a refinement ratio factor of two, the unrefined cell size is $\Delta x = 0.015$ m and $\Delta z = 0.015$ m. To enhance further accuracy, a refinement level of 2x2 is implemented in the area of the rotating flap. This yields a final refinement level of $\Delta d = 0.00375$ m in both the x- and z-directions. The $\Delta t$ is chosen based on accuracy and stability of the iteration process in ComFLOW. To start, the same time step is chosen as presented in the paper of Wei et al. [55]. Figure 8.5 depicts a zoomed view of the refinement levels near the flap.

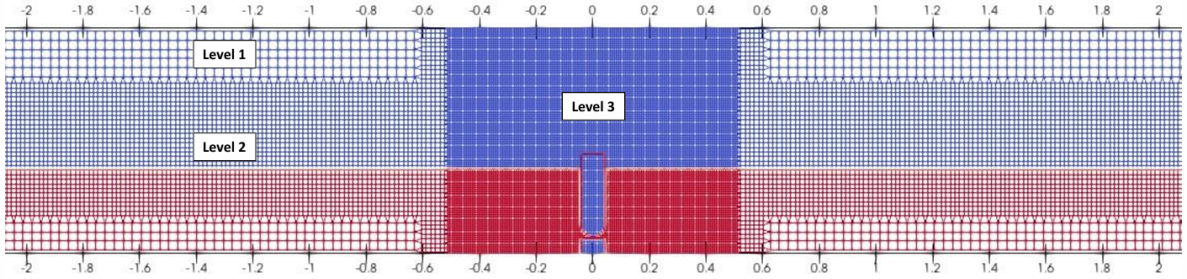


**Figure 8.5:** Refinement levels within computational domain of Model 2

### Validation

In Figure 8.6 the rotation angle of the numerical OWSEC model is compared to experimental data. The maximum errors are 9.5% in troughs and 8.5% in crests when measuring five oscillations. Thus, ComFLOW underestimates the rotation angle, which aligns with the findings presented by Henry et al. [20] and Wei et al. [55].

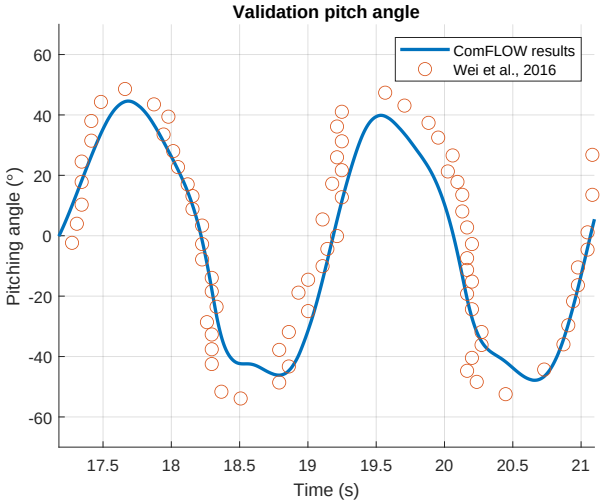


**Figure 8.6:** Comparison of flap rotation angle as a function of time

Next, in Figure 8.7 the flap's angular velocity is compared. This velocity aligns well with the experiment, where the crests show a maximum error of 6.8%. However, a notable difference of 33.6% is found in the troughs when experiencing non-linear slamming.

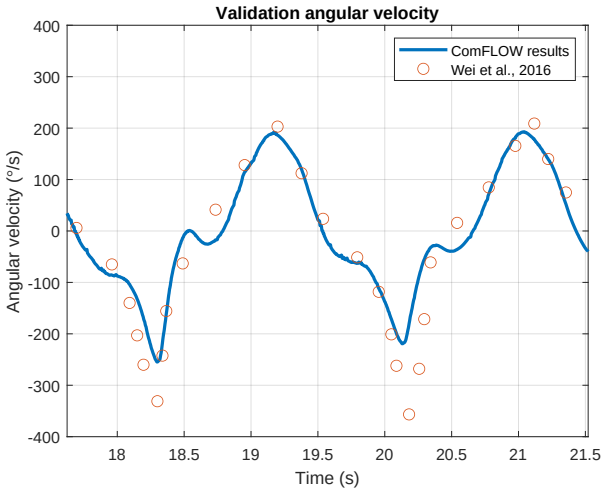


**Figure 8.7:** Comparison of flaps angular velocity a function of time

The significant error can be explained by examining Figure 8.8. This figure shows the difference in the drop in free surface elevation in front of the flap where slamming occurs. The images from the experiment clearly show a free surface decline, particularly when the flap is in upright position after rotating positively in the direction of the propagating wave. This gap allows the flap to increase its pitching angle and angular velocity [55].

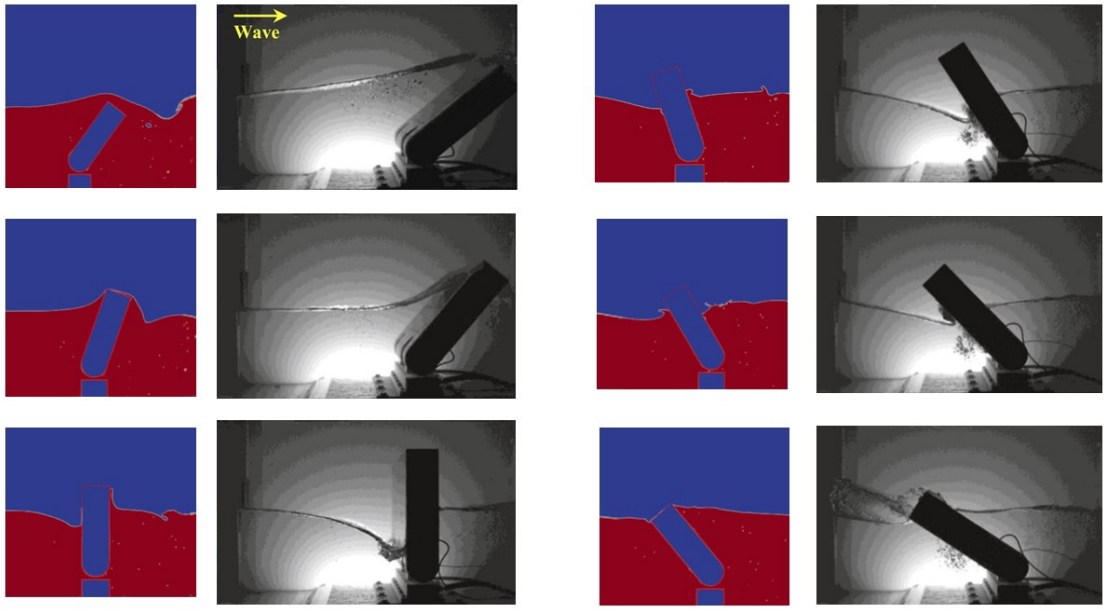


**Figure 8.8:** Comparison of flap rotation angle with use of images from the experiment of Henry et al., 2014 [20]

When analyzing all these results in the context of validation purposes, it can be concluded that ComFLOW reasonably predicts the rotational motions in non-linear conditions. The experiment focuses on coincidental waves in shallow water, examining the effect of slamming with a surface piercing flap. Due to these extreme non-linear conditions, the results are considered acceptable for use in this research due to several factors:

1. The experiment used a mechanical wave paddle to generate input waves with troughs at -0.5 m depth. In contrast, ComFLOW generated waves (Rienecker-Fenton wave theory) with slightly shallower troughs at -0.4 m depth. This difference could impact the rotation of the flap.
2. In the CFD simulation, the over-damped conditions require a notable decrease in water level to trigger slamming. As the water profile moved up the flap's front face, the profile stayed mostly horizontal. Conversely, in the actual experiment, the water surface dropped near the flap.
3. In extreme wave conditions, non-linear slamming events dominate over straightforward linear hydrodynamics. Therefore, using a coarse mesh and time step can lead to varying computational results.
4. As emphasized by the numerical benchmark introduced at the ISOPE Sloshing Symposium, the accuracy of numerical results is heavily reliant on the quality of grid refinement and temporal resolution during jet formation and evolution [20].
5. In this research, fully submerging the rotating flap eliminates potential non-linear slamming events that could otherwise affect its angular motion and velocity.
6. Fully submerging the flap eliminates wave reflections that could affect its rotation amplitude and phase angle, ensuring more consistent experimental conditions.
7. Within this research, submerging the flap ensures a constant restoring moment. In contrast, experimental conditions show that this moment varies with pitching angles, affecting the submerged volume over time.

In conclusion, it can be stated that the conditions in Model 2 are less severe compared to those in the experiment. The percentage error will decrease even more to acceptable levels because there is no occurrence of non-linear slamming. This conclusion is further supported with the following summarised arguments:

- Due to limitations in grid size or time step, the simulation does not capture the sudden pressure increases during slamming events that affects the flap's motion. This report addresses this issue by fully submerging the flap, which eliminates these pressure peaks.
- In a fully submerged scenario, non-linear events like air entrapment, jet formation, and time-dependent flap properties (e.g., restoring moment) are eliminated.
- The positive pitching angles and angular velocities show an error percentage below 10%, indicating that ComFLOW's dynamics are acceptable. These angles correspond to the region without non-linear slamming (right-side).

In Model 2 simulations, the validated numerical settings will be used, with a base cell size of $\Delta x = 0.015$ m and $\Delta z = 0.015$ m. Near the rotating flap, a 2x2 refinement will refine $\Delta d$ to 0.00375 m in both x- and z-directions. The simulation's time step will be set to $\Delta t = 0.001$ s.

## 8.3. ComFLOW Domain Set-up

In this section, the methodology for setting up the domain in ComFLOW for Model 2 will be explained. Using the validated settings from the previous section, the key components necessary for a domain setup will be discussed, including boundary conditions, geometry, computational grid, numerical settings and a wave model.

### 8.3.1. Computational Domain & Boundary Conditions

A fixed domain with absorbing boundaries (i.e. GABC) at the outflow is established to accommodate various input waves, including the approximated input wave from Model 1 in Part I. The simulations are conducted in two distinct domains presented in Figure 8.9 and 8.10. Initially, a single WAS is introduced into a smaller local domain to reduce computational time. Subsequently, the full computational domain, mirroring the characteristics of the well-dock, is analyzed. Both domains differ from Model 1 in several aspects. Firstly, they lack a well-dock bottom that is subject to motion induced by the LPD's movements in waves. Furthermore, the beach ramp is ignored to prevent interference from reflected waves. Lastly, the water depth is kept constant and therefore the actual sloped well-dock bottom is ignored.

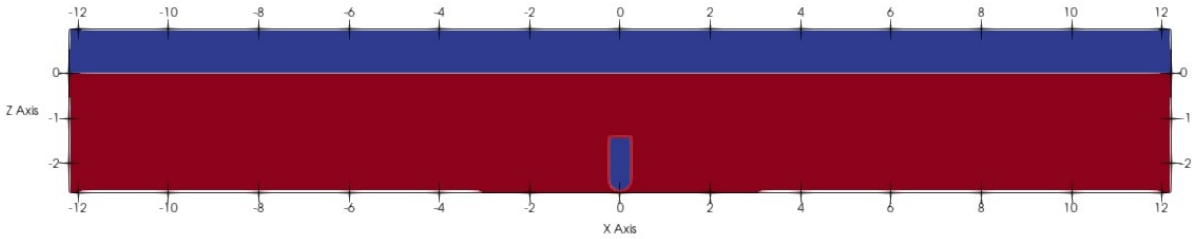


**Figure 8.9:** Local computational domain with a single WAS

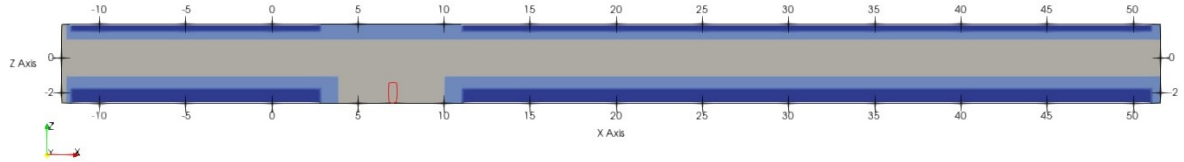


**Figure 8.10:** Full scale computational domain with a single WAS

These modelling choices will have the following effects:

- As waves travel over a sloped bottom, their speed slows due to the decrease in water depth. Shoaling becomes more pronounced, raising wave heights and producing steeper waves. This could result in faster wave breaking. However, Model 2 has a constant water depth, so wave shoaling is reduced. This could result in fewer waves breaking.
- Because of the constant water depth, waves travel at a relatively consistent speed over a flat bottom. Resulting in a more uniform energy distribution across the wave front and fewer variations in wave energy.
- In Model 1, the combined pitch and heave motion of the well-dock bottom alters the water depth in relation to the free surface at various points along the well-dock over time. The varying water depth can affect wave velocity by accelerating or decelerating the contained fluid. Furthermore, changing depth can intensify the shoaling effect at specific times and locations, resulting in higher wave heights and potentially earlier wave breaking.
- Ignoring a beach ramp at the end of the well-dock eliminates interference, which can lead to wave breaking and energy dissipation. Furthermore, reflected waves from the ramp may interact with the WAS and incoming waves (wave-wave interaction), which reduces or improves the effectiveness of the flap's wave attenuation performance.

### 8.3.2. Geometry

Different WAS configurations are installed based on four design parameters ($\alpha$, L/h, CoG, and $B_m$). Initially, all had identical dimensions, as shown in Figure 8.11.

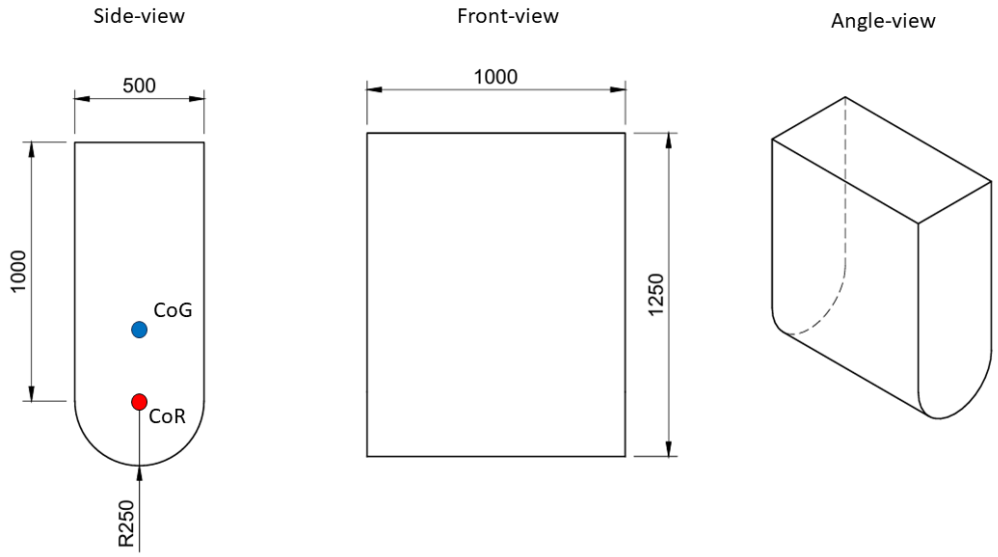


**Figure 8.11:** Sketch of initial WAS configuration, side-view (left) and front-view (middle), dimensions are in mm.

The concept model maintains the same dimensional ratio as the computational geometry properties used in the validation process with the flap utilized in Wei et al. [55]. The flap's height is constrained by the maximum draft of 1.4 m for the LCU (loaded condition). The Center of Rotation (CoR) is located at the red dot, 2.35 m from the free water surface, representing the flap's hinge. The CoB is 0.38 m above the CoR, marked with a blue dot. The technical drawings were created with Autodesk Fusion, and the CoB position was calculated using BEM software.

### 8.3.3. Computational Grid

The grid settings, validated by Wei et al. [55], are extrapolated with equal number of cells per wavelength and wave amplitude. Figure 8.12 illustrates the various grid refinement levels.

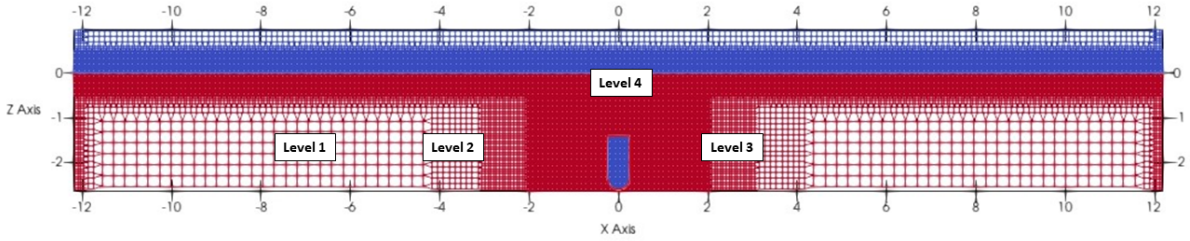


**Figure 8.12:** Local computational domain with grid level (single WAS included)

### 8.3.4. Numerical Settings

In Model 2, the same numerical settings are used as in the validation process. Exact properties can be found in the Table 8.1.

| Numerical setting | Applied setting | Unit |
|---|---|---|
| $\Delta$t | 0.001 | s |
| $\Delta$x, z (flap surface) | 3.75 | mm |
| CFL | 0.5 < CFL < 0.9 | - |
| BC (inflow and outflow) | GABC | - |

**Table 8.1:** ComFLOW settings local domain within Model 2

### 8.3.5. Wave modelling

In the local and full scale domains, various input waves are used to evaluate the WAS's wave attenuation capabilities. Linear Airy waves are used as input for the simulation in the small domain. The wave period and wave height are adjusted to allow for the use of linear wave theory, which serves as a foundation for analysing flap dynamics in relation to wave attenuation. With this approach the performance of the single flap can be optimised in a shorter computational time. In addition, Stokes' second-order wave theory is applied by increasing the wave height. The results are compared to see if wave (non-)linearity influences flap's performance. Finally, the optimised flap configuration from the local domain is integrated into the full scale domain. In this case, the approximated wave from Model 1 is used.

## 8.4. Free Decay Test

In offshore engineering and naval architecture, a common approach to determine damping coefficients and natural periods, both linear and non-linear, is through free decay tests [15]. In these tests, the flap is displaced with a known pitching angle and released in still water. With no applied mechanical damping ($B_m$) and no presence of excitation waves, the flap oscillates at its damped natural period ($T_d$), driven purely by its restoring buoyancy moment $C$.

Note that the calculation of the described properties is based on solving ordinary differential equations (ODE's). Hereby, it is assumed that damping remains constant over the amplitude of the oscillation. Finally, the constant damping coefficients can be derived from the peak-to-peak decay of the oscillation [2][14][39].

### 8.4.1. Method of free decay test

The oscillation period of a damped body can be characterized when it is released from an initial pitching angle of displacement. In this case an angle of $\theta$ = 20.0° is used.

$$T_d = \frac{T_n}{\sqrt{(1-\zeta^2)}} \tag{8.1}$$

Where $T_n$ is the undamped natural period of the flap and $\zeta$ the damping ratio.

In order to analyse the damping during the decay test, the logarithmic decrement method is applied [25][24][26]. The logarithmic decrement $\delta$ is first calculated with Equation 8.2, then Equation 8.3 is applied for the damping ratio $\zeta$:

$$\delta = ln\left(\frac{\theta_{a_i}}{\theta_{a_{i+1}}}\right) \tag{8.2}$$

$$\zeta = \frac{1}{\sqrt{1+\left(\frac{2\pi}{\delta}\right)^2}} \tag{8.3}$$

It is important to note that these decay tests do not provide information about the relationship between the potential coefficients and the frequency of oscillation. This is because decay tests are conducted at only one frequency, which is the natural frequency [26].

## 8.5. Measuring Wave Attenuation Performance

The effectiveness of the applied WAS will be determined by measuring the power flux difference ($\Delta P$). The method for calculating this value for one wave component was already explained in Section 2.1.2. However, with the use of the resuts of Part I, a more accurate method supported by CFD-results can be applied. This refined approach will enhance the precision of assessing the WAS's effectiveness.

Figure 4.10 shows that the measured free surface signal consists of a summation of regular wave components (irregular wave). To calculate the power flux for all individual components Equation 8.4 is used.

$$P_{energy} = \rho \cdot g \cdot \sum_{i=1}^{N} E\{\frac{1}{2}a_i^2\} \cdot c_{gi} \tag{8.4}$$

From Figure 4.10 in combination with Figure 2.1, the regime is characterized by shallow water conditions. For this reason, the phase velocity ($c$) becomes the group velocity ($c_g$) [21]. This phase velocity will be determined using an iterative Newton-Raphson method in MATLAB with use of Equations 8.5 and 2.5 [60].

$$kh \approx x_0 - \frac{f(x_0)}{f'(x_0)} = x_0 \left[\frac{k_0 h + \left(\frac{x_0}{\cosh x_0}\right)^2}{x_0 \tanh x_0 + \left(\frac{x_0}{\cosh x_0}\right)^2}\right] \tag{8.5}$$

Where $f(x) = x \tanh x - k_0 h$ and $f'(x)$ is the first derivative. Furthermore, $x_0$ is the initial guess for $kh$ and $k_0 h$ the relative water depth. After iterating Equation 8.5 with the use of the initial guess of $x_0$, the wave number $k$ can be determined. The wave number is then used to determine the phase velocity for each single wave component of the irregular wave. Finally, the individual phase velocities are used in Equation 8.4 to determine the power flux.

The free surface elevation is first measured without the WAS. Then, the power flux is calculated using Equation 8.4, serving as a reference. New simulations are then conducted with the WAS configurations included. Again, the free surface elevation is measured at the exact same location and the new power flux is calculated. Finally, the difference between the two results is calculated in both $J/s/m$ or $W/s$ and percentage. This final outcome presents the wave attenuation performance of different WAS designs. Note that this result only shows the total wave attenuation performance and does not differentiate between the amounts of reflected or dissipated wave energy. This is a recommendation for further research.

# 9

# Results & Discussion

In this chapter, Model 2 is used to analyse and optimise the hydrodynamic performance of the WAS, both in small and full scale. First, the linear Boundary Element Method (BEM) is used to calculate the added mass moment of inertia A($\omega$) and radiation damping coefficient B($\omega$) in frequency domain. Finally, four design parameters (listed below) are adjusted to optimise wave attenuation performance.

- Mass ratio $(\alpha)$;
- Length ratio $(\frac{L}{h})$;
- Distance from hinge to CoG $(r_g)$;
- Mechanical applied damping $(B_m)$ .

Changing the mass ratio $\alpha$, which is the ratio between the seawater density ($\rho_w$) and the homogeneous density of the flap ($\rho_f$), will affect the restoring moment $C$ (Equation 9.1 [29]), the moment of inertia $I_m$ (Equation 9.2 [16]) and the radius of gyration $r$ (Equation 9.3).

$$C = g \cdot t_f \cdot W \cdot L \left(\rho_w \cdot r_b - \rho_f \cdot r_g\right) \tag{9.1}$$

$$I_m = \frac{1}{12} \cdot \frac{\rho_f}{\rho_w} \cdot \left(L^2 + t_f^2\right) + \frac{\rho_f}{\rho_w} \cdot r_g^2 \tag{9.2}$$

$$r = \sqrt{\frac{I_m}{m}} = \sqrt{\frac{I_m}{\frac{\rho_f}{\rho_w} \cdot W \cdot L \cdot t_f}} \tag{9.3}$$

Where $t_f$, $W$, $L$, $r_b$, and $r_g$ are respectively the flap's thickness, width, length, moment arm to center of buoyancy and center of gravity (from hinge). These five parameters remain constant during the sensitivity study of the mass ratio.

Next, by changing $\frac{L}{h}$, the length of the flap L is increased with respect to the water depth h. Keeping all other parameters constant will also alter the outcomes of Equations 9.1 to 9.3. Another effect of the increased length is the increase in added mass moment of inertia and the radiation damping coefficient. Therefore, due to the draft of the LCU a primary length ratio of 0.377 (-) is chosen as primary configuration.

Equations 9.1 to 9.3 are also affected by changing the position of the centre of gravity $r_g$. Increasing the distance or moment arm from the CoG to the hinge reduces the restoring moment C while increasing the moment of inertia $I_m$, thereby increasing the radius of gyration. Finally, the (mechanical) damping coefficient $B_m$ is adjusted. All other parameters remain constant.

## 9.1. Hydrodynamic Analysis with Linear Boundary Element Method (BEM)

Before the design optimisation can be started with ComFLOW , the initial WAS configuration is tested using BEM. The primary benefits of BEM simulations are their short computational time and valuable insights into the system's hydrodynamic behaviour. However, the BEM simulations used in this report are unable to implement non-linear effects. As a result, only harmonic forces can be used as input, allowing the harmonic motion of the object to be modelled accurately.

Simulations are performed using the open-source software Hydrodynamic Analysis of Marine Structures (HAMS) [58], which is supported by the hydrodynamic coefficients viewer BEMRosetta [61]. This solver calculates linear hydrodynamic coefficients, excitation forces and moments. With these results, the RAO can be computed using MATLAB and Equation 9.4.

$$\text{RAO}(\omega) = \frac{M_0}{C - (I_m + A(\omega))\omega^2 + iB(\omega)\omega} \tag{9.4}$$

Where $M_0$ is the complex linear excitation moment amplitude.

During BEM simulations, the length ratio is initially set to 0.377 (-), considering the maximum length relative to the maximum draft of 1.4 m of the LCU. Therefore before proceeding further a grid sensitivity analysis is performed to achieve convergence. This is ultimately reached with a grid size of $\Delta$x = 0.05 m, $\Delta$y = 0.05 m and $\Delta$z = 0.05 m. The final results are shown in Figure 9.1 to 9.4.

Figure 9.1 shows that the difference between the maximum and minimum added mass moments of inertia is 2.1%. This means that variations in wave frequency have little effect on the added mass of inertia. The added mass moment of inertia at frequency infinity, A($\infty$), yields a value of 146.2 $kg{\cdot}m^2/rad$. This information is then used to calculate the natural period of the pitching flap.

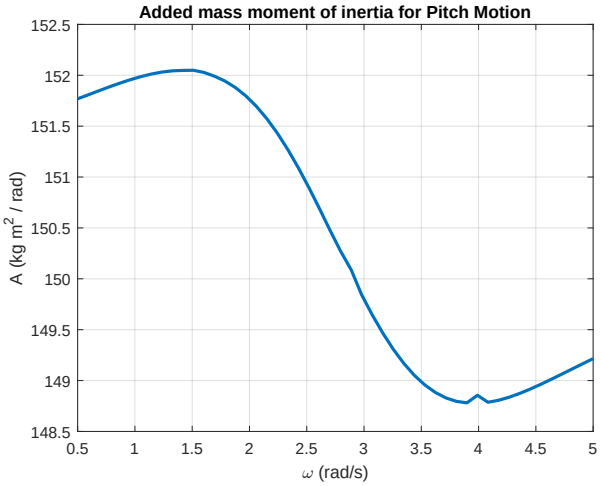


**Figure 9.1:** Added mass calculated with BEM for a flap with L/h = 0.377 (-)

BEM also determines the radiation damping coefficient, B($\omega$). Figure 9.2 shows that the maximum damping occurs at a frequency of 2.9 rad/s, which is equal to a wave period of 2.1 s. As a result, it is assumed that during the CFD simulations, this particular wave frequency will exhibit greater wave attenuation than lower wave frequencies.

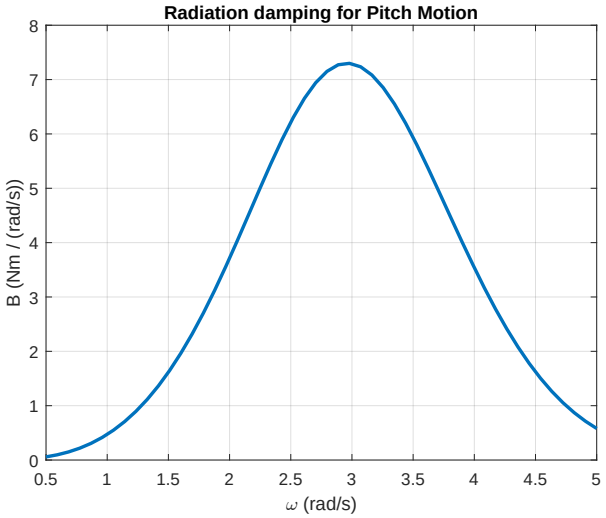


**Figure 9.2:** Radiation damping calculated with BEM for a flap with L/h = 0.377 (-)

HAMS is also used to perform motion decay tests. The results represent a system's response to an impulse input (Kirf Impulse Response function), which provides useful information about the system's dynamic characteristics. This includes the natural frequency, damping ratio and oscillating response to sudden forces [31]. Figure 9.3 summarises the findings.

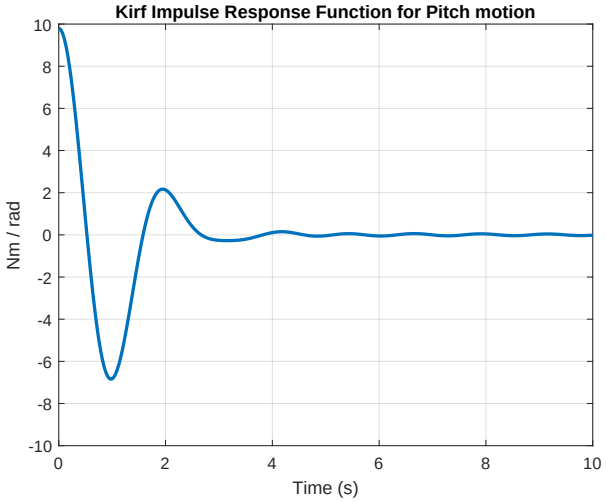


**Figure 9.3:** Kirf impulse response function for pitch with BEM for a flap with L/h = 0.377 (-)

Figure 9.3 clearly demonstrates that the motion of the flap is damped. Following the impulse, the system reaches a new equilibrium in just 2.6 s. This demonstrates a small overshoot, followed by a steady state. The logarithmic decrement method can be used to calculate the damping ratio and (damped) natural period. The values are shown in Table 9.1.

| $T_d$ (s) | $\zeta$ (-) | $T_n$ (s) |
|---|---|---|
| 2.23 | 0.30 | 2.12 |

**Table 9.1:** Results Kirf response function in BEM

It can be concluded that the flap experiences relatively high damping due to radiation damping alone. When comparing the damped natural period to the period in Figure 9.2, which shows the highest radiation damping, it is clear that the flap oscillates with the same period/frequency. Only a 3.4% difference is observed. It is important to note that the damping computed using linear potential theory only represents the energy dissipated by radiated waves and ignoring the energy dissipated by viscous forces [33]. When the same simulation is run in ComFLOW, where viscous effects are present, the damping could increase even more.

Finally, RAOs are calculated for different CoG positions. The change in this design parameter affects the moment of inertia and the restoring moment. By plotting the differences, the effect on the flap's dynamics can be investigated. Figure 9.4 presents the results.

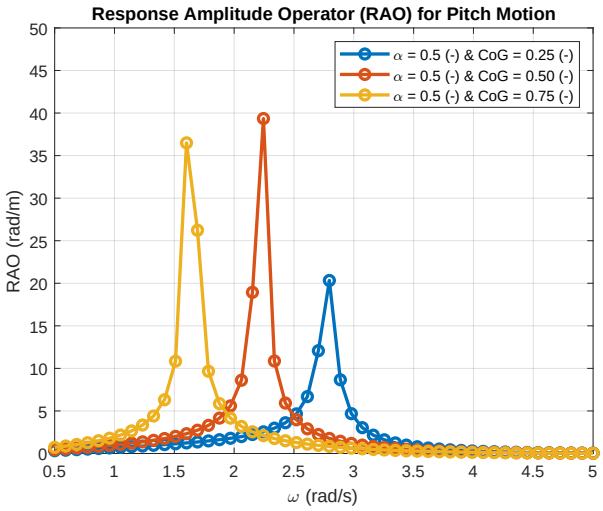


**Figure 9.4:** Different RAOs for a flap with L/h = 0.377 (-) and different CoG-positions

The damped natural frequency at CoG positions 0.25 (-), 0.5 (-) and 0.75 (-) are 2.8 rad/s, 2.2 rad/s and 1.6 rad/s respectively. Changing the CoG, and thus the ratio of inertia and restoring moment, will have several consequences. To begin, lowering the CoG and thus reducing the distance between the hinge and the CoG increases the restoring moment while decreasing the moment of inertia, resulting in a higher natural frequency. Equations 9.1 and 9.2 demonstrate this, along with Equation 9.5:

$$\omega_n = \sqrt{\frac{C}{I_m + A(\omega)}} \tag{9.5}$$

Figure 9.4 shows that a higher position of the CoG leading to a larger moment arm, results in a decrease in natural frequency. This corresponds to longer wave periods. It should be noted that the RAO graphs have high values in the region of resonance. In real-world scenarios, these motions are further restricted by non-linear damping terms such as drag and viscous effects or friction.

Furthermore, the peak increases as the graph shifts to the left. Figure 9.2 provides an explanation for this. When the natural frequency approaches the frequency with the highest radiation damping, the RAO curve is lowered (dampened). The damping terms dominate the motions and extract energy from the system because the velocity is highest and the damping is proportional to this velocity [23][47].

The BEM results show that a flap with the natural frequency set to the wave frequency with the highest radiation damping produces the greatest system damping. Thus, the amount of wave radiation is maximised. In this way, the flap acts only on the principles of radiation damping, requiring no additional mechanisms and thus improving the maintainability as desired by COMMIT (see Section 6.1.2). In this research it is assumed that increasing wave radiation will cause a decrease in wave elevations due to: destructive interference, wave energy redistribution and losses due to viscous effects.

## 9.2. Hydrodynamic Analysis with Numerical Free Decay Test

In this section, the results from the free decay tests performed in ComFLOW are presented. The simulation employs the WAS properties listed in Table 9.2.

| Property | CoG = 0.25 | CoG = 0.50 | CoG = 0.75 | Unit |
|---|---|---|---|---|
| $I_m$ | 34.6 | 58.5 | 95.7 | $kg \cdot m^2$ |
| A($\infty$) | 146.2 | 146.2 | 146.2 | $kg \cdot m^2$ |
| C | 1301.5 | 907.5 | 513.4 | N/m |
| r | 0.37 | 0.49 | 0.63 | m |
| $t_f$ | 0.5 | 0.5 | 0.5 | m |
| L/h | 0.377 | 0.377 | 0.377 | - |
| W | 1.0 | 1.0 | 1.0 | m |
| $\alpha$ | 0.5 | 0.5 | 0.5 | - |

**Table 9.2:** Properties WAS during free decay test in ComFLOW with fixed $\alpha$=0.5 and different CoG

### 9.2.1. Free surface elevation

Figure 9.5a shows that the free surface elevation behind the WAS varies with time for all three CoG values. The crests and troughs differ, indicating that the CoG influences radiated wave dynamics. The initial peak at 2.0 s is highest for CoG = 0.25 (-) and lowest for CoG = 0.75 (-), indicating that a lower CoG amplifies the initial radiated wave more significantly. This is logical because the natural period shortens, making it more tuned to the period with the greatest radiation damping.

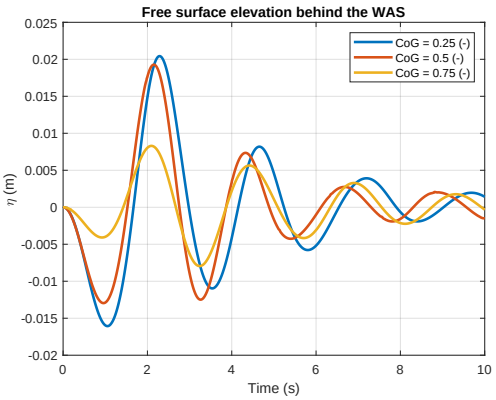


**(a)** Free surface elevation behind WAS, with varying CoG

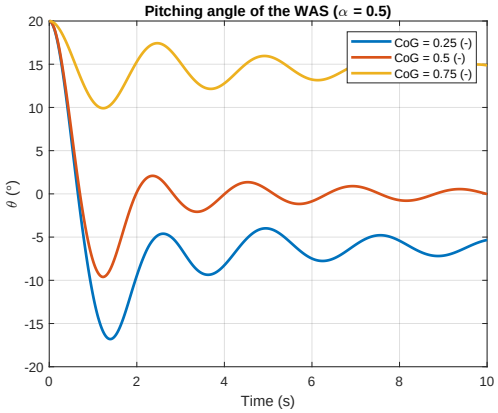


**(b)** Pitching angle of WAS, with varying CoG

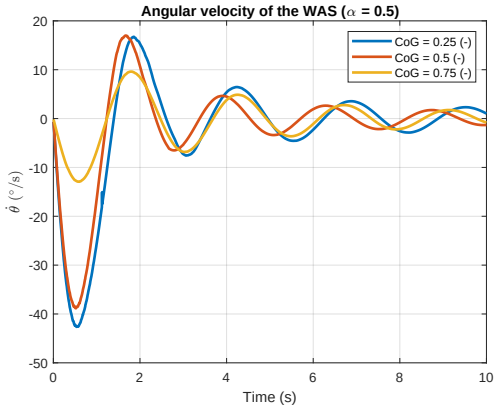


**(c)** Angular velocity of WAS, with varying CoG

**Figure 9.5:** Free decay properties of WAS configuration with different CoG positions

### 9.2.2. WAS dynamics

Observing the dynamics of the flap reveals that all three CoG positions exhibit damped oscillatory behaviour. However, the motion amplitudes, angular velocities and phases vary. CoG = 0.25 (-) exhibits the greatest initial amplitude oscillation, while CoG = 0.75 (-) exhibits the least, indicating that a lower CoG produces more pronounced oscillation. In addition, the three CoG values show slight phase shifts.

Further examination of Figure 9.5b reveals that lower CoG values cause the highest initial oscillation after release, which is quickly damped. A lower CoG indicates that the mass is concentrated near the hinge, making the system more stable in terms of tipping over. However, this implies that the system has a lower moment of inertia around the pitching axis. With a lower moment of inertia, the system is more responsive to external excitation's, resulting in higher initial oscillations and angular velocities. This also explains why the free surface elevation in Figure 9.5a is highest. This is due to the velocity-dependent hydrodynamic damping coefficient, which results in increased wave radiation [26].

The resistance caused by radiation damping reduces motion after being released from the initial position. When the CoG is further from the hinge, the opposite effect occurs. This is due to the decreased restoring moment, which results in a decrease in angular velocity.

Calculating the (damped) natural period is clearly not possible. The configurations with CoG = 0.25 (-) or 0.75 (-) show that after releasing from its initial pitching angle of $20.0°$, the flap quickly reaches equilibrium. From this point onward, the flap oscillates with a very small angle of $2.0°$ around the new equilibrium. This behaviour is thus assumed to be the result of numerical error (steady-state error) and cannot be used to calculate the damped natural period or damping ratio.

The configuration with the CoG equal to the CoB will result in oscillatory motion. The results show a 3.6% difference between the BEM and ComFLOW simulations for the natural period. The damping ratio differs by 10%, probably due to non-linear quadratic viscous damping. Besides, in this CFD simulation the flap has a damped natural period, which is close to the period of maximum radiation damping.

| $T_d$ (s) | $\zeta$ (-) | $T_n$ (s) |
|---|---|---|
| 2.15 | 0.27 | 2.10 |

**Table 9.3:** Free decay test in ComFLOW for CoG = 0.5 and $\alpha = 0.5$

In conclusion, the CoG location influences flap dynamics, affecting wave radiation and the damping ratio. A flap with a higher pitching angle and angular velocity produces the most wave radiation, effectively dissipating energy. This is achieved by matching the flap's natural frequency to the highest radiation damping coefficient.

### 9.2.3. Mass ratio

The optimal configuration, shown in Figure 9.5, will be further investigated. The mass ratio was changed to investigate its impact. Table 9.5 demonstrates how this change impacts other parameters. The findings indicate that changing this ratio has no significant effect on radiated wave oscillations, pitching angle, or angular velocity. Only a minor phase shift is observed in all the outcomes. The consistent results are most likely due to the submerged volume's dominant restoring moment and the low variations in mass moment of inertia. This results in a constant radius of gyration across all configurations.

| **Property** | $\alpha$ **= 0.1** | $\alpha$ **= 0.50** | $\alpha$ **= 0.9** | **Unit** |
|---|---|---|---|---|
| $I_m$ | 6.9 | 34.6 | 62.3 | $kg \cdot m^2$ |
| A($\infty$) | 146.2 | 146.2 | 146.2 | $kg \cdot m^2$ |
| C | 1712.3 | 1301.5 | 890.8 | N/m |
| r | 0.37 | 0.37 | 0.37 | m |
| $t_f$ | 0.5 | 0.5 | 0.5 | m |
| L/h | 0.377 | 0.377 | 0.377 | - |
| W | 1.0 | 1.0 | 1.0 | m |
| CoG | 0.25 | 0.25 | 0.25 | - |

**Table 9.4:** Properties WAS during free decay test in ComFLOW with fixed CoG = 0.25 and different $\alpha$

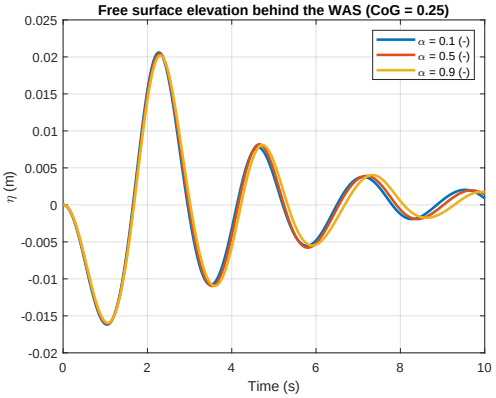


**(a)** Free surface elevation behind WAS, with varying $\alpha$

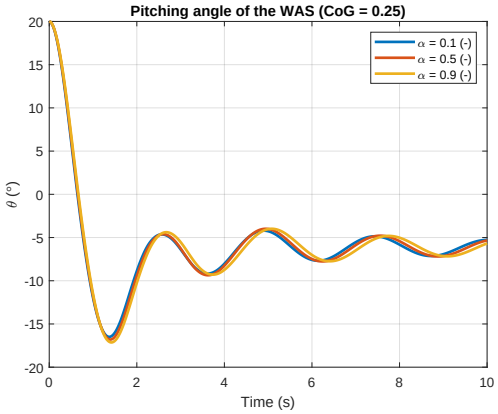


**(b)** Pitching angle of WAS, with varying $\alpha$

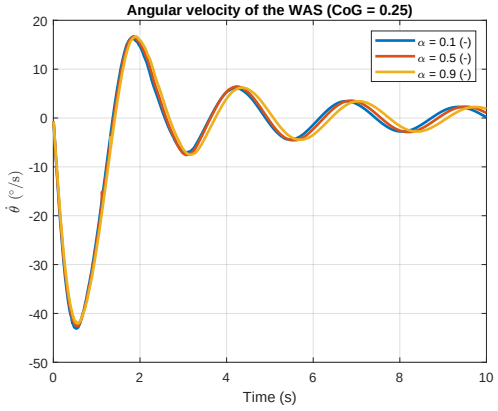


**(c)** Angular velocity of WAS, with varying $\alpha$

**Figure 9.6:** Free decay properties of WAS configuration with different $\alpha$ ratios

### 9.2.4. Length ratio

Figure 9.7 depicts the length ratio and allows for several conclusions regarding the amount of radiated waves and damping ratio. To begin, increasing the flap surface area results in a higher surface amplitude, implying that a larger flap surface area produces higher amplitude radiation waves. This can be used to generate destructive interference and improve wave attenuation performance. Second, by examining the pitching angle and angular velocity, it is clear that increasing the length of the flaps, and thus the frontal area, results in smaller angles and velocities. The natural period (i.e. 4.3 s) becomes higher as $I_m$ and A values increase. Ultimately, increased radiation damping coefficients due to large volume result in an increase in the damping ratio ($\zeta$ = 0.31).

| Property | L/h = 0.377 | L/h = 0.6 | Unit |
|---|---|---|---|
| $I_m$ | 34.6 | 145.7 | $kg \cdot m^2$ |
| A($\infty$) | 146.2 | 432.1 | $kg \cdot m^2$ |
| C | 1301.5 | 2737.9 | N/m |
| r | 0.37 | 0.59 | m |
| $t_f$ | 0.5 | 0.5 | m |
| $\alpha$ | 0.5 | 0.5 | (-) |
| W | 1.0 | 1.0 | m |
| CoG | 0.25 | 0.25 | (-) |

**Table 9.5:** Properties WAS during free decay test in ComFLOW with fixed $\alpha$ = 0.5 and different L/h

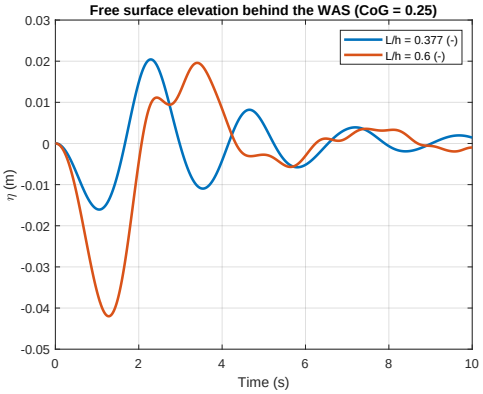


**(a)** Free surface elevation behind WAS, with varying $L/h$

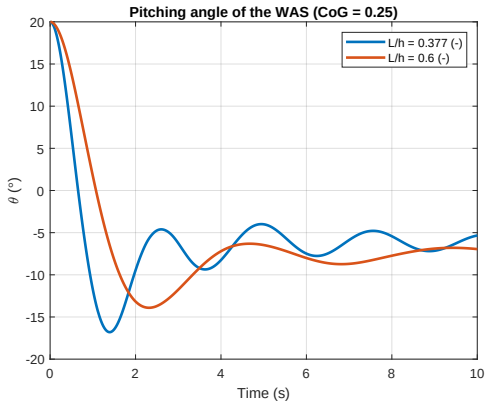


**(b)** Pitching angle of WAS, with varying L/h

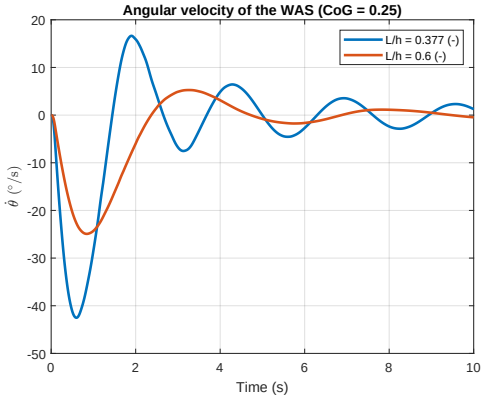


**(c)** Angular velocity of WAS, with varying L/h

**Figure 9.7:** Free decay properties of WAS configuration with different L/h ratios

### 9.2.5. Conclusions

The analysis of WAS dynamics, including linear damping ratio and radiated wave amplitudes, reveals that optimal performance requires a low CoG. This is the result of multiple observations. First, with a lower CoG, the flap is tuned to higher frequencies, resulting in larger pitching angles and angular velocities. In this way, the flap is precisely tuned to achieve the greatest amount of radiation damping possible. In the upcoming section, it is assumed that input waves with a period of 2.5 s, which corresponds to the WAS's damped natural period and highest radiation damping coefficient, will produce the best wave attenuation results.

## 9.3. Hydrodynamic Design Optimisation (single WAS in local domain)

To improve the wave attenuation, the hydrodynamic response and attenuation performance of a WAS in waves are investigated. To accomplish this with use of CFD, the follow the steps are taken: First, design parameters are adjusted to generate multiple WAS configurations. Second, the pitching angle ($\theta$) and angular velocity ($\dot{\theta}$) caused by wave excitation are analysed. This is done to understand the flap's dynamics in relation to its wave energy attenuation performance. Finally, the surface elevations behind the WAS are measured to assess wave energy transport. This data allows for the calculation of wave energy attenuation caused by the presence of the flap.

All results will be plotted against the design parameters $\alpha$, $CoG$, and $B_m$. Finally, this procedure will be repeated for different wave periods and wave heights.

### 9.3.1. Hydrodynamics in Linear Waves (Airy) with ComFLOW:

Appendix B shows graphs for a single WAS, excited by linear regular waves with a wave height of H = 0.2 m, a constant water depth of 2.65 m, and a flap length ratio of 0.377 (-). We will look at three parameters: the mass ratio, the location of the CoG and the period of the input wave. This analysis eventually focuses on measuring the pitching angle, angular velocity and power flux difference to better understand the wave dynamics that affect wave attenuation performance.

### 9.3.2. Hydrodynamics in Non-linear Waves (2nd Order Stokes) with ComFLOW:

In this paragraph, the wave height will be increased to H = 0.4 m. This increase results in second-order Stokes waves. The purpose of this adjustment is to investigate the effects of non-linear waves on the WAS's hydrodynamics and wave attenuation performance. The results are obtained by measuring the steady-state time signal of the free surface elevation, pitching angle and filtered angular velocity signals. The FFT analysis was performed using a sample of five periods.

#### Design parameter: centre of gravity and mass ratio

Figure 9.6 shows that when CoG = 0.25 (-), changing the mass did not affect the dynamics of the flap. This conclusion holds when the flap is excited by second-order Stokes waves. Figures 9.8a and 9.8b show that the pitching angle and angular velocity are nearly constant over the entire mass ratio range. When the CoG exceeds the CoB and the mass is increased, the angle and velocity increase slightly. Which is caused by the dominant restoring moment.

Furthermore, as the CoG increases, the inertia also increases, being proportional to the square of the distance from the hinge to the CoG. Resulting in an increased radius of gyration (see Table 9.2). A higher radius of gyration means that more wave torque is required to rotate the flap. In the end, this makes the flap more resistant to changes in rotational motion.

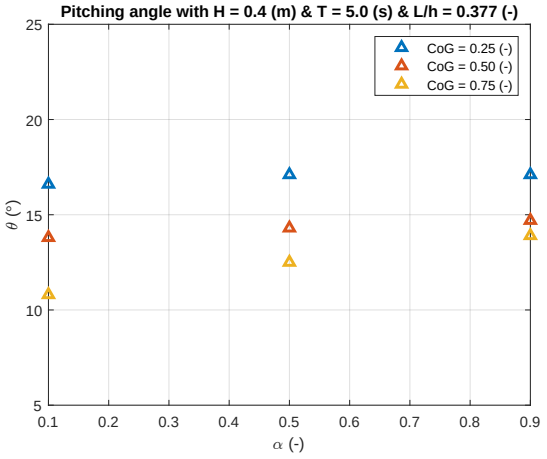


**(a)** Pitching angle of WAS, with varying CoG and $\alpha$

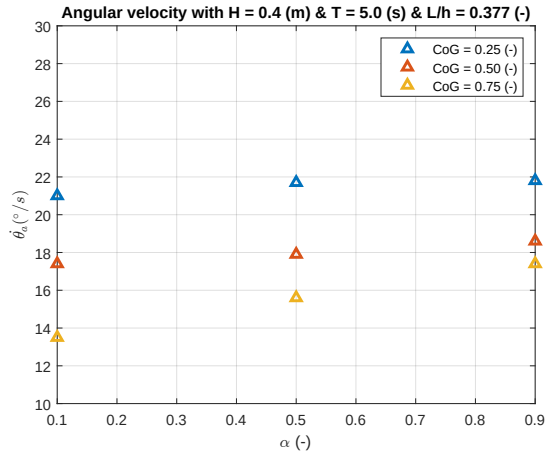


**(b)** Angular velocity of WAS, with varying CoG and $\alpha$

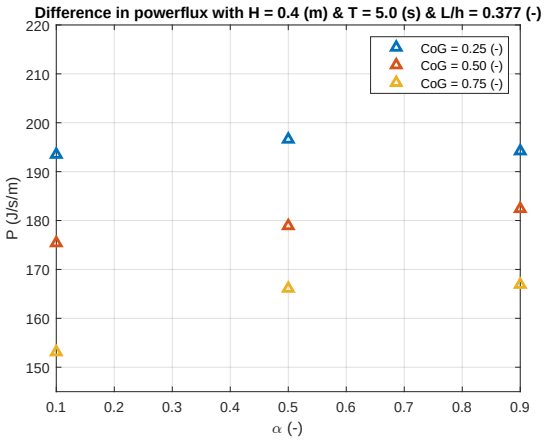


**(c)** power flux difference due to WAS, with varying CoG and $\alpha$

**Figure 9.8:** WAS dynamics in relation with power flux difference

The differences in free surface elevations are further examined in time domain. This is done by looking at the best and worst performing WAS configuration as seen in Figure 9.8c. The following configurations will be compared:

**Best performing:** CoG = 0.25 and $\alpha = 0.5$, with T = 5.0 s
**Worst performing:** CoG = 0.75 and $\alpha = 0.1$, with T = 5.0 s

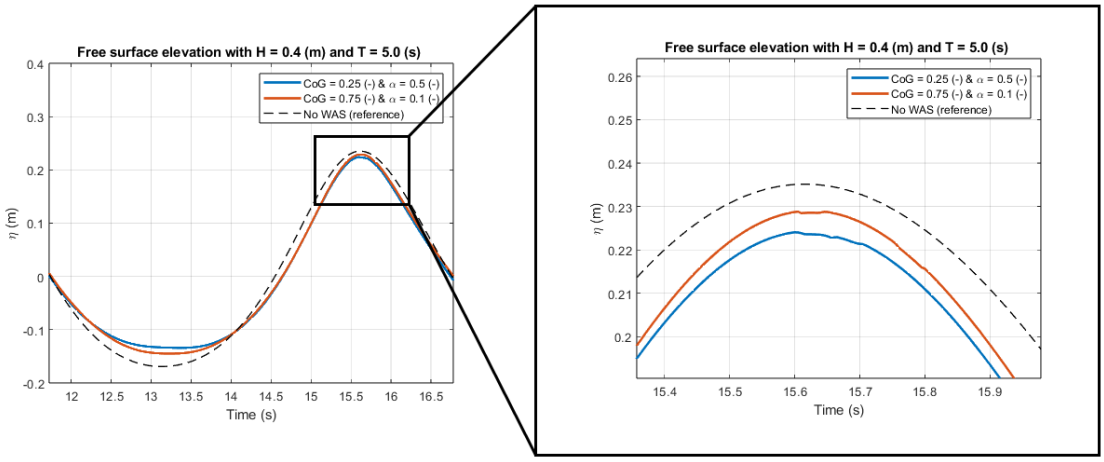


**Figure 9.9:** Free surface elevation behind the best and worst performing WAS in time domain, when examining CoG and $\alpha$ (zooming in on crest)

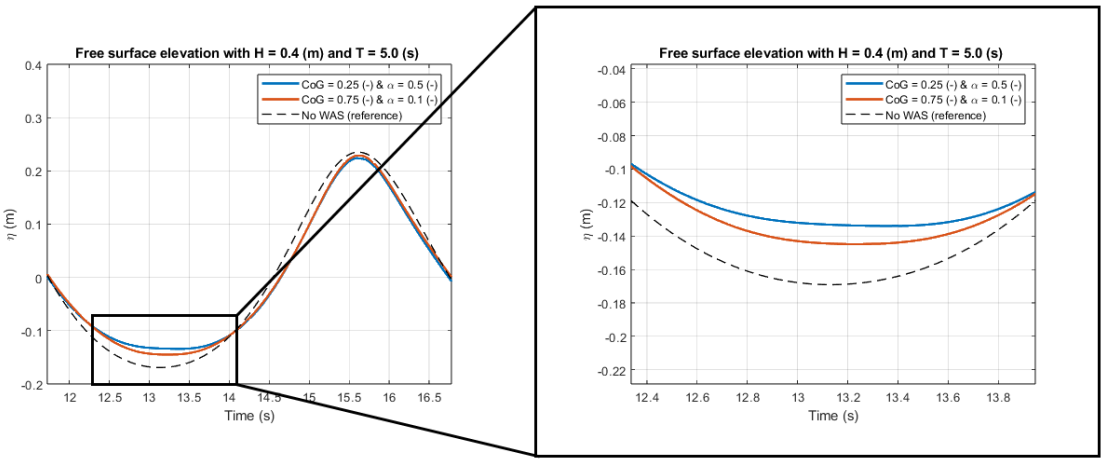


**Figure 9.10:** Free surface elevation behind the best and worst performing WAS in time domain, when examining CoG and $\alpha$ (zooming in on through)

Figures 9.9 and 9.10 show time domain plots, allowing for multiple observations. The analysis of the crests shows a modest wave amplitude reduction of 2%, with the best performing WAS (CoG = 0.25) achieving a reduction of 4%. The troughs exhibit a notable 30% reduction in wave amplitude.

This difference in wave elevation can be linked to the hydrodynamic response of the flap, as illustrated in Figure 9.11. The findings show that larger rotation angles combined with higher angular velocities result in greater free surface reduction. This reduction can be explained by the increased flap dynamics, which produce larger radiated waves that interfere with incoming waves or dissipate energy. This increased wave radiation was also observed during the free decay test presented in Section 9.2.

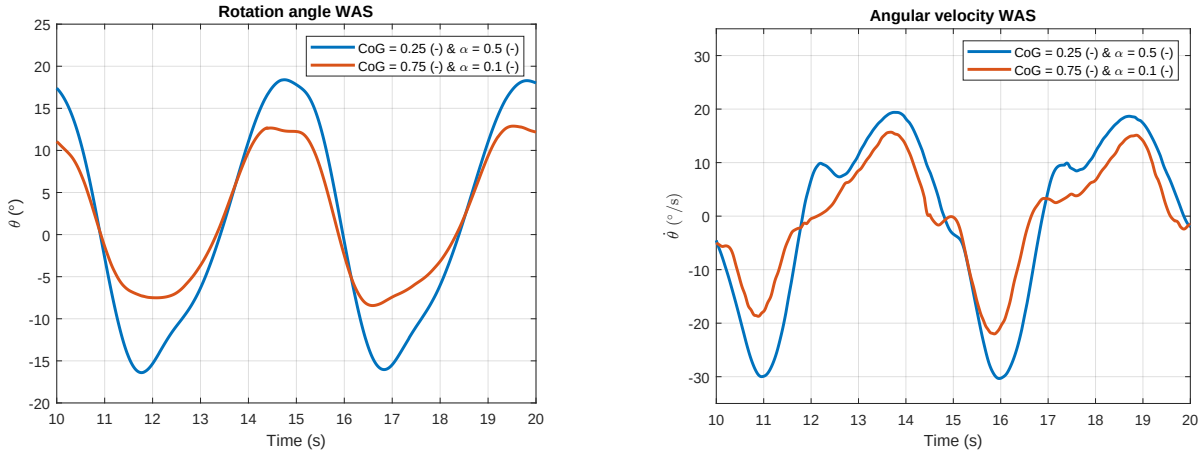


**(a)** Pitching angle in time domain

**(b)** Angular velocity in time domain

**Figure 9.11:** Dynamic properties of the best and worst WAS in time domain, when examining CoG and $\alpha$ with T = 5.0 s

By comparing the best and worst performing WAS, it can be concluded that configurations with a lower CoG result in increased wave amplitude reduction. This effect is evident in both the troughs and crests, where the troughs exhibit a flatter (shallower) shape.

### Design parameter: centre of gravity and wave period

Changing the wave period influences the flap's wave attenuation performance. All configurations presented in Figures 9.8b to 9.13a show an increase in flap dynamics as the wave period approaches 2.5 s. Again, flaps with higher dynamics cause greater power flux differences. However, the configurations with CoG = 0.50 (-) and 0.25 (-) show similar dynamics. Despite the similar dynamics, the power flux difference is greater at CoG = 0.50 (-). The only plausible explanation for this difference is a phase shift, which results in more destructive interference. This will be expanded upon later in this paragraph.

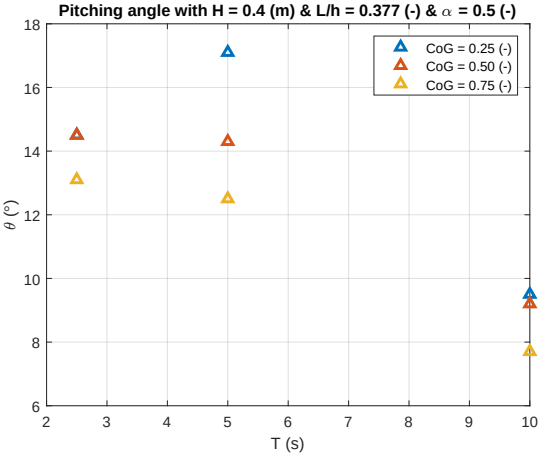


**(a)** Pitching angle of WAS, with varying CoG and wave period

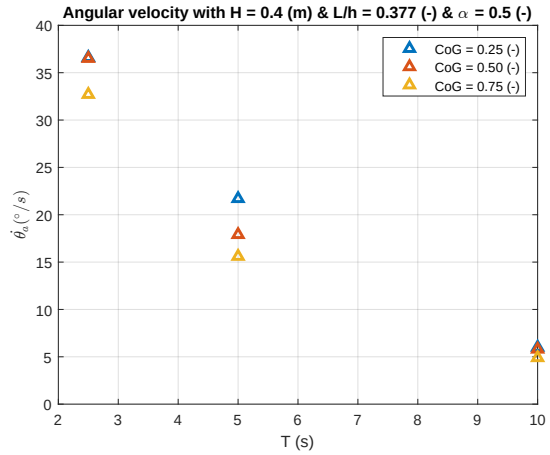


**(b)** Angular velocity of WAS, with varying CoG and wave period

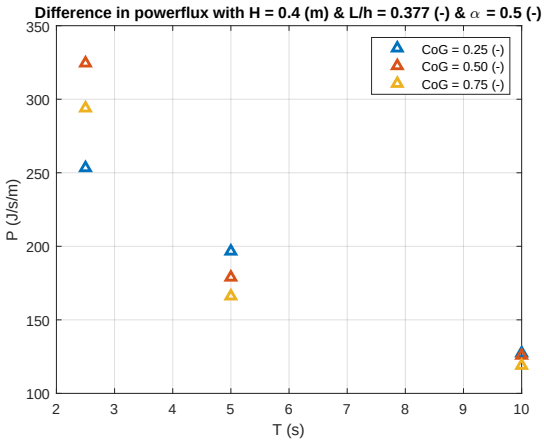


**(c)** power flux difference due to WAS, with varying CoG and wave period

**Figure 9.12:** WAS dynamics in relation with power flux difference for different wave periods

The angular velocity and power flux difference for CoG = 0.50 (-) and 0.75 (-) tends to be exponential across the wave periods, while CoG = 0.25 (-) shows a linear trend. This could indicate that the optimal wave period for this configuration is even lower than 2.5 s. At wave periods of 10.0 s, the dynamics and wave attenuation performance are less pronounced. This is because the wave period is far outside the resonance area of the flap. With these high periods the radiation damping coefficient is also significantly lower (see Figure 9.2). For this reason, this research assumes that all configurations will perform equally in high-period waves.

As previously mentioned, the configurations CoG = 0.25 (-) and CoG 0.50 (-) show the same flap dynamics, but the amount of power flux difference is 23%. The graphs in the time domain are compared to explain the disparity. Figure 9.13 displays the results.

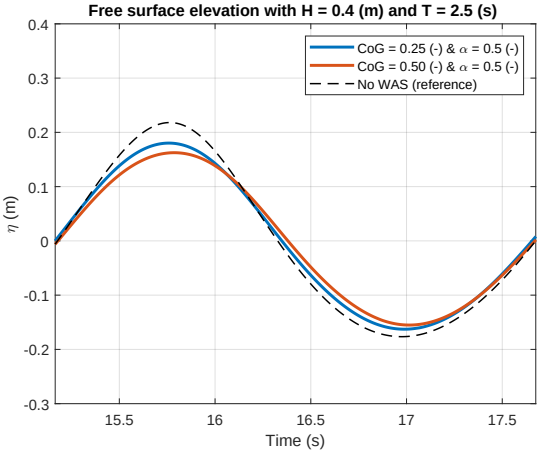


**(a)** Free surface elevation

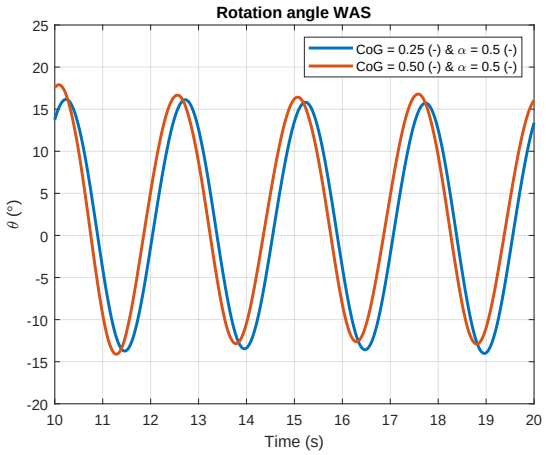


**(b)** Pitching angle

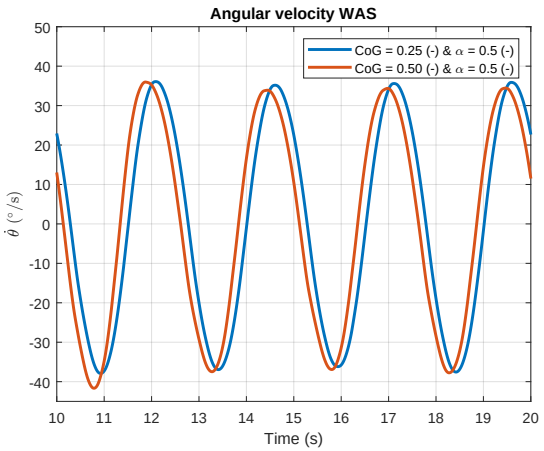


**(c)** Angular velocity

**Figure 9.13:** Comparing free surface elevation and dynamics of worst and best performing WAS with T = 2.5 s

From Figure 9.13a and 9.13b, it follows that the motion and angular velocity amplitudes are nearly identical. The phase of the time signal varies significantly. This phase shift results in a further reduction in maximum amplitude (crest). Henry et al. [19] and Pecher [38] found that this phase shift can increase destructive interference by combining incoming free surface elevation and radiated waves from flap dynamics.

### Design parameter: Mechanical damping

Adding extra mechanical damping $B_m$ to the already existing radiation damping B($\omega$) could increase energy dissipation and thus improve the wave attenuation possibilities of the WAS. As a result, the best performing WAS from the previous paragraph, CoG = 0.25 (-), is selected and tested. The mechanical damping coefficients are sequentially increased to 5.0, 10.0, and 20.0 Nms/°. Figure 9.14 displays the results.

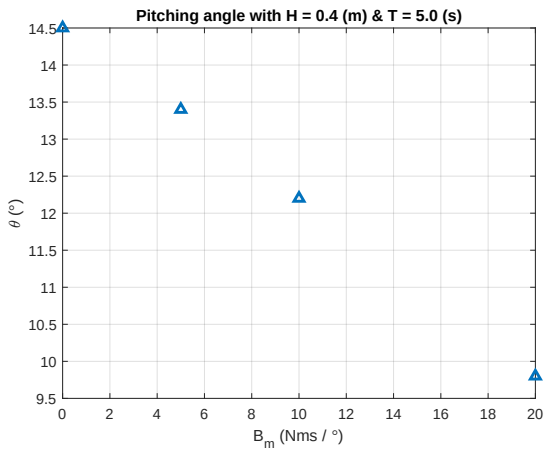


**(a)** Pitching angle of WAS, with varying $B_m$

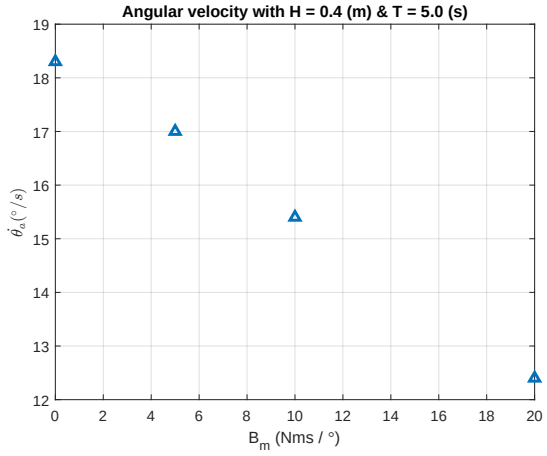


**(b)** Angular velocity of WAS,with varying $B_m$

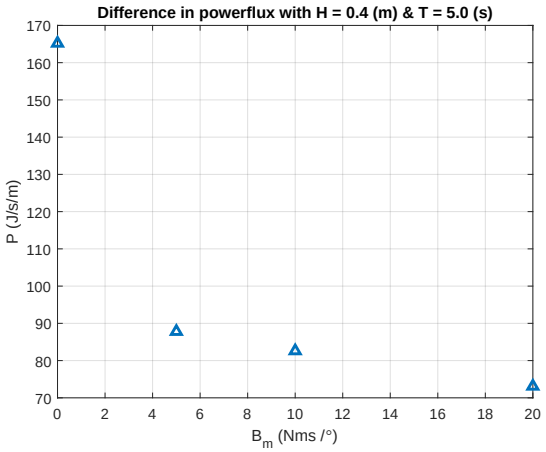


**(c)** power flux difference due to WAS, with varying $B_m$

**Figure 9.14:** WAS dynamics in relation with power flux difference for different $B_m$

Figure 9.14c also shows that a decrease in pitching angle, with possibly more wave reflection, does not increase power flux difference. Apparently, the reduction in angular velocity due to mechanical damping has more effect on the power flux difference. Further research is needed to determine the optimal combination between B($\omega$) and $B_m$.

### Conclusion

To summarise, in Airy and second order Stokes waves, optimal wave attenuation with a 1-DOF WAS occurs when 1) the flap's natural period coincides with the incoming wave period and 2) the period is close to the maximum radiation damping coefficient. This synchronisation increases pitching angles and angular velocities, resulting in larger radiated wave amplitudes and thus more effective destructive interference. Furthermore, changing the CoG can improve the destructive interference effect.

## 9.4. Hydrodynamic Design Optimisation (single WAS in full scale domain)

The local domain results in Model 2 show that wave attenuation is improved by 1) a low centre of gravity, 2) adjusting the flap to the wave period and 3) maximising radiation damping. In the full domain analysis, the approximated wave from Model 1 will excite the best-performing flap.

Figure 6.1 indicates that the area of interest is located within the first 15.0 m of the well-dock. To assess the impact of the WAS, the free surface elevation at x = St.0 + 15.0 m is measured with and without the flap. This is accomplished by bringing the approximated wave input into the numerical domain (via the ComFLOW plug-in function) and placing a numerical wave gauge in the desired location. Furthermore, power flux is calculated using surface elevation data obtained in the frequency domain.

### 9.4.1. Design Parameter: Centre of Gravity

The results from the local domain show that wave attenuation performance improves when the pitching angle and angular velocity are high, this occurs when the flap is in resonance. By adjusting the CoG, the flap can be tuned to the incoming wave period. Raising the CoG lowers the restoring moment, shifting the flap's natural period to longer periods. This shift also means that it is further away from the frequency with the highest radiation damping. For the initial guess, the best performing flap from the local domain will be included in the full scale model. Figures 9.15 shows the results for surface elevation in time and frequency domain and 9.16 the corresponding flap dynamics.

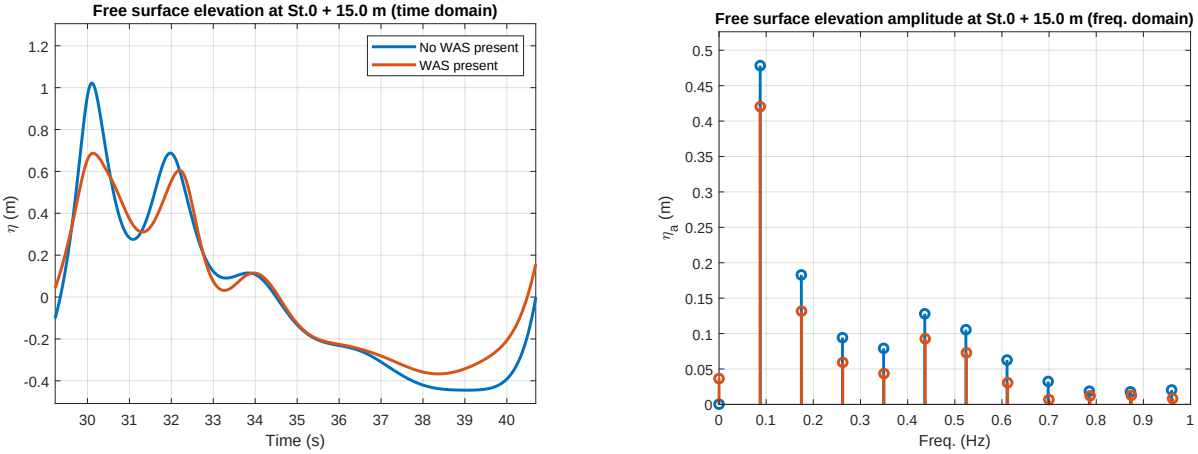


**(a)** Free surface elevation at St. 0 + 15.0 m in time domain

**(b)** Free surface elevation at St. 0 + 15.0 m in frequency domain

**Figure 9.15:** Free surface elevation at St. 0 + 15.0 m, when looking at CoG = 0.25 (-) and $\alpha$ = 0.5 (-)

| power flux in (W/m) | power flux out (W/m) | $\Delta$ power flux (W/m) | $\Delta$ power flux (%) |
|---|---|---|---|
| 7040.0 | 5020.6 | 2019.3 | 28.7 |

**Table 9.6:** Wave attenuation performance of WAS with CoG = 0.5 and $\alpha$ = 0.5 (-)

Several conclusions can be drawn from the free surface elevation data at St.0 + 15.0 m. To begin, at T = 30.0 s the first crest shows the greatest decrease in amplitude. Second, the trough is significantly shallower than when WAS is not present. Lastly, the frequency domain results show that the presence of a WAS reduces the energy of all wave components in the signal.

Table 9.6 shows the power flux difference obtained from this WAS configuration. The results show an attenuation performance of 28.7%. This can be attributed to reflection or the flap's dynamics, which causes a redistribution of energy across different wave frequencies and wave radiation. To summarise, it is clear that the solution effectively reflects and dissipates energy, preventing it from entering the well-dock.

By examining the dynamics of the WAS presented in Figure 9.16, the several observations can made. Firstly, the maximum pitching angle is around 30.0° and the maximum angular velocity is approximately 40.0° / s. Furthermore, it can be seen that the flap oscillates with a frequency of 0.087 Hz, which corresponds to a period of 11.4 s or 0.70 rad/s. This is the same as the dominant period of the incoming approximated wave from Model 1. The strong coupling between waves and bottom-hinged flaps, due to high wave torque is also observed by Henry [19]. Lastly, a smaller resonance peak is observed at 0.35 Hz, likely due to wave components near the flap's natural period.

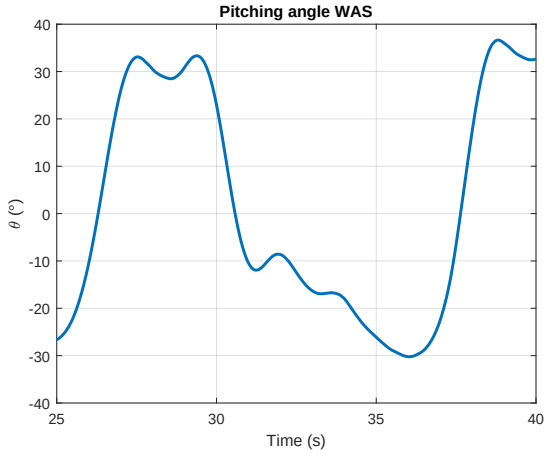


**(a)** Pitching angle of WAS at location St.0

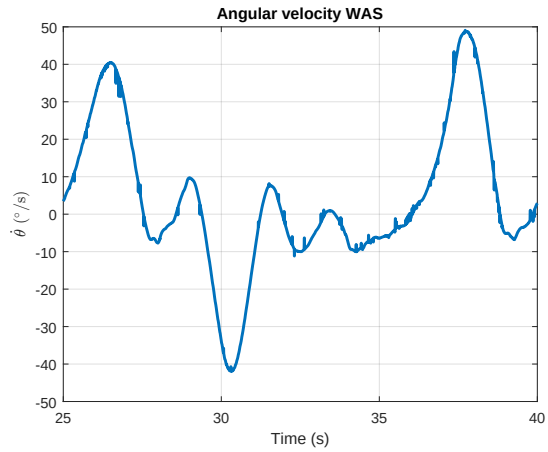


**(b)** Angular velocity of WAS at location St.0

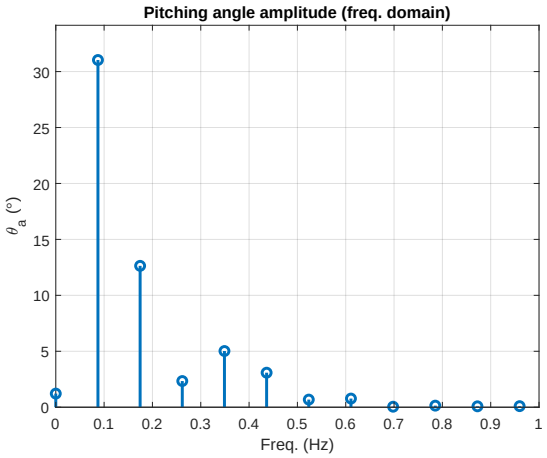


**(c)** Pitching angle amplitude in frequency domain

**Figure 9.16:** WAS dynamics for configuration CoG = 0.25 (-) and $\alpha$ = 0.5 (-)

Figure 9.2 shows that radiation damping is not used optimally in high period wave conditions. With the initial dimensions as depicted in Figure 8.11, the WAS configuration would perform best at 2.9 rad/s or 2.2 s. Despite its low radiation damping coefficient, it can still attenuate almost 30% of wave energy entering the dock. As a result, it is expected that mechanical damping will enhance the WAS design even further.

To compare the three CoG positions within the flap, all CoG-configurations are tested. The results are shown in Figure 9.17 and 9.18. Changing the CoG results in minor differences in the amplitudes of the crests but no significant difference in the troughs. Examining the flap's dynamics reveals that decreasing the CoG causes more rotations and angular velocities. However the effects are minimal. The shape of the first two crests are clearly influenced by CoG = 0.75 (-), which has a lower rotation angle and angular velocity.

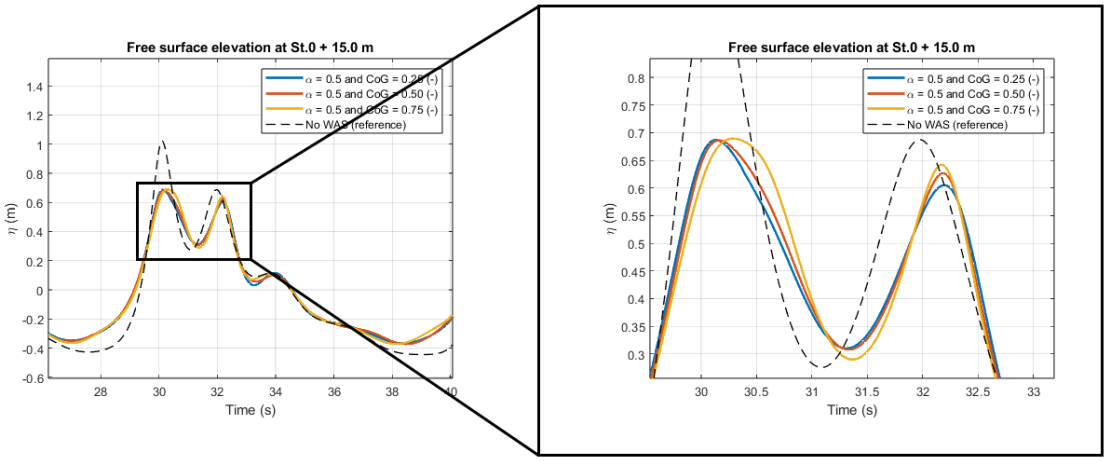


**Figure 9.17:** Free surface elevation at St. 0 + 15.0 m in time domain, when looking at CoG and fixed $\alpha$.

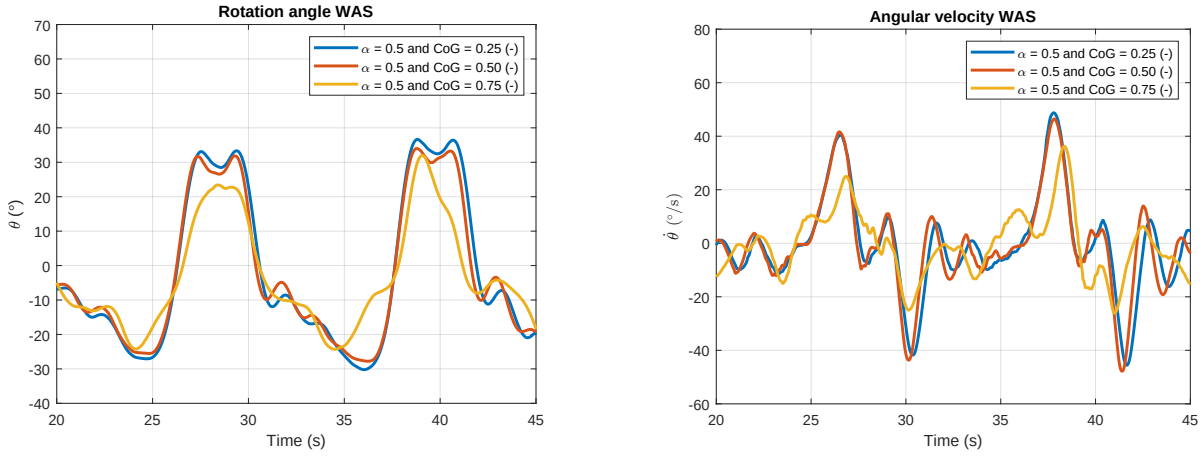


**(a)** Pitching angle of WAS at location St.0

**(b)** Angular velocity of WAS at location St.0

**Figure 9.18:** WAS dynamics for different CoG locations and $\alpha$ = 0.5 (-)

| CoG (-) | power flux in (W/m) | power flux out (W/m) | Δ power flux (W/m) | Δ power flux (%) |
|---|---|---|---|---|
| 0.25 | 7040.0 | 5020.6 | 2019.3 | 28.7 |
| 0.50 | 7040.0 | 5048.4 | 1991.5 | 28.3 |
| 0.75 | 7040.0 | 5052.9 | 1986.9 | 28.2 |

**Table 9.7:** Wave attenuation performance of different CoG positions

Finally, the simulation results (Table 9.7) show a loss of approximately 28% in wave energy for all CoG positions. It should be noted that the various flaps are not yet tuned to either the incoming wave period of 11.4 s or the highest radiation damping coefficient (determined by the WAS's dimensional properties). This implies that the configuration could be improved by adjusting the dimensions to change the radiation damping or incorporating mechanical damping. These adjustments were found to be effective in small-scale results, in which it was discovered that increasing the restoring moment by adjusting the CoG causes an increase in natural frequency, resulting in a greater damping effect.

### Tuning natural period WAS to wave period

This paragraph numerically manipulates the flap's properties by adjusting the radius of gyration $r$ to tune it to the incoming waves. This means that $r$ must be increased to 3.42 m to achieve a natural period of 11.4 s. The results are presented in Figure 9.19.

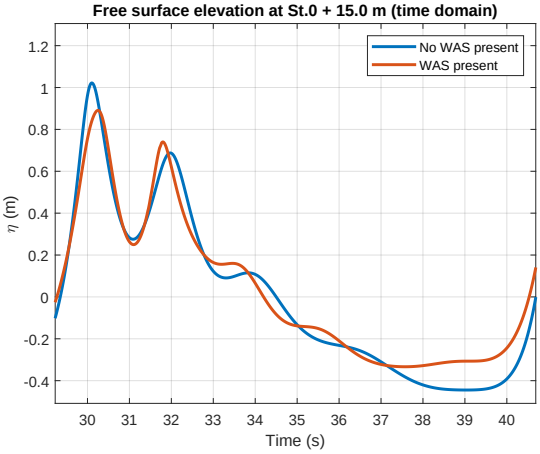


**(a)** Free surface elevation at St. 0 + 15.0 m in time domain

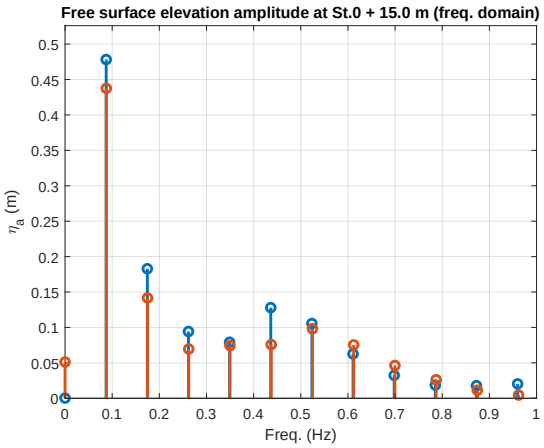


**(b)** Free surface elevation at St. 0 + 15.0 m in frequency domain

**Figure 9.19:** Free surface elevation at St. 0 + 15.0 m, with WAS tuned to wave period

| power flux in (W/m) | power flux out (W/m) | Δ power flux (W/m) | Δ power flux (%) |
|---|---|---|---|
| 7040.0 | 5651.4 | 1388.5 | 19.7 |

**Table 9.8:** Wave attenuation performance of WAS tuned to wave period

Tuning the flap to the incoming wave causes higher pitching angles. In Figure 9.20a, it can be seen that maximum amplitude of 53 degrees is reached. Because of these increased angles and long periods, the second crest passes over the flap without any attenuation. At T = 32.0 s in Figure 9.19a, this effect can be seen. Furthermore, Figure 9.19b demonstrates that higher wave frequency components show minimal decrease in wave amplitude. This concludes that a flap tuned to lower frequencies does not reduce higher frequency wave components. In the end, this configuration reduces power flux by 19.7%.

Figure 9.20a demonstrates that the flap dynamics are smooth and without peaks. This means that other wave components besides the incoming wave have only a minor influence on the motion of the WAS. The findings in Figure 9.20c further support this explanation. The resonance area can be found near the wave period. Finally, it is observed that the angular velocity decreases by 25% compared to 9.18b.

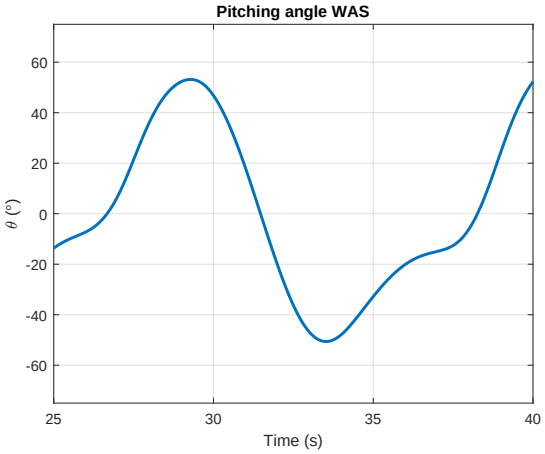


**(a)** Pitching angle of WAS at location St.0

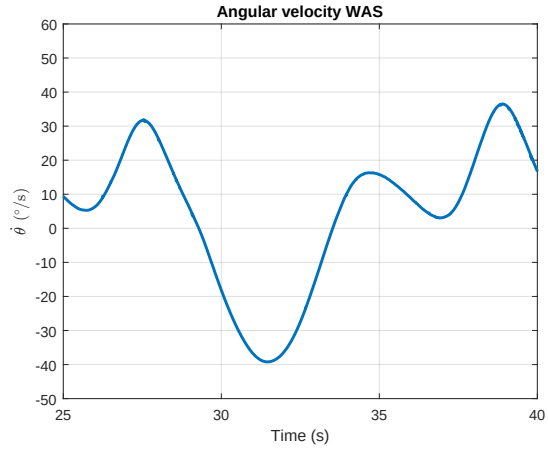


**(b)** Angular velocity of WAS at location St.0

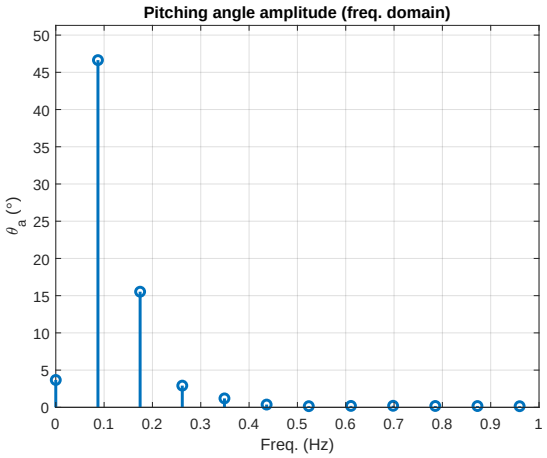


**(c)** Pitching angle amplitude in frequency domain

**Figure 9.20:** WAS dynamics for WAS tuned to wave period

#### Fixed angle of WAS

This subparagraph will look into the relationship between rotation angle and wave attenuation performance. Figure 9.18 shows that the flap's maximum rotation angle is around 30°. In this simulation, the flap is fixed at the specified pitching angle. By ignoring the flap dynamics, the role of these oscillations can be investigated. To gain additional insights, a WAS with a fixed angle of 0° (vertical) is also tested. Table 9.9 summarises the results.

| DOF (-) | power flux in (W/m) | power flux out (W/m) | $\Delta$ power flux (W/m) | $\Delta$ power flux (%) |
|---|---|---|---|---|
| Hinged | 7040.0 | 5020.6 | 2019.3 | 28.7 |
| Fixed (30°) | 7040.0 | 5376.6 | 1663.3 | 23.6 |
| Fixed (0°) | 7040.0 | 4891.1 | 2148.8 | 30.5 |

**Table 9.9:** Wave attenuation performance for different angles and DOF

Table 9.9 shows that the flap's 1-DOF (pitch) motion improves wave attenuation compared to a fixed inclined WAS. This outcome also shows that the hinged flap, which is required to prevent damage caused by collisions, performs nearly identically to a fixed vertically placed flap. This type of fixed flap fully relies on wave reflection.

### 9.4.2. Design Parameter: Length ratio

Table 9.10 shows that increasing flap length improves performance by 9.4%. This improvement is due to two factors. Increasing the flap's length increases its frontal surface area by 37% in 2D, resulting in better reflection of waves. Besides, as shown by the numerical free decay test and BEM-results, increasing the submerged volume leads to a higher damping ratio. As a result, the system radiates more wave energy. These results are consistent with the findings of Yoon et al. [59] and Wang et al. [53], who found that increasing flap height decreases wave transmission and increases reflection.

| L/h (-) | power flux in (W/m) | power flux out (W/m) | $\Delta$ power flux (W/m) | $\Delta$ power flux (%) |
|---|---|---|---|---|
| 0.377 | 7040.0 | 5020.6 | 2019.3 | 28.7 |
| 0.6 | 7040.0 | 4355.7 | 2684.1 | 38.1 |

**Table 9.10:** Wave attenuation performance for different length ratio's

Unfortunately, this optimisation is only intended to demonstrate the effect of flap length on wave attenuation. Due to COMMIT's requirements in the task clarification phase (see Section 6.1.2) and the LCU's draft of 1.4 m, this configuration will eventually hit landing vessels within the flooded well-dock. For this reason, the flap must be made from a flexible material, which could influence the dynamics. This should therefor be further examined.

### 9.4.3. Design Parameter: Mechanical Damping

This subsection adds mechanical damping to the hinge in addition to radiation damping. Figure 9.21 displays the measured free surface elevation in time domain at St.0 + 15.0 m, along with flap dynamics. Based on the graphs in Figure 9.21, several conclusions can be drawn. First, the variations in free surface elevation with different damping coefficients are minor. Zero mechanical damping results in slightly lower crest heights then with mechanical damping. Second, as expected, mechanical damping reduces both rotation angle and angular velocity. This is due to the resistance caused by damping. It is also noted that in case of mechanical damping the time plots of rotation and angular velocity are smoother. Figure 9.21d shows that increasing the mechanical damping reduces the second resonance peak at 0.35 Hz. This would imply that the flap is less responsive to higher frequency wave components. It is important to note that these higher components are responsible for higher radiation damping coefficients. Furthermore, in all three damping cases, the flap motions period corresponds to the dominant period of the incoming wave (full wave coupling). From Table 9.11 it is seen that adding mechanical damping decreases the power flux difference.

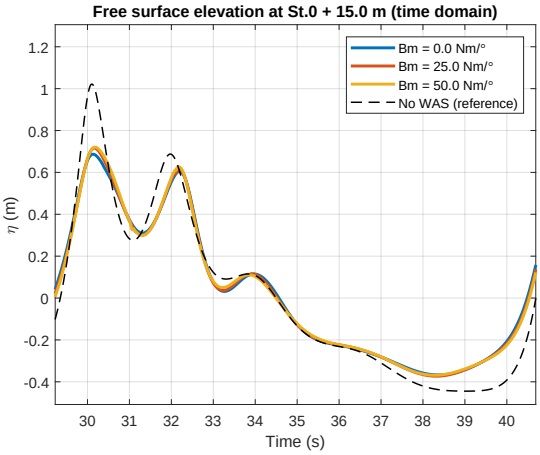


**(a)** Free surface elevation at St. 0 + 15.0 m

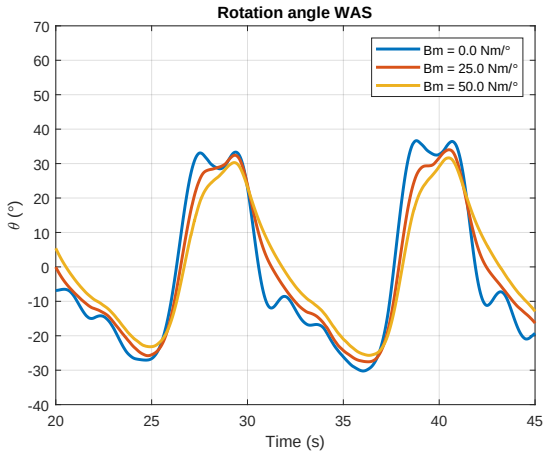


**(b)** Pitching angle of WAS

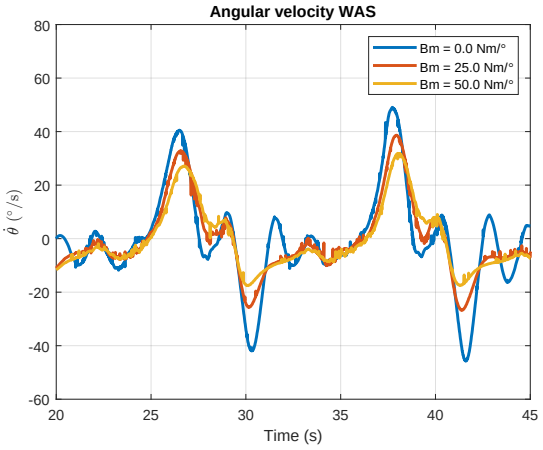


**(c)** Angular velocity of WAS

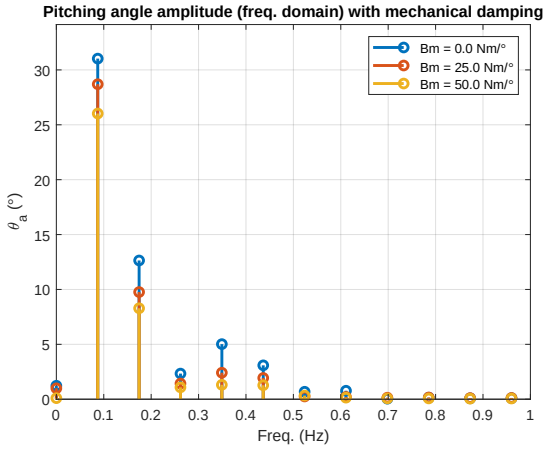


**(d)** Pitching angle amplitude

**Figure 9.21:** WAS dynamics and free surface for configuration CoG = 0.25 (-) and $\alpha$ = 0.5 (-), when looking at different $B_m$

| $B_m$ (Nms/°) | power flux in (W/m) | power flux out (W/m) | Δ power flux (W/m) | Δ power flux (%) |
|---|---|---|---|---|
| 0.0 | 7040.0 | 5020.6 | 2019.3 | 28.7 |
| 25.0 | 7040.0 | 5105.8 | 1934.1 | 27.5 |
| 50.0 | 7040.0 | 5137.3 | 1902.6 | 27.0 |

**Table 9.11:** Wave attenuation performance for different $B_m$

# 10

# Conclusions and Recommendations

In this final chapter the last sub-question presented in Section 1.2 will be answered. Hereby completing the objective of this report. The last sub-question is stated below:

4. ***"How can wave attenuation solutions be optimised by looking at design- and environmental input parameters?"***

## 10.1. Conclusions

In shallow water conditions with non-linear 11.4 s period waves and wave heights of nearly 1.5 m (extreme wave conditions), a submerged bottom-hinged Wave WAS achieves 28.7% reduction in power flux. This attenuation percentage is consistent regardless of changing design parameters such as mass ratio or CoG position. As wave size increases, optimisation such as adjusting mass or CoG becomes less effective due to strong dynamic wave coupling, causing the flap to move in sync with the incoming waves. To optimise wave attenuation slightly, the flap must poses a low CoG which increases angular velocity and therefore damping. In contrast to extreme wave conditions, the WAS dynamics are more sensitive to design changes when subjected to Airy waves and second-order Stokes waves. So, tuning can be used to synchronise the natural period with the incoming wave and the period with maximum radiation damping, resulting in greater wave attenuation. Note, this optimal condition is only present in short period waves with a period of approximately 2.5 s.

In full-scale simulations, adjusting the flap's natural period to match the incoming wave period decreases the power flux difference. By increasing the radius of gyration to tune the WAS, three effects occur. First, the angular velocity is reduced, which directly impacts the damping. Second, the flap exhibits higher pitching angles, resulting in smaller frontal area and therefor less wave reflection as multiple crests passes. Third, the flap has lower sensitivity to higher wave frequencies, leading to less attenuation of these high-frequency wave components. In the end, only 19.7% of wave energy can be attenuated by reflection or dissipation.

Increasing length, improves wave radiation and reflection, resulting in better overall wave attenuation. An increase in length of 37% improves performance by 9.4% and results in a power flux decrease of 38.1%. Note that the actual contributions due to energy dissipation or reflection remain unknown.

The final design parameter, mechanical damping, yields disappointing results as it reduces both the rotation angle and angular velocity, resulting in lower wave attenuation performance in comparison with no mechanical damping. It was discovered that the flap is less sensitive to higher wave components. FFT graphs also show that less energy is attenuated in these higher wave components.

## 10.2. Recommendations

This section provides recommendations how to improve the results obtained within this research. Furthermore, it presents how future research could yield to more accurate solutions.

- Neglecting a sloped bottom and assuming a fixed water depth will reduce shoaling and wave breaking, causing the model to underestimate wave energy dissipation. Even small wave breaking can redistribute significant wave energy. Consequently, the fixed water depth leads to more stable wave propagation, preventing waves from breaking and dissipating their energy. Future research should model time-dependent water depth to accurately capture the breaking, propagation properties, shape, and non-linear effects of waves within the well-dock.
- Wave attenuation is measured by examining the power flux difference, indicating the total attenuation of waves due to reflection and dissipation. In this research, the dynamics of the pitching flap are analysed to determine their influence on power flux difference. These dynamics have two effects: radiating waves as the flap moves and reflecting waves. The optimisation process aims to maximise both effects. However, measuring the total power flux difference does not reveal the underlying relationship between reflection and radiation damping. This makes the optimisation process less effective. Future research should focus on analysing the reflected waves in front of the WAS and the transmitted waves behind the flap. This approach can help identify the optimal combination to maximise wave attenuation.
- Model 2 ignores the beach ramp at the dock's far end. Reflected waves are therefore not taken into account. These waves may have an impact on the flap's dynamics and surface elevation due to wave-wave interaction. Future research should incorporate a beach ramp or an approximate reflected wave input from the right boundary.
- The added mechanical damping yielded unsatisfactory results. Additionally, high levels of mechanical damping coefficients could not be calculated due to convergence problems in ComFLOW. Future research should analyse higher levels of mechanical damping coefficient for possibly maximum wave attenuation performance.
- The current BEM software assumes linear behavior at small amplitudes, which may not be applicable to the full-scale model with large flap motions. To improve accuracy, an unsteady non-linear potential flow solver could be used for additional comparison. Future research could also focus on developing an optimisation method using BEM to reduce computational time and increase the number of results. With these improvements, an iterative optimisation algorithm can be employed to find the ideal combination of design parameters (e.g. mass, lenght, thickness, CoG and CoR).

# References


[1] NATO Standarization Agreement. “STANAG 4195 (edition 1), ”Standarized wave and wind environments and shipboard reporting of sea conditions””. In: (April 1983).

[2] H. Asmuth et al. “Determination of non-linear damping coefficients of bottom-hinged oscillating wave surge converters using numerical free decay tests”. In: Nov. 2014. ISBN: 978-1-138-02871-5. DOI: 10.1201/b18973-71.

[3] D. W. Bass. “Simulating wave action in the well deck of landing platform dock ships using somputational fluid dynamics”. In: 2006. URL: https://api.semanticscholar.org/CorpusID:172131640.

[4] R. Bowman. “Scattering of seismic waves by small inhomogeneities: Ph.D. thesis”. PhD thesis. Department of Geology and Geophysics, MIT, 1955.

[5] H. J. Bungartz and M. Schäfer. *Fluid-Structure Interaction: Modelling, Simulation, Optimisation*. Jan. 2006. ISBN: 978-3-540-34595-4. DOI: 10.1007/3-540-34596-5.

[6] B. Cartwright et al. “Motions of a landing craft in a flooded well dock - effect of well dock design”. In: (Jan. 2007).

[7] B. Cartwright et al. “The modelling of landing craft motions inside a flooded well dock using smoothed particle hydrodynamics”. In: (2006).

[8] W.E. Cummins. *The impulse response function and ship motions*. 1962.

[9] M.A. Davidson et al. “A new non-dimensional number for the analysis of wave reflection from rubble mound breakwaters”. In: *Coastal Engineering* 28.1 (1996), pp. 93–120. ISSN: 0378-3839. DOI: https://doi.org/10.1016/0378-3839(96)00012-9. URL: https://www.sciencedirect.com/science/article/pii/0378383996000129.

[10] Ministerie van Defensie. *LCU-landingsvaartuig (materieel)*. Jan. 2024. URL: https://www.defensie.nl/onderwerpen/materieel/schepen/lcu-landingsvaartuig-materieel.

[11] Ministerie van Defensie. *LCVP-landingsvaartuig (personeel)*. 2024. URL: https://www.defensie.nl/onderwerpen/materieel/schepen/lcvp-landingsvaartuig-personeel.

[12] M.W. Dingemans. “Water wave propagation over uneven bottoms”. PhD thesis. TU Delft, Electrical Engineering, Mathematics and Computer Science, 1994.

[13] M.W. Dingemans and W. Maarten. *Water Wave Propagation Over Uneven Bottoms*. World Scientific Publishing Company, 1997. DOI: 10.1142/1241. eprint: https://worldscientific.com/doi/pdf/10.1142/1241. URL: https://worldscientific.com/doi/abs/10.1142/1241.

[14] J. Falnes. *Ocean waves and oscillating systems*. Cambridge University Press, 2002.

[15] Odd M. Faltinsen. *Hydrodynamics of High-Speed Marine Vehicles*. Cambridge University Press, 2006.

[16] R.P.F. Gomes et al. “A Study on the Wave Energy Conversion by Submerged Bottom-hinged Plates”. In: Sept. 2011. DOI: 10.13140/2.1.3329.9209.

[17] R.P.F. Gomes et al. “The dynamics and power extraction of bottom-hinged plate wave energy converters in regular and irregular waves”. In: *Ocean Engineering* 96 (2015), pp. 86–99. ISSN: 0029-8018. DOI: https://doi.org/10.1016/j.oceaneng.2014.12.024. URL: https://www.sciencedirect.com/science/article/pii/S0029801814004818.

[18] P. Groenenboom and B. Cartwright. “Hydrodynamics and fluid-structure interaction by coupled SPH-FE method”. In: *Journal of Hydraulic Research* 48 (Jan. 2010), pp. 61–73. DOI: 10.1080/00221686.2010.9641246.

[19] A. Henry. “The hydrodynamics of small seabed mounted bottom hinged wave energy converters in shallow water.” PhD thesis. The Queen’s University of Belfast., 2014.

[20] A. Henry et al. “A two dimensional experimental investigation of slamming of an Oscillating Wave Surge Converter”. In: *Proceedings of the International Offshore and Polar Engineering Conference* (Jan. 2014), pp. 296–305.

[21] L.H. Holthuijsen. *Wave in oceanic and coastal waters*. Cambridge University Press, 2007.

[22] H. Hopman, G. Kapsenberg, and E. Krikke. “Design and Hydromechanic Aspects of the Amphibious Transport Vessel for the Royal Netherlands Navy”. In: *Naval Engineers Journal* 106 (Mar. 2009), pp. 163–174. DOI: 10.1111/j.1559-3584.1994.tb02849.x.

[23] J. L. Humar. *Dynamics of structures (3rd ed.)* CRC Press, 2012.

[24] Y. Ikeda. *On the form of non-linear roll damping of ships*. Tech. rep. University of Osaka, 1983.

[25] D. J. Inman. *Engineering vibration (4th ed.)* Prentice-Hall, 2014.

[26] J Journée and W Massie. *Offshore Hydromechanics*. Jan. 2008, p. 570.

[27] D.J Korteweg and G. De Vries. “On the Change of Form of Long Waves Advancing in a Rectangular Canal, and on a New Type of Long Stationary Waves”. In: *Philosophical Magazine* 39 (1895), pp. 422–443. DOI: 10.1080/14786449508620739.

[28] B. Le Méhauté. *An introduction to hydrodynamics and water waves*. Springer, 1976.

[29] Y. Liu. “Nonlinear Hydrodynamic Analysis and Optimization of Bottom-Hinged Oscillating Wave Surge Converters in Shallow Water”. PhD thesis. Department of Civil and Environmental Engineering, Nagoya University, 2022.

[30] Y. Liu et al. “Performance enhancement of a bottom-hinged oscillating wave surge converter via resonant adjustment”. In: *Renewable Energy* 201 (Nov. 2022). DOI: 10.1016/j.renene.2022.10.130.

[31] S. Ma et al. “Consistent formulation of ship motions in time-domain simulations by use of the results of the strip theory”. In: *Ship Technology Research* 63 (Nov. 2016), pp. 146–158. DOI: 10.1080/09377255.2016.1245471.

[32] E. O. Macagno. “Fluid mechanics: experimental study of the effects of the passage of a wave beneath an obstacle”. In: (1953).

[33] P. Naaijen. *Motions and Loadings of Structures in Waves, Part 1 MT44021 2022 - 2023*. TU Delft, 2022.

[34] S. Nallayarasu, C. Hin Fatt, and N. Jothi Shankar. “Estimation of incident and reflected waves in regular wave experiments”. In: *Ocean Engineering* 22.1 (1995), pp. 77–86. ISSN: 0029-8018. DOI: https://doi.org/10.1016/0029-8018(93)E0011-G. URL: https://www.sciencedirect.com/science/article/pii/0029801893E0011G.

[35] Nieuwsredactie NU.nl. *Scheepsbouwer Damen wederom betrokken bij order voor nieuwe marineschepen*. 2024. URL: https://www.nu.nl/economie/6304217/scheepsbouwer-damen-wederom-betrokken-bij-order-voor-nieuwe-marineschepen.html?referrer=https%3A%2F%2Flens.google.com%2F.

[36] G. Pahl et al. *Engineering Design: A Systematic Approach*. Jan. 2007. ISBN: 978-1-84628-318-5. DOI: 10.1007/978-1-84628-319-2.

[37] The Contact Patch. *M.1115 / Seakeeping*. URL: https://the-contact-patch.com/book/marine/m1115-seakeeping.

[38] A. Pecher and J. Kofoed. *Handbook of Ocean Wave Energy*. Jan. 2017. ISBN: 978-3-319-39888-4. DOI: 10.1007/978-3-319-39889-1.

[39] E. Renzi and F. Dias. “Hydrodynamics of the Oscillating Wave Surge Converter in the open ocean”. In: *European Journal of Mechanics - B/Fluids* 42 (Jan. 2013), pp. 2–10. DOI: 10.1016/j.euromechflu.2013.01.007.

[40] E. Renzi et al. “How does Oyster work? The simple interpretation of Oyster mathematics”. In: *European Journal of Mechanics - B/Fluids* 47 (Apr. 2014), pp. 124–131. DOI: 10.1016/j.euromechflu.2014.03.007.

[41] M. Robert. *NavSource Online: Amphibious Photo Archive*. Jan. 2024. URL: https://navsource.org/archives/10/08/0808.htm.

[42] J. Samuel, J. S. Ling, and W. Moebs. *University physics. Volume 1.* OpenStax University Physics, 2016.

[43] T. Sawaragi. “On the Change of Form of Long Waves Advancing in a Rectangular Canal, and on a New Type of Long Stationary Waves”. In: *Coastal Engineering – Waves, Beaches, Wave-Structure Interactions* 78 (1995), pp. 1–479. DOI: 10.1080/14786449508620739.

[44] seaforces.org. *L 800 HNLMS Rotterdam*. 2024. URL: https://www.seaforces.org/marint/Netherlands-Navy/Amphibious-Ship/L-800-HNLMS-Rotterdam.htm.

[45] K. Senol and M. Raessi. “Enhancing power extraction in bottom-hinged flap-type wave energy converters through advanced power take-off techniques”. In: *Ocean Engineering* 182 (2019), pp. 248–258. ISSN: 0029-8018. DOI: https://doi.org/10.1016/j.oceaneng.2019.04.067. URL: https://www.sciencedirect.com/science/article/pii/S0029801819301969.

[46] H. Shi et al. “WHTO: A methodology of calculating the energy extraction of wave energy convertors based on wave height reduction”. In: *Energy* 185 (July 2019). DOI: 10.1016/j.energy.2019.07.068.

[47] J. Spijkers. *Structural Dynamics CT 4140*. Delft: Delft University of Technology, 2005.

[48] Tweede Kamer der Staten-Generaal. “Defensienota 2022 – sterker Nederland, veiliger Europa”. Kamerstuk, 2023, Kamerdossier 36 124, nr. 31.

[49] A. Svendsen. *Introduction to Nearshore Hydrodynamics*. WORLD SCIENTIFIC, 2005. DOI: 10.1142/5740. eprint: https://www.worldscientific.com/doi/pdf/10.1142/5740. URL: https://www.worldscientific.com/doi/abs/10.1142/5740.

[50] P. Van der Plas. *ComFLOW online manual*. URL: https://poseidon.housing.rug.nl/comflow/index.html.

[51] A.E.P. Veldman et al. “Turbulence modeling, absorbing boundary conditions and local grid refinement for free-surface flow simulations in offshore applications”. In: 2014.

[52] G. Wang et al. “Investigation on the Natural Modes of A Semi-Closed Floating Tank”. In: *China Ocean Engineering* 37 (Sept. 2023), pp. 580–587. DOI: 10.1007/s13344-023-0049-8.

[53] K. Wang, Z.Q. Zhang, and W. Xu. “Transmitted and reflected coefficients for horizontal or vertical plate type breakwater”. In: *China Ocean Eng.* 25 (2011), pp. 285–294. DOI: https://doi.org/10.1007/s13344-011-0023-8.

[54] Z. Wang, Y. You, and A. Feng. “Investigation on the Wave Characteristic Inside the Well Dock of LPD Ship in Open Ocean”. In: vol. All Days. International Ocean and Polar Engineering Conference. June 2023, ISOPE-I-23–322.

[55] Y. Wei et al. “Wave interaction with an Oscillating Wave Surge Converter. Part II: Slamming”. In: *Ocean Engineering* 113 (Feb. 2016), pp. 319–334. DOI: 10.1016/j.oceaneng.2015.12.041.

[56] G. Xu et al. “Hydrodynamic Analysis of Ship with Well Deck in the Linear Numerical Wave Tank”. In: *Mathematical Problems in Engineering* 2020 (Mar. 2020), pp. 1–15. DOI: 10.1155/2020/3804748.

[57] T. Yamano, T. Ikebuchi, and I. Funeno. “Stern waves consisting of forward-oriented breaking waves and the remaining following waves”. In: *Journal of Marine Science and Technology* 6 (Jan. 2001), pp. 13–22. DOI: 10.1007/s007730170003.

[58] L. Yingyi. “Introduction of the Open-Source Boundary Element Method Solver HAMS to the Ocean Renewable Energy Community”. In: Sept. 2021.

[59] S. Yoon and K.H. Seo. “Well Dock Design and Assessment of Relative Motions During the Operation of the Landing Crafts Within Well Dock”. In: *Journal of the Society of Naval Architects of Korea* 49 (Apr. 2012). DOI: 10.3744/SNAK.2012.49.2.164.

[60] Z.J. You. “A close approximation of wave dispersion relation for direct calculation of wavelength in any coastal water depth”. In: *Applied Ocean Research - APPL OCEAN RES* 30 (Apr. 2008), pp. 113–119. DOI: 10.1016/j.apor.2008.08.001.

[61] I. Zabala et al. “BEMRosetta: An open-source hydrodynamic coefficients converter and viewer integrated with Nemoh and FOAMM”. In: Sept. 2021.

# A

# Zoomed images from ComFLOW

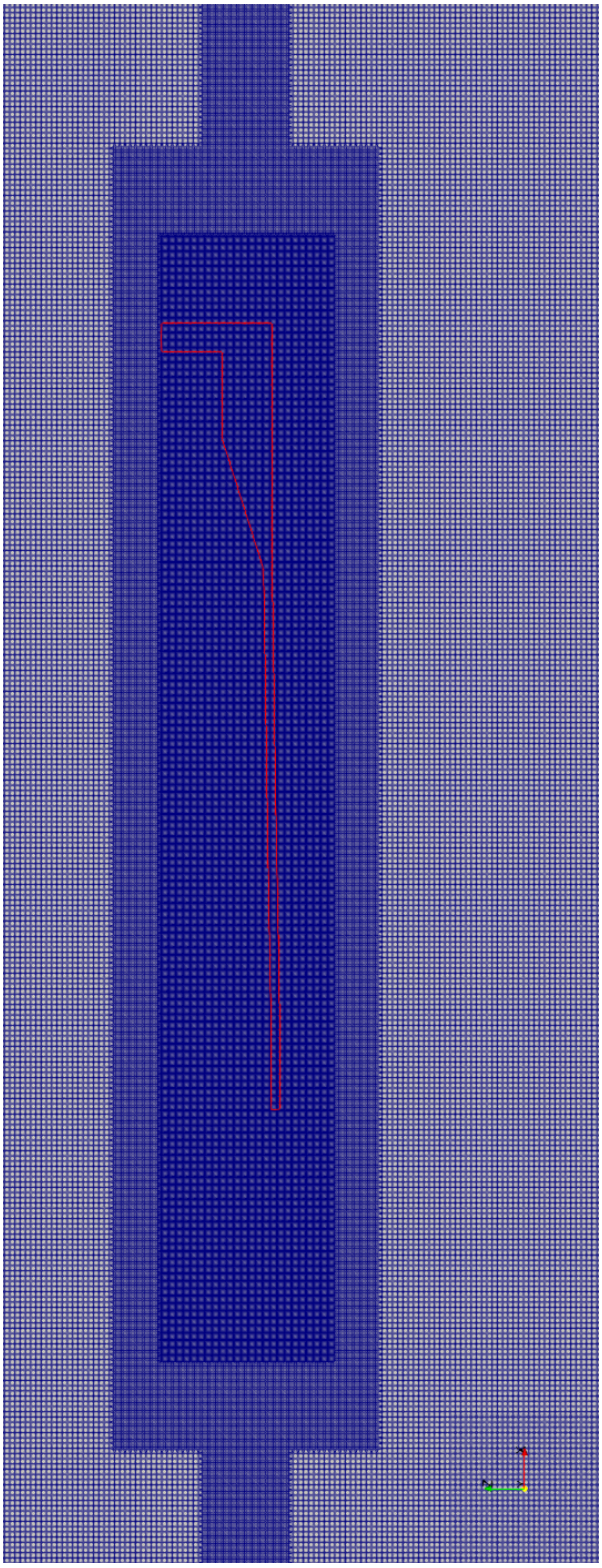

**Figure A.1:** Grid in ComFLOW of Model 1

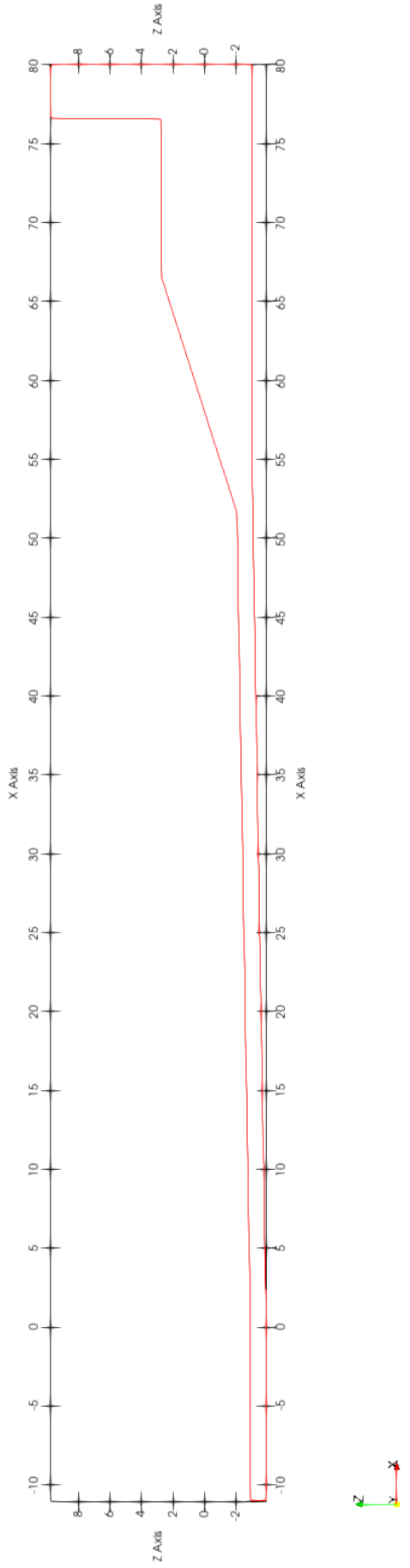


**Figure A.2:** Well-dock dimensions in ComFLOW of Model 1

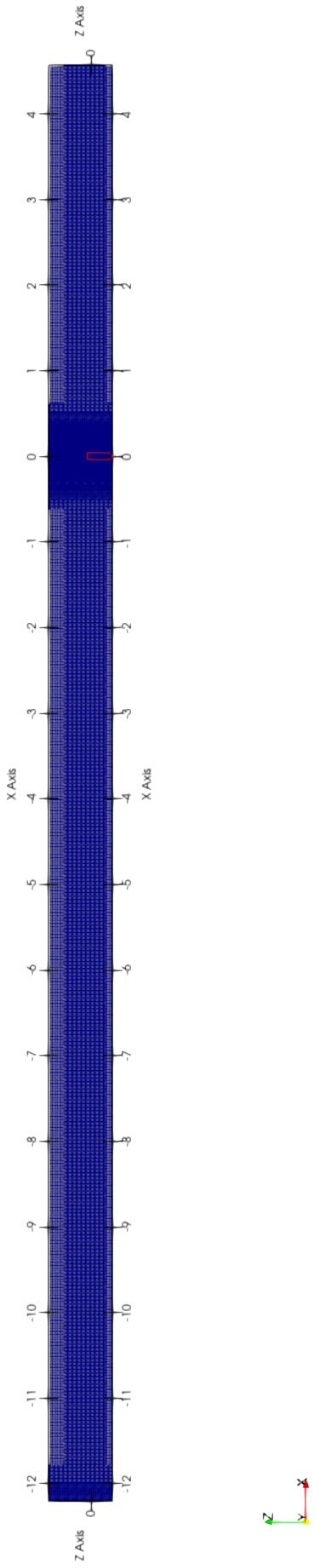


**Figure A.3:** Full domain of domain in validation step of Model 2

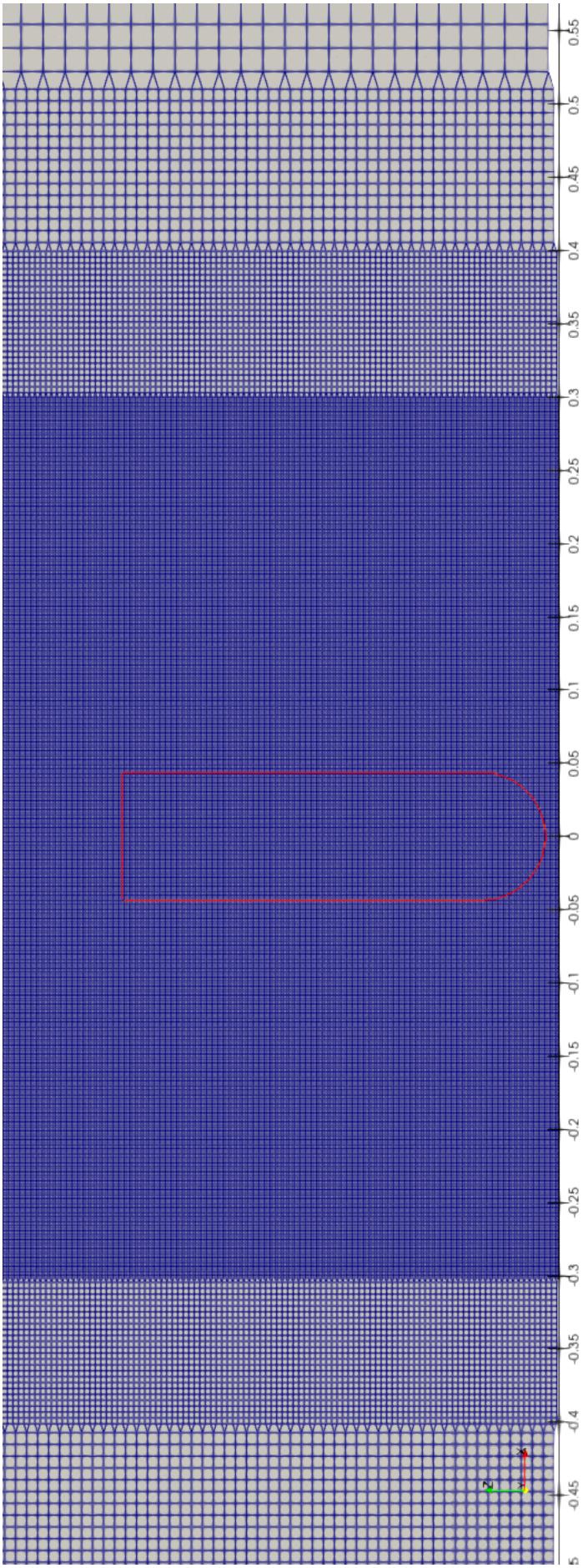


**Figure A.4:** Zoom on flap in validation step of Model 2

# B

# Local domain results Model 2 with Airy waves

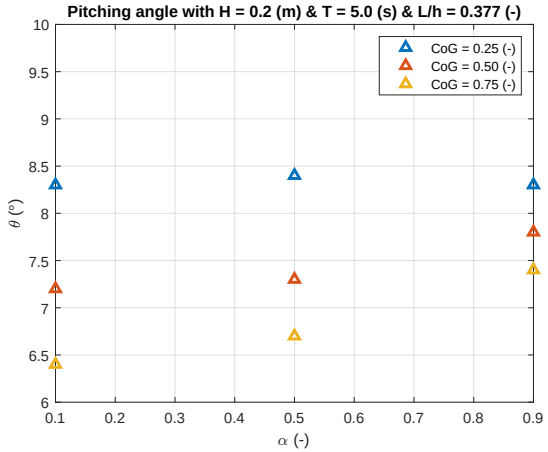


**(a)** Pitching angle of WAS, with varying CoG and $\alpha$

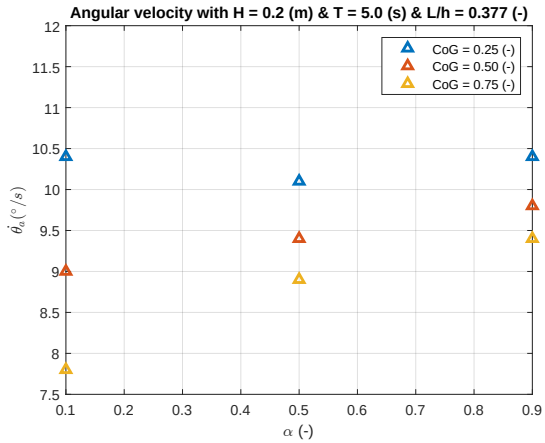


**(b)** Angular velocity of WAS, with varying CoG and $\alpha$

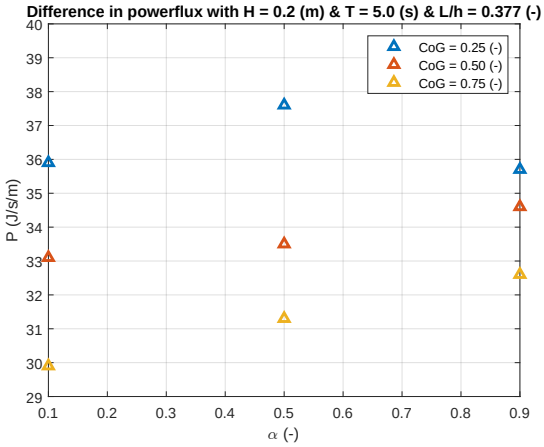


**(c)** Powerflux difference due to WAS, with varying CoG and $\alpha$

**Figure B.1:** WAS dynamics in relation with powerflux difference with Airy waves

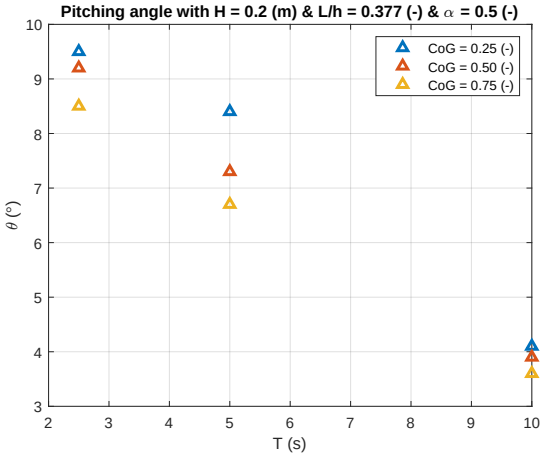


**(a)** Pitching angle of WAS, with varying CoG and wave period

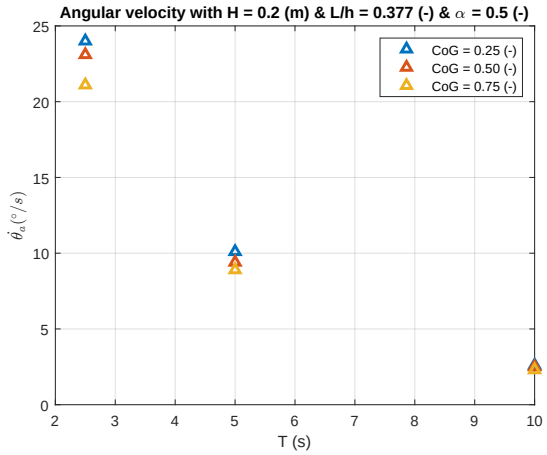


**(b)** Angular velocity of WAS, with varying CoG and wave period

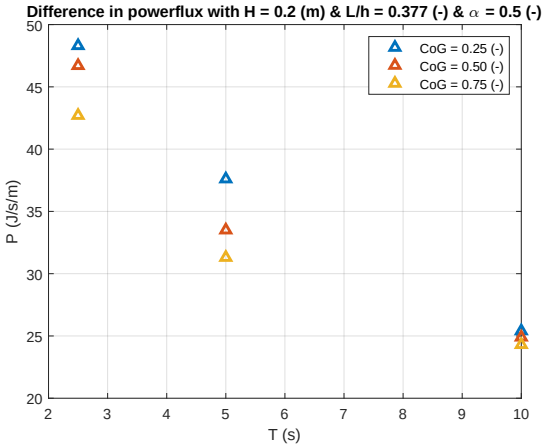


**(c)** Powerflux difference due to WAS, with varying CoG and wave period

**Figure B.2:** WAS dynamics in relation with powerflux difference for different wave periods with Airy waves

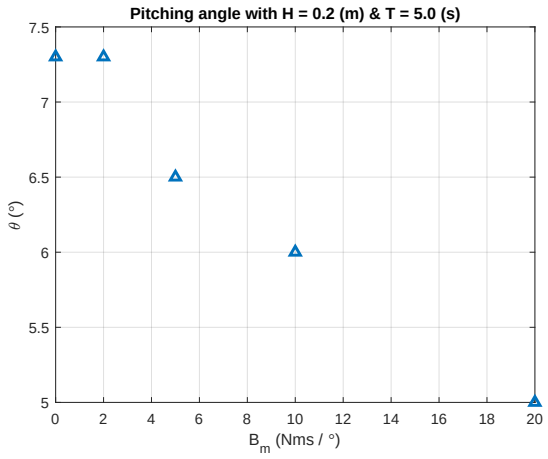


**(a)** Pitching angle of WAS, with varying $B_m$

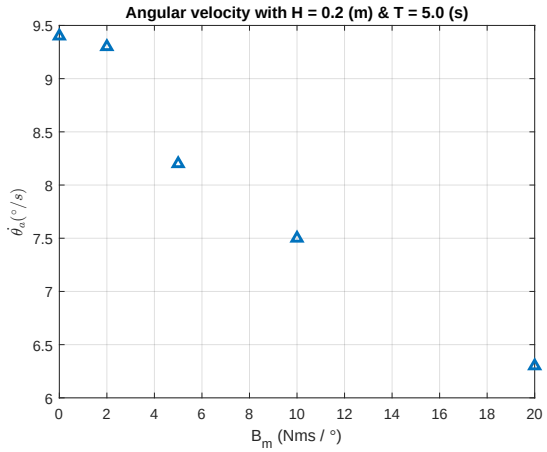


**(b)** Angular velocity of WAS,with varying $B_m$

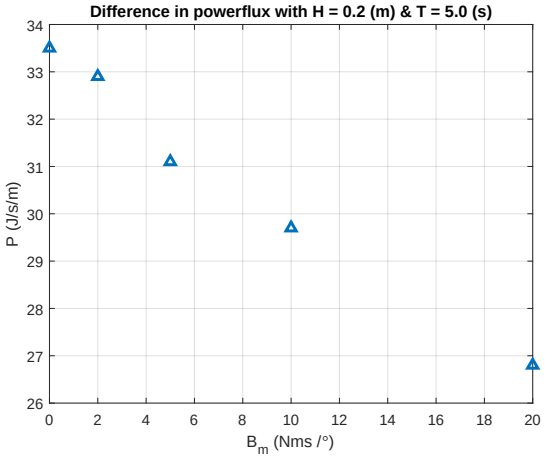


**(c)** Powerflux difference due to WAS, with varying $B_m$

**Figure B.3:** WAS dynamics in relation with powerflux difference for different $B_m$ and Airy waves